Synthesis, Optical and Electronic Properties of Group IV Semiconductor Nanocrystals.

Thesis by

Kirill V. Shcheglov

In Partial Fulfillment of Requirements
for the Degree of
Doctor of Philosophy

California Institute of Technology
Pasadena, California
1997
(Submitted May 2, 1997)

Acknowledgments.

My five years of graduate school at Caltech have been a unique experience. Many people have been instrumental in my successfully finishing my Ph. D. Some of them are listed below.

First and foremost I would like to thank my advisor, Dr. Harry A. Atwater, for all the help, guidance, and support during my graduate studies.

Great thanks to my collaborators in much of this work, Kyu S. Min, Dr. Chih M. Yang, Mark Brongersma, and Dr. Albert Polman. Their energy, help and creativity have been invaluable.

I would like to thank Dr. Gang He for many fascinating and inspiring discussions over the years, as well as for help in understanding much of the physics I have learned.

I wish to thank Kyu S. Min, Maggie Taylor, Claudine Chen, and Joseph Christopherson for much help, inspiration, and fun.

I would like to thank Dr. Imran Hashim and Dr. Jung Shin for help, guidance and good times in my early years of graduate school.

I wish to thank everyone else with whom I have had the pleasure to work in our group, Elizabeth Boer, Renato Camata, Regina Ragan, Geraldine Nogaki, Dr, Ramana Murty, Dr. Selmer Wong, and Dr. Hyun S. Joo. Thank you for all the help and for making the last few years a lot more fun.

I wish to thank Dr. Kerry J. Vahala for letting me use much of the equipment in his laboratory for this work, as well as for his insight into many physical problems.

I wish to thank Carol Garland and Channing Ahn for teaching me to use the TEM, make samples, and for much invaluable help with TEM.

I would like to thank Ali Ghafari and Mike Easterbrook for generous help with maintaining much of the equipment and for teaching me how to use it. I thank Reynold Johnson for letting me use the Aph 9 lab and for teaching me many valuable skills.

I thank Dr. Sergei Orlov for his friendship, for sharing with me his wisdom, physical insight and intuition, and for teaching me to use the equipment in Dr. Yariv's lab.

Great thanks are due to Doruk Engin and Roman Gutierrez for friendship, support and lots of great fun.

I thank Dr. Amnon Yariv for teaching me much fascinating physics and for generously allowing me to use equipment in his laboratory for the nonlinear optical measurements.

I thank Dr. William Johnson who is partly responsible for me being a graduate student at Caltech.

I wish to thank Dr. William Bridges for teaching me optics and for being on my candidacy and defense committees.

I would like to thank my defense committee members, Dr. Harry Atwater, Dr. William Bridges, Dr. Thomas McGill, Dr. Stephen Quake, and Dr. Kerry Vahala for taking the time out of their busy schedules to be at my defense and for letting me graduate.

I wish to thank Rosalie Rowe, Linda Dosza, Illiana Salazar, and Jana Mercado for making my time in graduate school so much easier.

I thank all my friends, Lee Burrows, Teresa Engelhard, Roman and Karina Gutierrez, Greg and Tera Goldmakher, Boris, Masha and Simon, Dan, Boaz, and many others for their friendship, support and for making these years so much better.

I thank UBU for always being there during those lonely nights in the past few months.

I acknowledge the US Congress and NASA headquarters for creating many artificial obstacles to my getting a job at JPL and I thank all the great people at JPL, Roman Gutierrez, Tony Tang, Chris Stell, Wen Li, Lin Miller, and Bill Tang, for helping me overcome them and for all their help in many experiments in this work.

And finally, I thank my family- my mother, my father and my sister. Words could not express how much their continual love and support during these years have meant to me.

Abstract

Group IV semiconductor (Si, Ge and Sn) nanocrystals were synthesized in dielectric matrixes by ion implantation of the respective species into the matrix to form a supersaturated solid solution and subsequent precipitation by thermal annealing. The resulting structure was characterized by Transmission Electron Microscopy and Raman spectroscopy. It was found that nanocrystals of these materials can be effectively synthesized with diameters in the nanometer range. Ge nanocrystals in SiO_2 were extensively characterized, particle size distributions were counted from TEM results and were used to compare experimental photoluminescence spectra with theoretical predictions. Unusual nanostructures were formed in samples co-implanted with Ge and Sn and annealed at 600 °C. Raman spectroscopy indicated a possibility of significant alloying of Ge and Sn in these nanostructures. Optical properties of Si nanocrystals in silicon dioxide were investigated by photoluminescence spectroscopy as well. It was found that while Ge nanocrystal system luminescence is mostly due to defects in the matrix produced by ion implantation, Si nanocrystal sample luminescence is due to the Si nanocrystals themselves. The luminescence is above the bulk Si bandgap and supports the quantum confined excitonic luminescence theory. Light emitting devices were fabricated using both systems. Electroluminescence was observed for both Si and Ge, albeit with rather low efficiency, in the 10^{-6} - 10^{-7} range. Electroluminescence from Si nanocrystal containing devices was spectrally similar to photoluminescence from that system, with a band about 800 nm, consistent with electronic excitation of radiative transitions in Si nanocrystals. Cubic nonlinearities were measured for both Ge and Si nanocrystals and found to be 10^{-9}-10^{-10} esu range. Finally, an interesting interferometric arrangement which has a potential to be useful for investigating nanoscale structures was theoretically described.

List of publications.

Portions of this thesis have been published or will be published under following titles:

H.A. Atwater, K.J. Vahala, R.C. Flagan, R. Camata, R.B. Lee, K.V. Shcheglov, C.S. Tsai, and C.M. Yang, Group III-V and group IV Quantum Dot Synthesis, NATO Advanced Research Workshop on Low-Dimensional Structures, (1995).

C.M. Yang, K.V. Shcheglov, M.L. Brongersma, A. Polman, and H.A. Atwater, Correlation of Size and Photoluminescence for Ge Nanocrystals in SiO_2 Matrixes, Nucl. Instr. Meth. Phys. Res. B **106**, p.433 (1995).

K.V. Shcheglov. C.M. Yang, K.J. Vahala, and H.A. Atwater, Electroluminescence and Photoluminescence of Ge-implanted $Si/SiO_2/Si$ Structures, Appl. Phys Lett. **66**, p. 745 (1995).

K.S. Min, K.V. Shcheglov, C.M. Yang, H.A. Atwater, M.L. Brongersma, and A. Polman, The Role of Quantum-confined Excitons vs. Defects in Visible Luminescence of SiO_2 Films Containing Ge Nanocrystals, Appl. Phys. Lett. **68**, p.2511 (1996).

K.S. Min, K.V. Shcheglov, C.M. Yang, H.A. Atwater, M.L. Brongersma, and A. Polman, Defect-related versus Excitonic Visible-light Emission from Ion-beam Synthesized Si Nanocrystals in SiO_2 , Appl. Phys. Lett. **69**, p. 2033 (1996).

R.C. Gutierrez and K.V. Shcheglov, Interferometry with a Modulated Source, to be published.

Contents.

1. Introduction....1

1.1 Nano-scale Regime....1

1.2 Semiconductor Nanostructures....1

1.3 Synthesis of Semiconductor Nanostructures....2

1.4 Optical and Electronic Properties....3

1.5 Si and Ge Nanocrystals....4

References....6

2 Synthesis of Group IV Semiconductor Nanocrystals....9

2.1 Ion Implantation for Producing Nanocrystals in SiO_2....9

2.2 Synthesis of Ge Nanocrystals....9

2.3 Structural Characterization of Ge Nanocrystal Samples....10

2.4 Ge Nanocrystals Size Distributions....18

2.5 Synthesis of Si Nanocrystals....20

2.6 Structural Characterization of Si Nanocrystal Samples....20

2.7 Synthesis of Sn and SnGe Nanocrystals....23

2.8 Structural Characterization of Sn and SnGe Implanted Samples....23

2.9 Raman spectroscopy of SnGe Nanocrystal Samples....27

References....39

3 Luminescence of Ge and Si Nanocrystals....40

3.1 Introduction....40

3.2 Theoretical Predictions....40

3.3 Description of Photoluminescence Experiment....42

3.4 Photoluminescence of Ge Nanocrystal Samples....42

3.5 Modeling of Ge Photoluminescence Spectra....43

3.6 Deuteration Experiments and Xe^+ Implantation....48

3.7 Experimental Procedure....48

3.8 Deuteration and Xe^+ Implantation Experimental Results....49

3.9 Predictions for Si Nanocrystals....51

3.10 Photoluminescence of Si Nanocrystals....52
3.11 Conclusions....53
References....58
4 Nanocrystal -based Devices....60
4.1 Introduction....60
4.2 Fabrication of Ge Nanocrystal-based LED Structure....60
4.3 Experimental Procedure....61
4.4 Structural Characterization....61
4.5 Electrical and Optical Characterization....63
4.6 Fabrication of Si Nanocrystal-based LED Structure....66
4.7 Experimental Procedure....67
4.8 Structural Characterization....67
4.9 Electrical and Optical Cahracterization....69
4.10 Conclusions....73
References....74
5 Nonlinear Optics of Si and Ge Nanocrystals....75
5.1 Introduction....75
5.2 Sample Preparation....76
5.3 Experimental Procedure....76
5.4 Experimental Setup....78
5.5 Results and Discussion....79
5.6 Conclusions....83
References....84
6 Modulated Source Interferometry and Imaging....85
6.1 Introduction....85
6.2 Interferometry with a Modulated Source....85
6.3 Two-beam Interferometry of an Arbitrary Spectrum Source....86
6.4 Sinusoidally Modulated Semiconductor Laser....90
6.5 Interferometric Imaging with a Modulated Source....92
References....96

List of Figures.

Figure 2.1 Ge concentration depth profiles after ion implantation and after subsequent annealing....11
Figure 2.2 Bright field TEM images of 2×10^{16} /cm^2 Ge-implanted sample annealed at different temperatures....12
Figure 2.3 2×10^{16} /cm^2 Ge-implanted sample annealed at 1000 °C for different lengths of time....14
Figure 2.4 Bright field TEM of 2×10^{16} /cm^2 and 5×10^{16} /cm^2 Ge-implanted samples annealed at 1000 °C....15
Figure 2.5 High resolution TEM images of the 2×10^{16} /cm^2 Ge-implanted samples annealed at 600 °C and 1200 °C....15
Figure 2.6 Cross-sectional TEM images of the 2×10^{16} /cm^2 Ge-implanted sample annealed at 800 °C....16
Figure 2.7 Raman scattering spectra of Si- and Ge- implanted samples....17
Figure 2.8 Tabulated Ge nanocrystal size distributions and gaussian fits to them....19
Figure 2.9 High resolution images of Ge and Si nanocrystals....21
Figure 2.10 High resolution images of Ge and Si nanocrystals at higher magnification..21
Figure 2.11 TEM images of Sn-implanted sample annealed at 800 °C....25
Figure 2.12 High resolution TEM image of a Sn nanocrystal....26
Figure 2.13 TEM images of 4×10^{16} /cm^2 Ge and 1×10^{16} /cm^2 Sn co-implanted sample annealed at 600 °C....29
Figure 2.14 High resolution TEM image of of 4×10^{16} /cm^2 Ge and 1×10^{16} /cm^2 Sn co-implanted sample annealed at 600 °C....30
Figure 2.15 TEM images of 4×10^{16} /cm^2 Ge and 1×10^{16} /cm^2 Sn co-implanted sample annealed at 800 °C....31
Figure 2.16 High resolution TEM image of 4×10^{16} /cm^2 Ge and 1×10^{16} /cm^2 Sn co-implanted sample annealed at 800 °C....32
Figure 2.17 High resolution TEM image of 2×10^{16} /cm^2 Ge and 2×10^{16} /cm^2 Sn co-implanted sample annealed at 600 °C....33

Figure 2.18 Raman shift of Ge-Ge stretch in Sn_xGe_{1-x} MBE grown films for different Sn concentrations....34

Figure 2.19 Raman scattering spectra of 4×10^{16} /cm^2 Ge and 1×10^{16} /cm^2 Sn co-implanted samples and 2×10^{16} /cm^2 Ge and 2×10^{16} /cm^2 Sn co-implanted samples annealed at different temperatures....35-37

Figure 3.1 Summary of theoretical predictions for Ge nanocrystals....41

Figure 3.2 Photolumiescence spectra of Ge nanocrystals....43

Figure 3.3 Comparison of measured and calculated photoluminescence spectra....47

Figure 3.4 Effect of deuterium on Ge nanocrystal photoluminescence intensity....50

Figure 3.5 Comparison of photoluminescence from Ge and Xe implanted samples....51

Figure 3.6 Summary of theoretical predictions for Si nanocrystals....52

Figure 3.7 Effect of deuterium on Si nanocrystal photoluminescence....55

Figure 3.8 PL stectra of etched-back samples....56

Figure 3.9 Calculated size distributions for Si nanocrystals....57

Figure 4.1 Cross-sectional TEM images of Ge nanocrystal LED structure....62

Figure 4.2 I-V characteristic of a typical Ge nanocrystal device....64

Figure 4.3 Photoluminescence and electroluminescence spectra of the Ge nanocrystal LED structure....65

Figure 4.4 Cross-sectional TEM images of Si nanocrystals in the Si nanocrystal LED structure....68

Figure 4.5 I-V characteristic of a typical Si nanocrystal device....71

Figure 4.6 Electroluminescence spectra of the Si nanocrystal LED taken at different voltages....71

Figure 4.7 Photoluminescence spectrum of the Si nanocrystal device....72

Figure 4.8 Electroluminescence in the forward breakdown regime....73

Figure 5.1 Schematic of the z-scan Experimental setup....77

Figure 5.2 Measuring Δn using z-scan....78

Figure 5.3 Z-scan measurements on Ge nanocrystals in silica and sapphire....80

Figure 5.4 Z-scan measurements of Si nanocrystals in silica and sapphire....81

Figure 5.5 Optical damage from excessive incident power....82

Figure 6.1 Schematic of modulated source interferometric imaging setup....93

List of Tables.

Table 2.1 Summary of Ge and SiGe diffraction data....24
Table 5.1 Summary of implantation characteristics....76
Table 5.2 Summary of experimental results....83

Chapter 1

Introduction

1.1 Nano-scale regime.

The properties of materials on an atomic scale are governed primarily by quantum effects. On a macroscopic scale these effects sometimes exhibit themselves in a few interesting systems (such as superfluidity or superconductivity), but for the most part they average out to an approximately classical behavior, i.e., quantum effects need not be considered in the physical theory. There is however a size regime where the behavior begins to deviate from classical, and while it is not purely a quantum regime, quantum effects cannot be discounted in the description. This regime for most materials is in a few nanometer range.

Many properties of nanostructures can be treated approximately in a classical manner, but they are strongly influenced by size, since quantum mechanics begins to come into play. Hence it is possible to tune the behavior of these structures simply by changing their dimensions in the nm range.

1.2 Semiconductor nanostructures.

Nanostructures of semiconductor materials offer one of the most exciting prospects for new physical systems and devices. A number of systems have been under investigation for over 20 years. Some, such as one-dimensional quantum wells of III-V alloy semiconductors already find a host of practical applications, such as Quantum Well (QW) solid-state lasers and optical amplifiers, which are a commercial product, and quantum well detectors for mid-range infrared frequencies [1,2]. One-dimensional QW's already show some of the interesting features of quantum confinement. For instance, the binding energy of the exciton in two dimensions is four times larger than in three dimensions. Exciton-related effects, such as pronounced optical nonlinearities observable in III-V quantum wells even at room temperature, are actively investigated for optical

communications applications, such as frequency conversion [3]. It is widely believed that going to lower dimensional systems will offer even more possibilities for novel effects and devices, such as optical nonlinearities enhanced by orders of magnitude, coulomb blockade effects for single electron devices, and quantum dot tunneling transistors and diodes, to name a few [4].

1.3 Synthesis of semiconductor nanostructures.

While it is relatively easy to produce one-dimensional QW's by a number of thin film growth techniques [5], two- and three- dimensional nanostructures are much more difficult to realize since one must define the structure not only in the vertical dimension, but also in one or two lateral dimensions. Current limits of conventional photolithography are in the hundreds of nanometers, so two orders of magnitude improvement is needed to make this technique useful for making nanostructures. Electron beam lithography has been used to define structures tens of nanometers in size [6], but since for most semiconductor materials the range of interest lies below 10-20 nanometers, and since precise control of structure dimensions must be maintained, usefulness of this technique is also limited. In addition there are secondary problems with available etching and patterning methods, most of them with a few notable exceptions [7] such as selective CVD, do not work well in the nanometer range.

For these reasons, investigators of semiconductor two-dimensional nanostructures (quantum wires) and three-dimensional nanostructures (quantum dots) have relied on indirect methods for producing them. Quantum wires of III-V materials have been synthesized by selective growth on step-edges, miscut substrates and patterned (V-grooved) substrates [8], and of group IV materials - by controlled oxidation and subsequent thinning of e-beam defined ridges and selective nucleation on patterned substrates [9]. Chemical synthesis of Ge quantum wires has been reported as well [10]. Quantum dots have generally been made by precipitation of the dot material out of a solution, by selective nucleation and growth at specific sites, and by islanding during growth on mismatched substrates. Group III-V and group IV quantum dots have been grown by selective nucleation on miscut and lattice mismatched substrates, and on

patterned substrates [11]. Aerosol techniques (evaporation and condensation in gas phase) have been applied to synthesize III-V, Si and Ge nanocrystals [12]. Synthesis of II-VI nanocrystals is commonly done by subsequent precipitation of respective components dissolved in the glass melt[13] chemically in solution [14]. Noteworthy is an astonishing degree of size control possible for the second technique (typically to a monolayer), as well as efficient surface passivation by organic ligands. Group IV nanocrystals have been synthesized in solution by chemical means as well and size-selected for characterization by liquid chromatography [15].

Chemical vapor deposition has also been used to synthesize arrays of Si quantum dots [16]. Another commonly used method for synthesis of group IV nanocrystals has been precipitation out of a supersaturated solid solution prepared by a number of techniques [17]. The method of choice in this work has been ion implantation of respective species into the host matrix because precise control of resulting concentration profile is possible with this technique.

1.4 Optical and electronic properties.

Electronic and optical properties of nanocrystals are strongly influenced by their size. The effects depend on the specific material, but some qualitative features are common to all systems. Generally, when the infinite periodic potential of a crystal is reduced in size to dimensions at which a majority of valence electrons begin to "feel" the surface, the electronic bandstructure undergoes significant changes. Bulk Bloch electron wavefunctions are no longer eigenstates of the system and thus crystal momentum is no longer a "good" quantum number. Quantum states which were before delta functions of momentum begin to "smear out" the characteristic smearing being $\frac{k_b a}{d}$ where "k_d" is the width of the Brilluoin zone, "d" the diameter of the nanocrystal, and "a" the lattice constant. Thus electronic transitions which are forbidden in the bulk because they do no conserve crystal momentum are allowed due to overlap of the tails of smeared out wavefunctions. The finite envelope potential also mixes electron wavefunctions which are relatively decoupled in the bulk , and this generally leads to changes in the electronic

bandstructure. Significant changes are also observed for excitons (coupled electron-hole pairs) when the nanocrystal radius is around the exciton radius. The binding energy of the exciton increases significantly leading to stable excitons at room temperature for small enough particle diameters[18].

Beyond these general remarks, the behavior strongly depends on the nature of the semiconductor.

Direct bandgap semiconductors with parabolic band edges such as GaAs and II-VI materials are relatively well understood and effects of reducing nanocrystal size are somewhat successfully treated analytically in the effective mass approximation (k•p theory), although some systematic errors persist in calculations due to inadequate description of bulk band dispersion [19]. Indirect bandgap semiconductors, particularly Si and Ge, offer significant challenges due to the indirect nature of the bandgap, band nonparabolicity, and phonon mixing of electron states that cannot be discounted in the complete description. Various predictions exist for group IV semiconductor nanocrystals, including the effective mass model, cluster calculation, tight-binding approximation, and explicit treatment of phonon coupling [18,20]. Although there is quite a bit of discrepancy in the numbers, a general trend indicates that for Si and Ge the bandgap should increase with decreasing size, and for sizes on the order of a few nanometers, should become quasi-direct.

Interesting excitonic effects, such as enhancement of cubic nonlinearities and stark-effect are predicted as well [21].

1.5 Si and Ge nanocrystals.

Group IV materials they are logical candidates for future nanoscale electronic and optical applications, since Si processing technology is quite mature. However, interest in Si and Ge nanocrystals was renewed largely as a result of observation of efficient photoluminescence from porous silicon in 1990 [22].

Since then a number of Si and Ge nanocrystal systems has been examined, though experimental investigation has been somewhat hampered by difficulty of producing

sufficient quantities of size-selected nanocrystals. Nevertheless, photoluminescence in the visible has been observed in a number of systems, such as various kinds of porous Si, Ge and Si nanocrystals in dielectrics, and Ge islands grown on GaAs and Si substrates. Electroluminescent devices have been fabricated based on porous Si, Si nanocrystals, and SiGe quantum dots grown on Si substrates [23], with quantum efficiencies in the 0.01 to 0.1 % range. Some coulomb blockade effects also have been investigated, although in this application the internal physics of quantum dots is mostly ignored.

In the following chapters synthesis, structural characterization, and optical properties of group IV nanocrystals in SiO_2 will be described. These materials, while still a distance away from being technologically useful, offer exciting possibilities of integrated optoelectronic circuits, as well some intriguing opportunities for investigation of fundamental physics of nanoscale structures.

References.

[1] See, for instance A. Yariv, "Quantum Electronics" p.264 J. Wiley & Sons, New York (1989);
P.J.A. Thijs et al., Phil. J. Res. **49**, p.187 (1995).

[2] H. Schneider et al., Appl. Phys. Lett. **70**, p.1602 (1997);
K.L. Doughty et al., Semicond. Sci. Tech. **5** p.494 (1990);
T. Osotchan et al., Mat. Sci. Electr. B **35**, p. 176 (1995).

[3] H. Ando et al., J. Appl. Phys. **70**, p.7024 (1991), G. Bongiovanni et al. Semicond. Sci. Tech. **12**, p.300 (1997); G.P. Bava et al. IEEE Proc. Opto. **143**, p.119 (1996);

[4] R.J. Haug et al., Surf. Sci. **263**, p.415 (1992);
Y.X. Liu et al., Phys. Rev. B **54**, p.5675 (1996);
T. Takagahara, Surf. Sci. **267**, p.310 (1992);
M Dilger et al., Semicond. Sci. Tech. **11**, p.1493 (1996);
M Stopa, Phys. Rev. B **54**, p. 13767 (1996);
J.H. Luscombe et al., Proc. IEEE **79**, p.1117 (1991);
C.W.J. Beenakker, Phys. Rev. B **44**, p.1646 (1991).

[5] such as MBE, sputtering, CVD and MOCVD, LPE, MOVPE etc.

[6] C. Vieu et al., Microelectr. Eng. **35**, p.253 (1997);
E. Difabrizio et al., Jpn. J. Appl. Phys. **36** p.L70 (1997).

[7] B. Dwir et al., Microelectr. Eng. **35**, p.269 (1997);
T.K. Whidden et al., J. Electrchem. Soc. **144**, p.605 (1997).

[8] L Pfeiffer et al., J. Cryst. Growth **111**, p. 333 (1991);
X.L. Wang et al., J Cryst. Growth **171**, p. 341 (1997);
M. Lopez et al., Sol. St. Electr. **37**, p.563 (1994).

[9] N. Usami et al., Sol. St. Elctr. **37**, p. 539 (1994);
Y. Nakajima et al., Appl. Phys. Lett. **65**, p. 2833 (1994).

[10] J.R. Heath and F.K. Legoues, Chem. Phys. Lett. **208**, p.263 (1993).

[11] W. Seifert et al., Prgress in Crystal Growth and Characterization of Materials, **33**, p. 423 (1996);

R. Notsel, Semicond. Sci. Tech. **11**, p.1365 (1996);

J. Tersoff et al., Phys. Rev. Lett. **76**, p.1675 (1996);

M. Dilger et al., Superlatt. Microstruct. **21**, p.533 (1997).

[12] I. Maximov et al., J.Vac.Sci.Tech. **11**, p.748 (1993).

M. Danek et al., Appl. Phys. Lett. **65**, p. 2795 (1994).

[13] A. I. Ekimov et al., Sov. Phys. Semicond. **16**, p. 775 (1982);

A. I. Ekimov et al., JETP Lett. **34**, p. 345 (1981);

A. I. Ekimov et al., Sol. State Comm. **56**, p. 921 (1985);

U. Woggon et al., Superlatt. Microstruct. **9**, p.245 (1991).

[14] M. Danek et al., Chem. Mat. **8**, p.173 (1996).

[15] L.E. Brus, J. Chem. Phys. **80**, p.4403 (1984);

J.R. Heath et al., J. Phys. Chem. **100**, p.3144 (1966);

J.R. Heath et al., J. Chem. Phys., **101**, p.1607 (1994).

[16] A. Nakajima, Y. Sugita, K. Kawamura, H. Tomita, and N. Yokoyama, Jpn. J. Appl. Phys. **35**, p. L189 (1996).

[17] S. Hayashi, E. Nishimae, and K. Yamamoto, Proc. ISSPIC-6, Chicago M-061 (1992).

K.S. Min, K.V. Shcheglov, C.M. Yang, H.A. Atwater, M.L. Brongersma, and A. Polman, Appl. Phys. Lett. **69**, p.2033 (1996).

[18] T. Takagahara and K. Takeda, Phys. Rev. B **46**, p. 15578 (1992).

[19] D.W. Wood and A. Zunger, Phys. Rev. B **53**, p. 7949 (1996).

[20] N. A. Hill, Private Communication (1994);

M.S. Hybertsen, Phys. Rev. Lett. 72, p.1514 (1994);

B. Delley and E. F. Steigmeier, Phys Rev. B. **47**, p. 1397 (1993);

N. A. Hill and K.B. Whaley, Phys. Rev. Lett. **75**, p.1130 (1995).

[21] S. Jaziri et al., Journal de Physique IV **3**, p. 367 (1993);

P.J. Thomson et al., Appl. Phys. Lett. **68**, p.946 (1996).

[22] L.T. Canham, Appl. Phys. Lett., **57**, p. 1046 (1990).

[23] Y. S. Tang et al., Electr. Lett. **31**, p.1385 (1995).

L Tsybeskov, S.P. Duttagupta, and P.M. Fauchet, Sol. St. Comm. **95**, p.429 (1995).
L. Tsybeskov, S.P. Duttagupta, K.D. Hirschman, and P.M. Fauchet, Appl. Phys. Lett. **68**, p. 2058 (1996).

Chapter 2

Group IV Semiconductor nanocrystals in SiO_2

2.1 Ion Implantation for producing nanocrystals in SiO_2.

Nanocrystals samples used in this work were made by ion-implanting the respective group IV element into SiO_2 to form a supersaturated solid solution. Subsequent annealing in vacuum allowed the elements to diffuse and precipitate out as nanometer-sized particles.

Ion implantation was the method of choice in this work for a variety of reasons stemming from both scientific and potential application considerations. Firstly, in order to investigate many properties of interest, such as size dependence of the bandgap, precise control must be maintained over the nanocrystal size distributions. Ion implantation allows precise setting of the resulting film composition by adjusting the implantation energy and the implantation dose. Multiple implants at different energies are possible in order to form a film with an arbitrary concentration profile. In addition, ion implantation is a standard technique used in VLSI semiconductor processing. Since we envision a potential for integrating nanocrystals on-chip with conventional electronics, a use of a VLSI-compatible process is a must. In fact, one application of Ge nanocrystals in SiO_2 formed by ion implantation and subsequent precipitation has already been demonstrated [1].

One potential drawback of the ion implantation technique is the damage to the matrix. One would expect that annealing at high enough temperature would allow the matrix to reconstruct [2], but for lower temperatures the presence of defects presents certain challenges, particularly in spectroscopic characterization of the samples, as will be described in the next chapter.

2.2 Synthesis of Ge nanocrystals.

Germanium nanocrystal samples for structural and Photoluminescence (PL) studies have been synthesized by ion implanting 100 nm thick thermal SiO_2 films with Ge at 70 keV at three different doses, 1×10^{16}, 2×10^{16}, and 5×10^{16} /cm^2, and by subsequent thermal annealing in vacuum at various temperatures ranging from 600 °C to 1200 °C. Ion implantation creates a supersaturated solid solution of Ge in the SiO_2 matrix, and annealing precipitates particles 2-10 nm in diameter, depending on annealing temperature. Figure 2.1 shows Ge concentration profiles in as-implanted samples, and after annealing at 700 °C for 30 minutes. A slight steepening of the concentration profile is observed for higher Ge content samples which is due to diffusion of atomic Ge into regions of higher particle density. These contain larger particles which act as Ge sinks and grow at the expense of smaller particles by coarsening.

2.3 Structural characterization of Ge nanocrystal samples.

Samples fabricated by the above method have been characterized by Raman spectroscopy and Transmission Electron Microscopy (TEM). Samples with the lowest Ge dose did not precipitate nanocrystals upon thermal annealing alone, although other work in our group indicates that they do precipitate under electron irradiation in the TEM

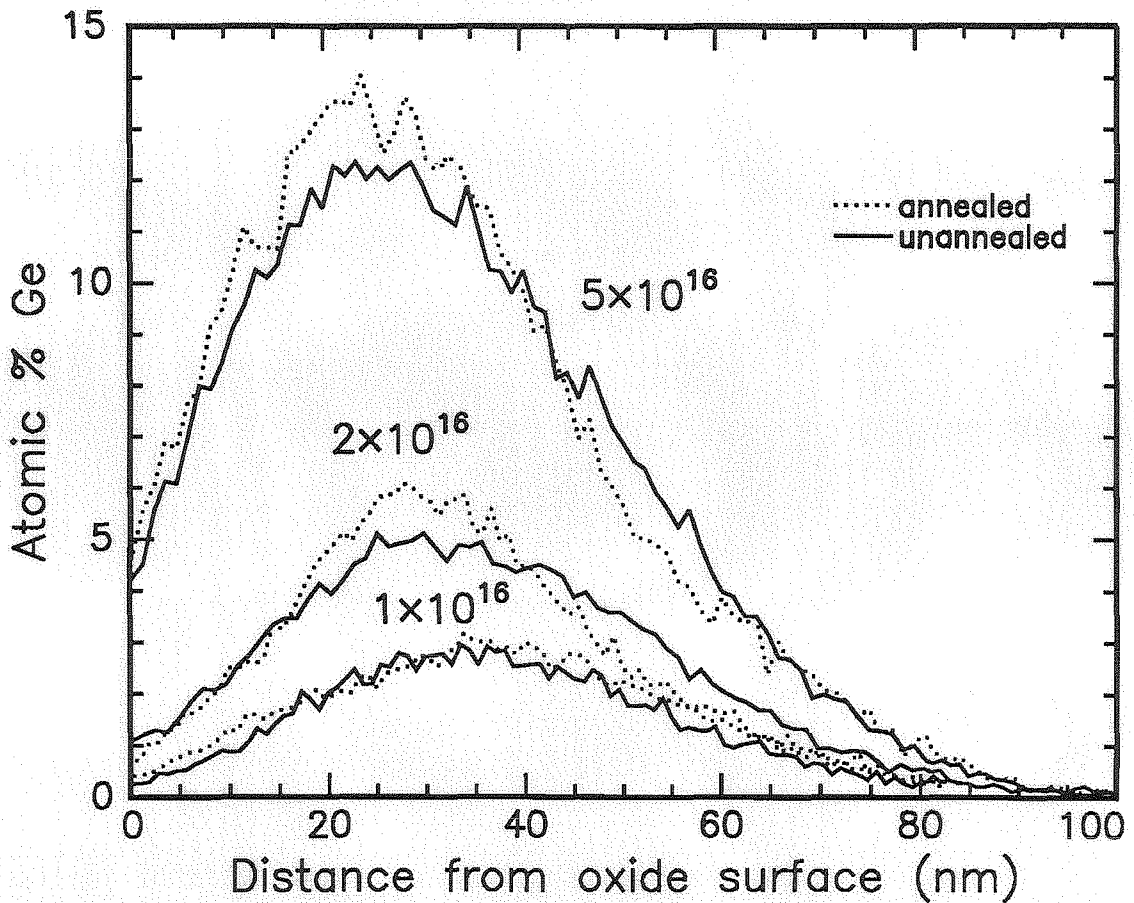

Figure 2.1 Ge concentration depth profiles after implantation and after subsequent annealing at 700 °C in vacuum for 30 minutes.

at elevated temperatures. This suggests that the solid solubility limit of Ge in thermal SiO_2 is on the order of the peak concentration for this sample, or about 3 atomic %. Results of varying annealing temperature for the middle dose sample are shown in Fig. 2.2. Mean particle diameters range from 2 nm for 600 °C anneals to 10 nm for 1200 °C. This is the size range where calculations [3,4] predict a significant variation of

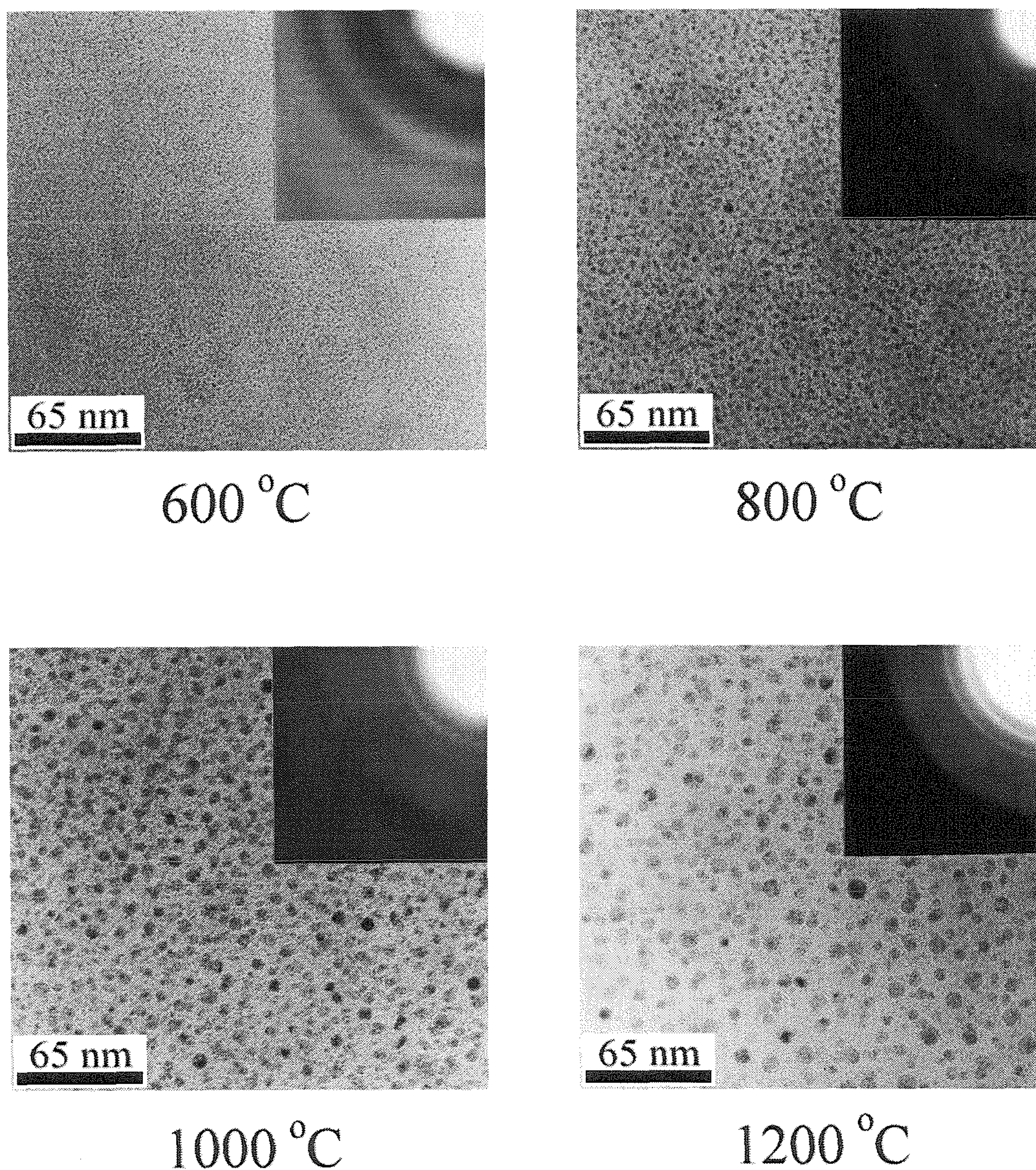

Figure 2.2 Bright field TEM micrographs of $2\times10^{16}/cm^2$ Ge implanted sample annealed at different temperatures. Significant control of particle size is possible simply by varying the annealing temperature. Electron diffraction patterns for the samples are inset at the upper right corner of each image.

the bandgap with particle diameter. It is apparent that a significant degree of size control in this range is possible solely by varying the annealing temperature. Electron diffraction (Fig. 2.2) patterns indicate that the particles are in a diamond cubic crystalline phase. The broadening of the (220) and (311) diffraction rings for the two lower temperature anneals is consistent with the small particle size.

Figure 2.3 shows middle dose samples annealed at the same temperature for different lengths of time. Contrary to what one might expect from a simple coarsening behavior, the size distribution does not evolve significantly after about 2 minutes (the shortest anneal possible with our furnace). One possible explanation is a diffusion transient enhanced by the presence of defects in the matrix created by ion implantation [8]. Annealing 5×10^{16} /cm^2 samples resulted in particle size distributions almost identical to those for the middle dose (Fig. 2.4), although with a considerably higher particle density.

Figure 2.5 shows a High - Resolution TEM comparison of typical particles in a 600 °C sample and typical particles in a 1000 °C sample. Crystalline particles are clearly visible, and a number of twin boundaries in them is apparent as well.

A cross section of the 2×10^{16} /cm^2 Ge implanted sample is shown in Figure 2.6. Germanium nanocrystals near the middle of the film are clearly visible in both bright field (dark dots) and dark field (bright spots).

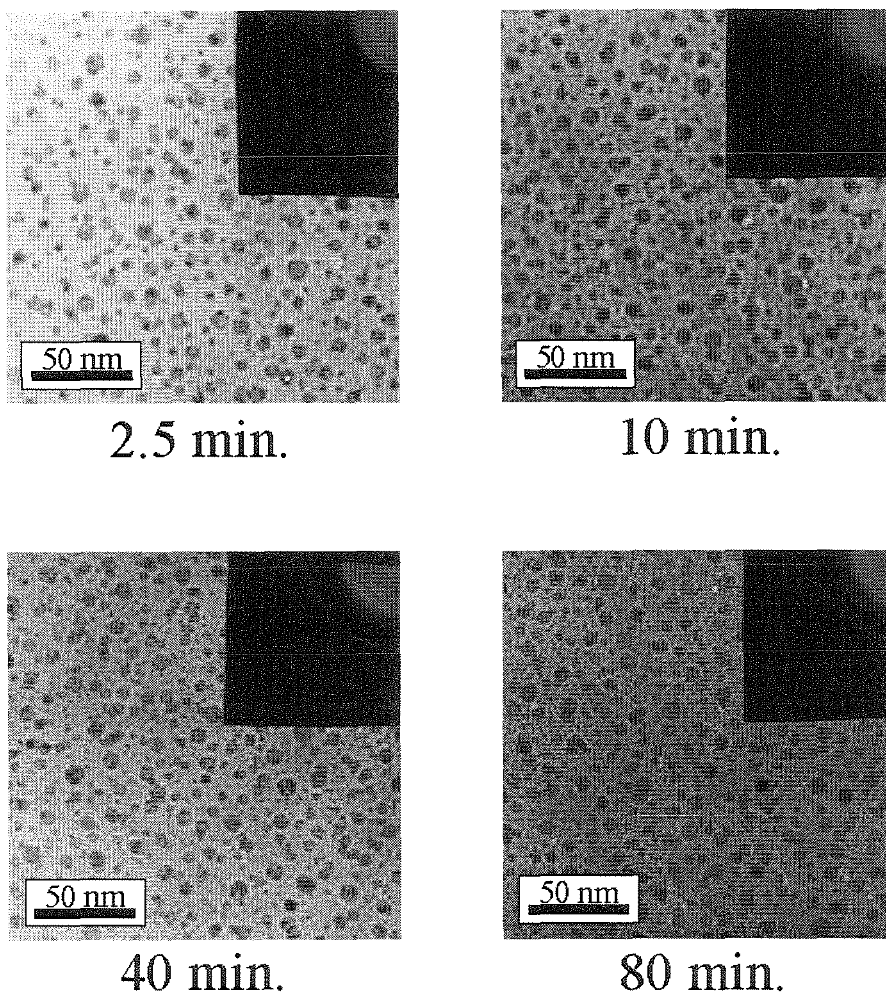

Figure 2.3 Middle dose samples annealed at 1000 °C for different lengths of time. No significant evolution of the particle size distribution is observed after the first 2.5 minutes of annealing.

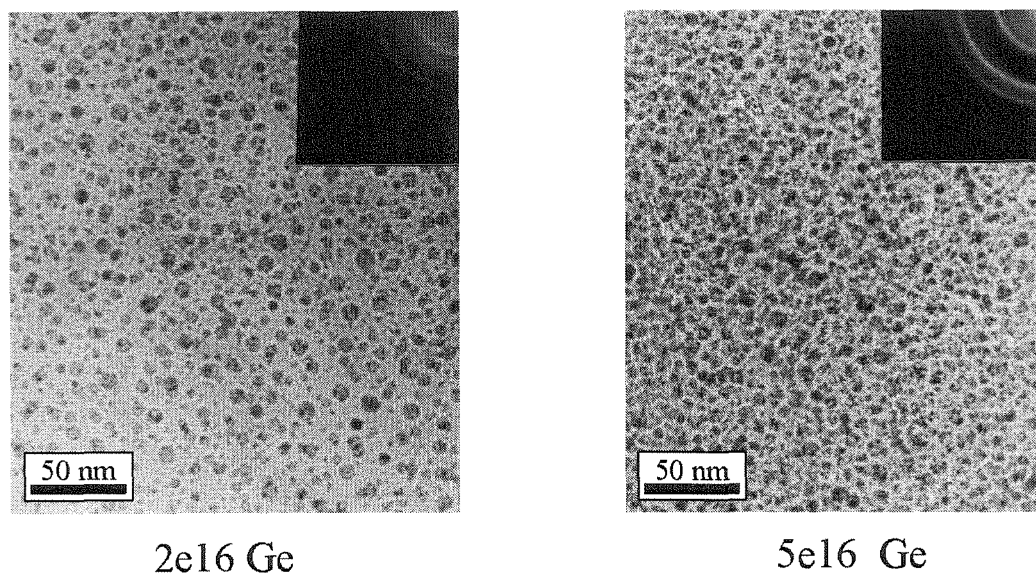

Figure 2.4 Bright field TEM micrographs of 2×10^{16} /cm^2 and 5×10^{16} /cm^2 Ge implanted samples annealed at 1000 °C. No significant change in average particle is seen, although a there is a dramatic increase in particle density.

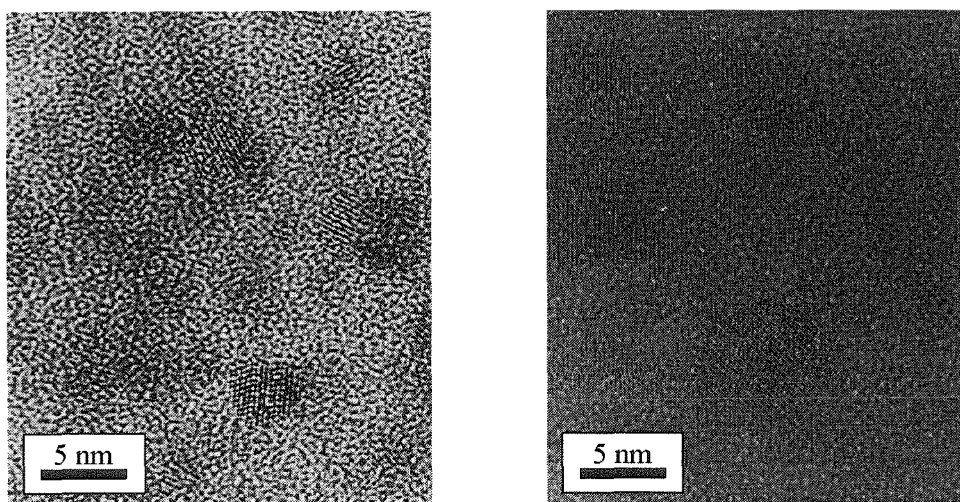

Figure 2.5 High resolution TEM images of the middle dose sample annealed at 600 °C and 1200 °C.

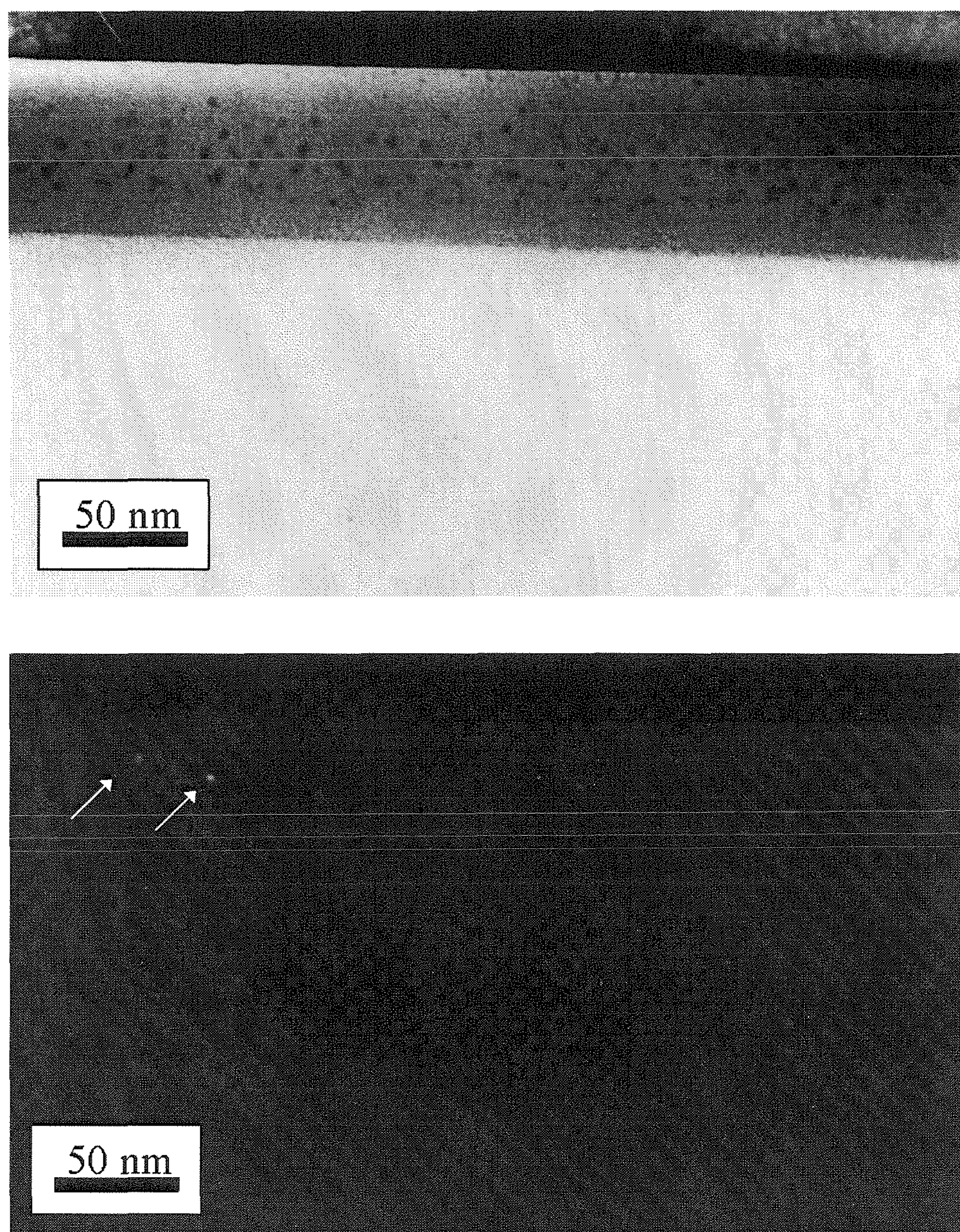

Figure 2.6 Cross-sectional bright-field (top) and dark-field (bottom) TEM images of the middle dose sample annealed at 800 °C. Nanocrystals are clearly visible in the middle of the oxide layer. Also visible is what appears to be some Si crystallites on the oxide surface. These may be responsible for the luminescence in the yellow part of the spectrum.

Raman scattering experiments were also performed on both Ge and Si implanted samples. Figure 2.7 shows a set of spectra for unannealed Ge and Si implanted samples and those annealed at 700 °C. One observes a general amorphous Ge shoulder around 300 cm^{-1} extending to lower energies which grows out into a broad peak centered around 300 cm^{-1} upon annealing. While some groups have attempted to use the width of the Raman peak as a measure of average particle size [9,10], this method is inherently unreliable since the broadening may be inhomogeneously dominated by surface effects which are important for particles of such small size, as well as by inhomogeneous hydrostatic stresses in the matrix. It is therefore difficult to obtain any information from the Raman spectra besides the qualitative conclusion that crystalline particles precipitate upon annealing.

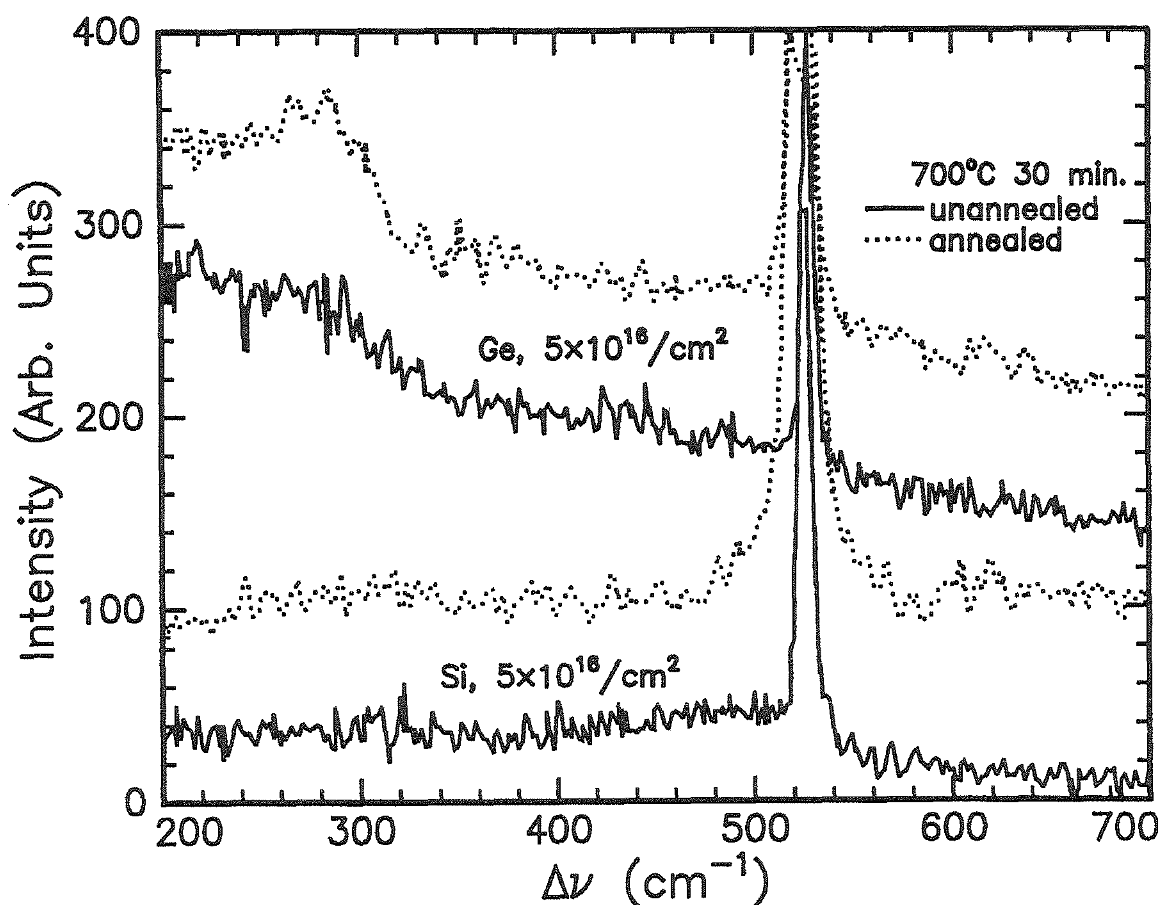

Figure 2.7 Raman scattering spectra of Ge- and Si-implanted samples before and after annealing at 700 °C.

2.4 Ge nanocrystal size distributions.

The bright field TEM images in fig. 2.2 were used to count Ge nanocrystal size distributions. The actual counted data for the four annealing temperatures is shown in figure 2.8, as well as the gaussian fits to that data. We obtain average nanocrystal diameters of 1.9 nm, 3.2 nm, 7.2 nm, and 8.4 nm with full widths at half-maximum of 1.5, 3.4, 4.0 and 4.3 nm respectively for 600, 800, 1000, and 1200 °C anneals. These fits will be used in the next chapter to generate a set of predicted PL spectra using the bandgap and radiative rates as a function of size calculated by in reference [3].

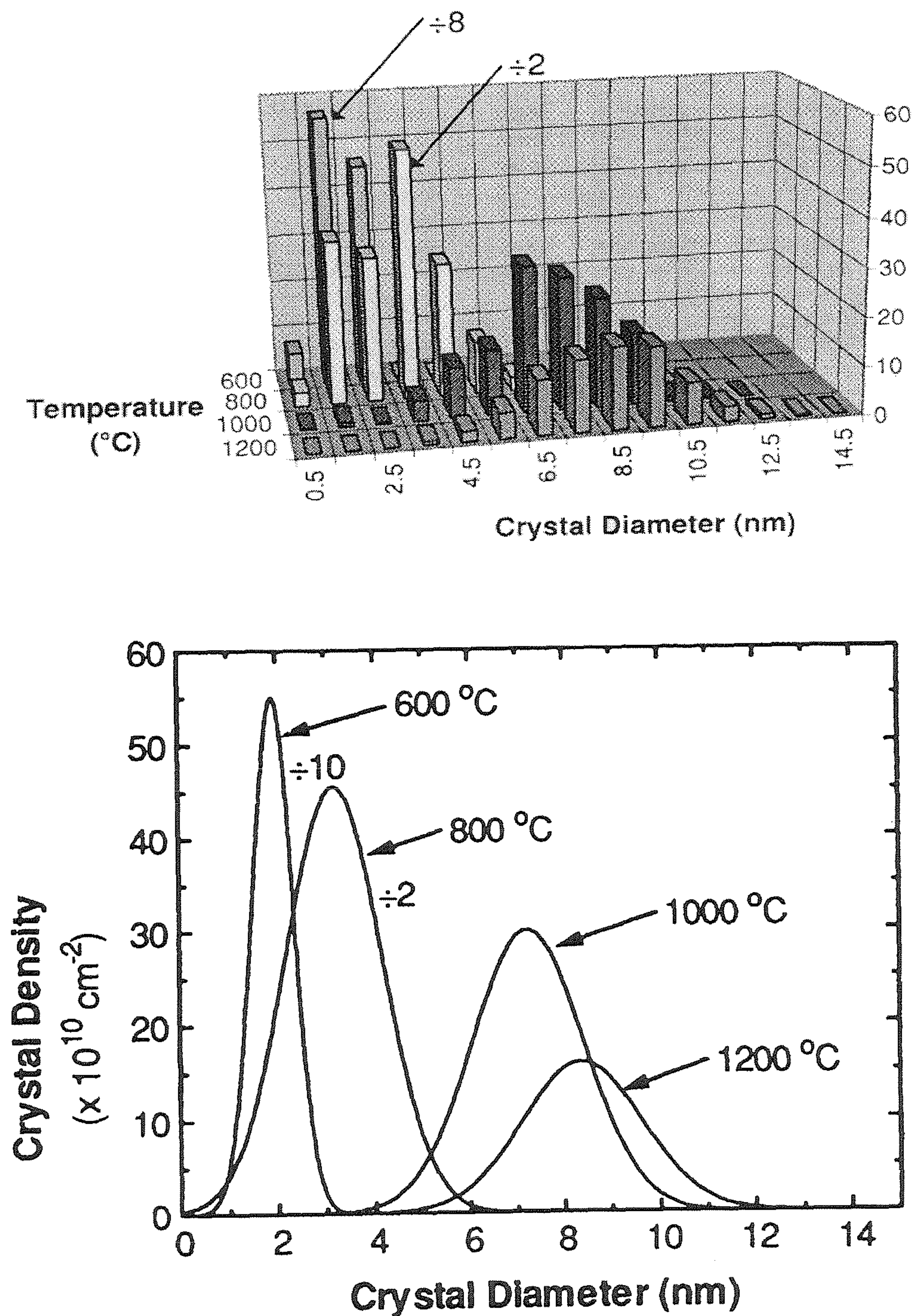

Figure 2.8 Tabulated nanocrystal size distributions based on TEM data in Fig. 2.2 (top) and gaussian fits to the histograms. The fits were used to generate the calculated PL spectra in chapter 3.

2.5 Synthesis of Si nanocrystals.

Silicon nanocrystals in an SiO_2 matrix were synthesized by a similar method. 100 nm thick thermal SiO_2 films were implanted with Si at 50 keV at three different doses, 1×10^{16}, 2×10^{16}, and 5×10^{16} /cm^2. The samples and by subsequent thermal annealing in vacuum at various temperatures ranging from 600 °C to 1200 °C.

RBS depth profiles could not be obtained since the excess few % of Si is difficult to observe on top of a large Si background from due to poor contrast of implanted Si from SiO_2.

2.6 Structural characterization of Si-implanted samples.

The only structural characterization possible for Si-implanted samples turned out to be High-resolution TEM. Even here it was possible to see reasonable crystallinity only for the high-dose samples annealed at 1000 °C high temperature. This is due to poor contrast between these extremely small particles and the SiO_2 matrix since the electronic densities of the two materials are sufficiently close. Figures 2.9 and 2.10 show a comparison of Ge and Si -implanted middle and high dose samples annealed at 1000 °C. While in Ge-implanted samples nanocrystals are clearly visible, in the Si-implanted samples one observes small crystallites in the high-dose sample. They are in the 2-4 nm diameter range, a range where calculations predict a substantial increase of bandgap and radiative recombination rate [3,5-7]. In the middle dose sample, while the pattern is not exactly amorphous, and one may be convinced that there are a few lattice fringes here and there, the image is inconclusive. It is highly probable that crystallites below 3 to 4 nanometers in diameter simply do not resolve due to poor contrast.

Raman spectra shown for Si-implanted samples in Figure 2.7 besides suffering from the general maladies described earlier, are dominated by the strong bulk substrate Si-Si stretch. One notices the disappearance of a week shoulder extending to lower energies and an appearance of a week broad feature centered about the bulk peak. Again, no quantitative information can be extracted from these spectra.

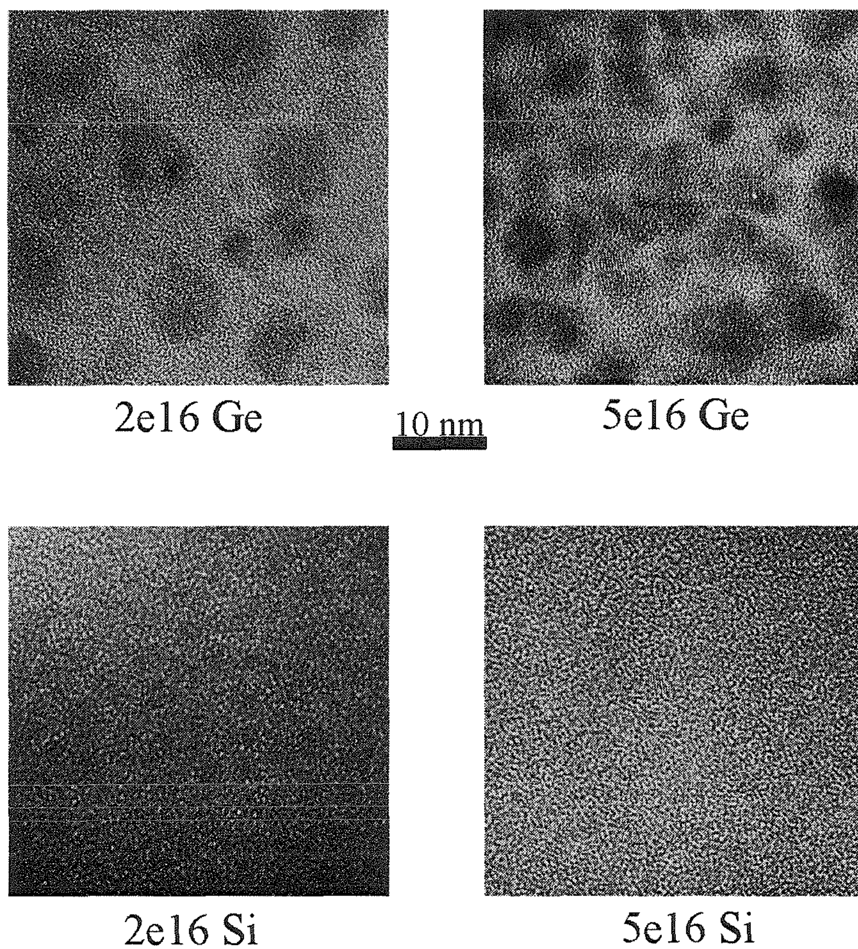

Figure 2.9 High resolution TEM images of middle and high dose Si and Ge implanted samples annealed at 1000 °C

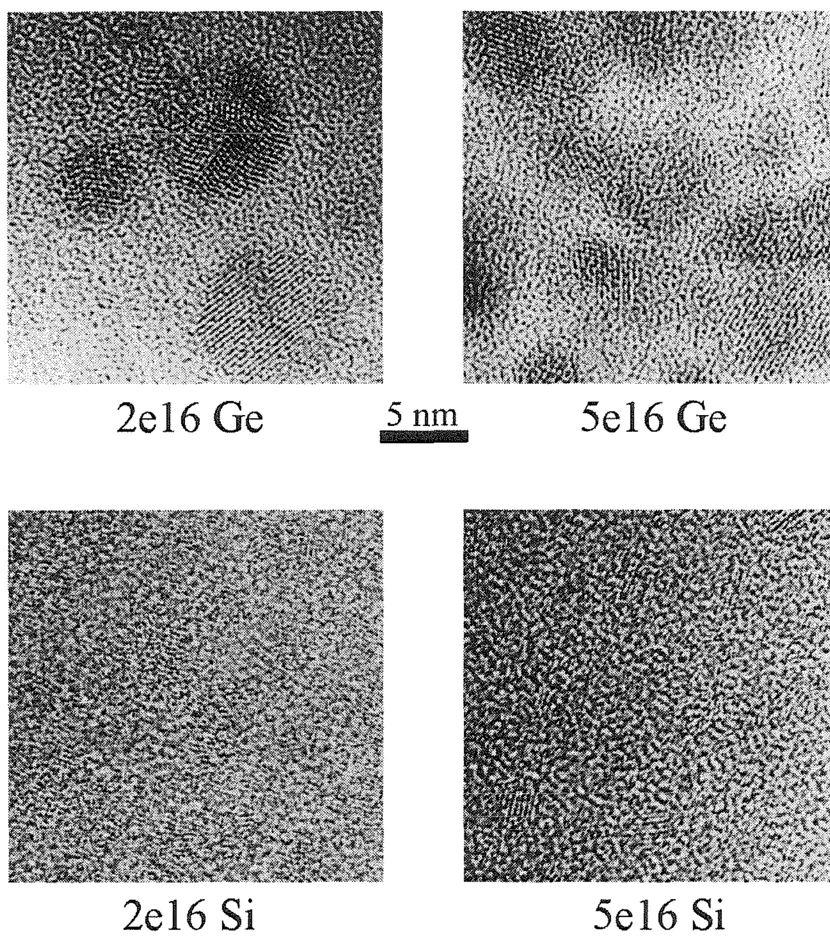

Figure 2.10 Images of Fig. 2.9 at higher magnification showing individual nanocrystals.

2.7 Synthesis of Sn and SnGe implanted samples.

A possibility of forming optically active Sn and SnGe alloyed nanocrystals was investigated as well. Sn nanocrystal samples were made by implanting 100 nm thick thermal SiO_2 films with Sn at 100 keV at 2×10^{16} /cm^2 and by subsequent thermal annealing in vacuum at various temperatures ranging from 400 °C to 800 °C. Samples for alloyed nanocrystal studies were fabricated by co-implanting Sn at 100 keV and Ge at 70 keV at two sets of doses, 2×10^{16} /cm^2 and 2×10^{16} /cm^2 Sn, and 4×10^{16} /cm^2 Ge and 1×10^{16} /cm^2 Sn. These samples were subsequently annealed in vacuum as well, at temperatures between 400 °C to 800 °C. Samples fabricated by the above method have been characterized by Raman spectroscopy and Transmission Electron Microscopy (TEM). Electron diffraction patterns were indexed using the adventitious Si substrate (200) diffraction spots as the calibration.

2.8 Structural characterization of Sn and SnGe implanted samples.

Figure 2.11 shows a bright and dark field pair of the Sn-implanted sample annealed at 800 °C. Large nanocrystals 15-20 nm are clearly visible both in bright field and in dark field. Electron diffraction pattern indicates that the nanocrystals are mostly the β phase of tin (Table 2.1 summarizes the diffraction patterns of the samples). There were two diffraction rings that could not be attributed to either tin phase. These rings corresponded to 3.96 Å and 2.36 Å interplanar spacings, which are closest to the α tin phase (111) and (220) rings (theoretical spacings of 3.75 Å and 2.29 Å respectively), although the absence of diamond cubic (200) and (311) reflections, particularly of the (200), argue strongly against this assignment. Another possibility may be a formation of tin oxide in some parts of the film.

Table 2.1 Summary of Sn and SnGe diffraction data.

Interplanar spacing d (Å) for sample				
$2\times10^{16}/cm^2$ Sn, ann. at 800 °C.	$4\times10^{16}/cm^2$ Ge, $1\times10^{16}/cm^2$ Sn, ann. at 800 °C.	$2\times10^{16}/cm^2$ Ge, $2\times10^{16}/cm^2$ Sn, ann. at 600 °C.	Possible attribution	Calculated d (Å)
---	4.47	4.60	??? α–Sn (110) (forbiddden)	4.59
4.14	4.07	4.03	β- Sn (110); β- SnGe?	4.123
3.93	3.91	---	α-Sn (111)? oxide?	3.75
2.90	---	---	β- Sn (200)	2.92
2.83	2.86	2.88	β- Sn (101) Ge(200)	2.79 2.83
---	2.41	2.40	β- SnGe (111)? strained Sn?	2.52 for Sn (111)
2.33	2.35	---	α-Sn (220)? oxide?	2.29
2.09	2.10	---	β- Sn (201)	2.15
2.03	2.04	2.06	β- Sn (220) β- Sn (211)	2.06 2.02
1.83	1.83	1.84	β- Sn (310)	1.84
1.71	1.70	1.71	β- Sn (221) Ge (311)	1.73 1.71

Figure 2.12 shows a HREM image of the sample. Large crystalline nanocrystals are clearly visible.

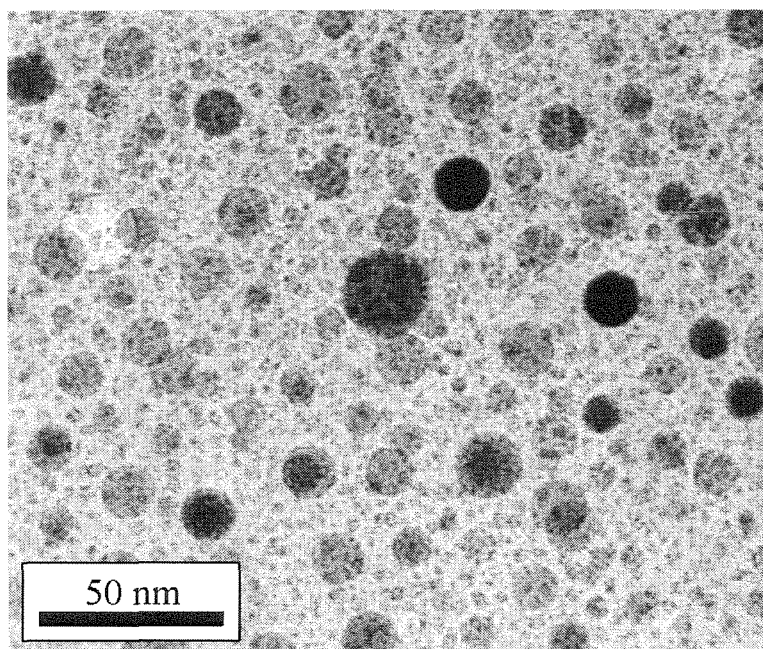

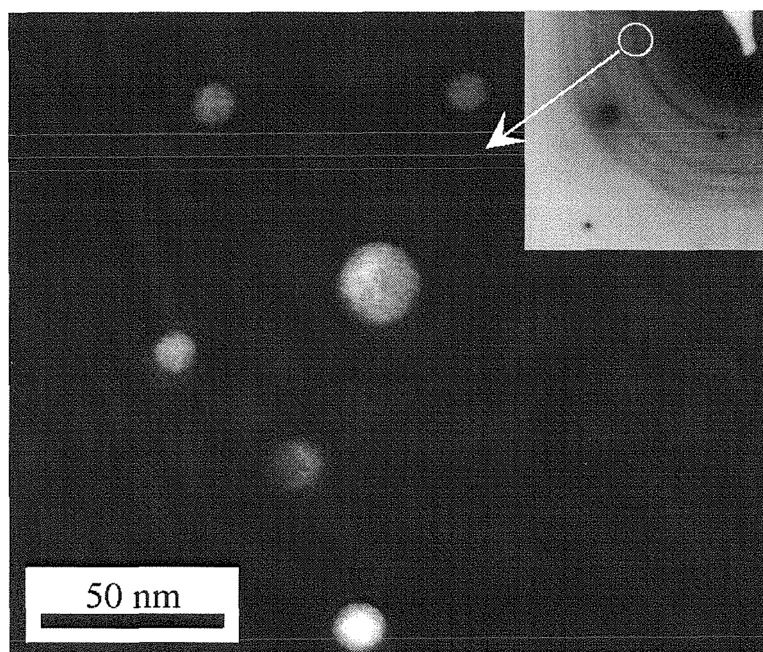

Figure 2.11 Bright and dark field TEM image pair of the 2×10^{16} /cm^2 Sn implanted sample annealed at 800 °C.

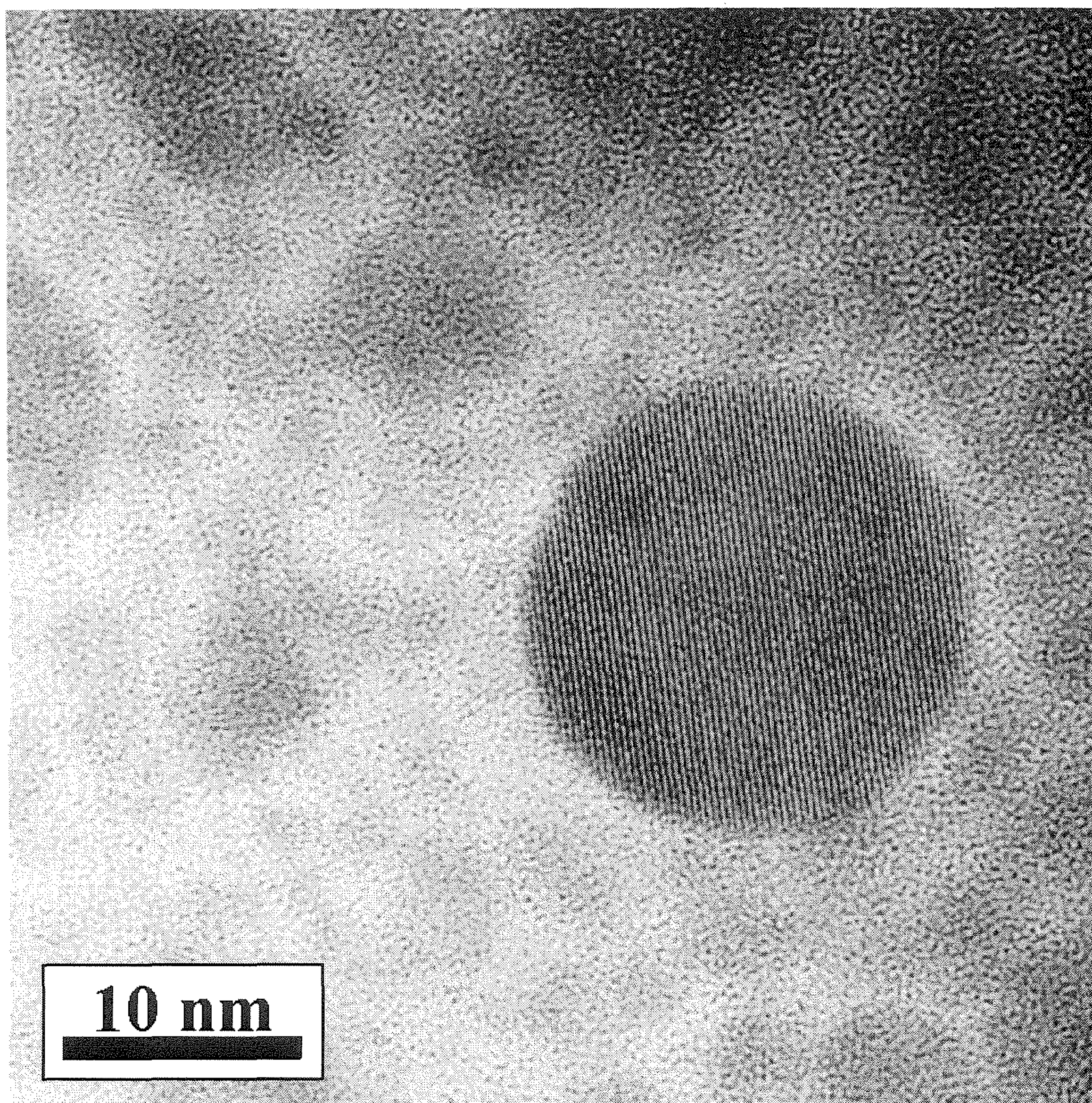

Figure 2.12 HREM image of the 2×10^{16} /cm^2 Sn implanted sample annealed at 800 °C.

Co-implanted samples present a much more interesting microstructure. Although 4×10^{16} /cm^2 Ge and 1×10^{16} /cm^2 Sn co-implanted sample annealed at 600 °C (figures 2.13 and 2.14) presents a microstructure similar to than of the Ge implanted samples annealed at similar temperatures, the same sample annealed 800 °C shows a number of interesting structures, such as coalesced Sn and Ge nanocrystals and "onion" structures, with what looks like alternating shells and Ge and Sn (figures 2.15 and 2.16). In addition, atomic scale registry is observed across the Sn-Ge interface, a nanoscale version of epitaxy. HREM image of the 2×10^{16} /cm^2 Ge and 2×10^{16} /cm^2 Sn co-implanted sample annealed at 600 °C (figure 2.17) shows an even more striking example of this nanocrystal "epitaxy".

Electron diffraction patterns of these co-implanted samples (table 2.1) contain rings that cannot be attributed to known Sn and Ge phases. Two possibilities exist, either the epitaxial arrangement induces a significant amount of strain on both portions of coalesced nanocrystals, or a new phase has formed. The former explanation is more likely in view of the microstructure observed in TEM.

2.9 Raman scattering results.

Raman scattering results also indicate that some Ge-Ge bond lengths differ significantly from the bulk value. Figure 2.18 shows a set of Raman spectra of the co-implanted samples annealed at different temperatures. The spectrum for the 4×10^{16} /cm^2 Ge and 1×10^{16} /cm^2 Sn co-implanted sample annealed at 600 °C shows a wide shoulder extending from 290 cm^{-1} down to lower energies. Upon annealing of the same sample at 800 °C two distinct peaks appear, one at 284 cm^{-1}, and another at 300 cm^{-1}, the bulk Ge-Ge stretch energy. The former corresponds either to Ge-Ge in SnGe alloy or to Ge under tensile strain, which would be the case if Ge was epitaxial on Sn. This effect is well known for strained III-V thin films as well as for strained SiGe films on Si substrates [11-13]. Figure 2.19 shows the Stokes shift of the Ge-Ge stretch in SnGe alloys grown by MBE as a function of Sn percentage. The Raman shift observed for nanocrystals corresponds to about 16 atomic % Sn in the alloy. The Alloy lattice constant would correspond to 5.65 Å as deduced from X-ray diffraction data for MBE-grown films [14].

Alternately, if the mechanism for this anomalous shift were the tensile strain, the Ge-Ge bond length would correspond to 2.42 Å, a value obtained from first-principles density functional calculations[14]. Annealing at higher temperatures causes this peak to grow in intensity, an effect that is yet unexplained, but may be related to alloying of large percentage of Sn and Ge in the film.

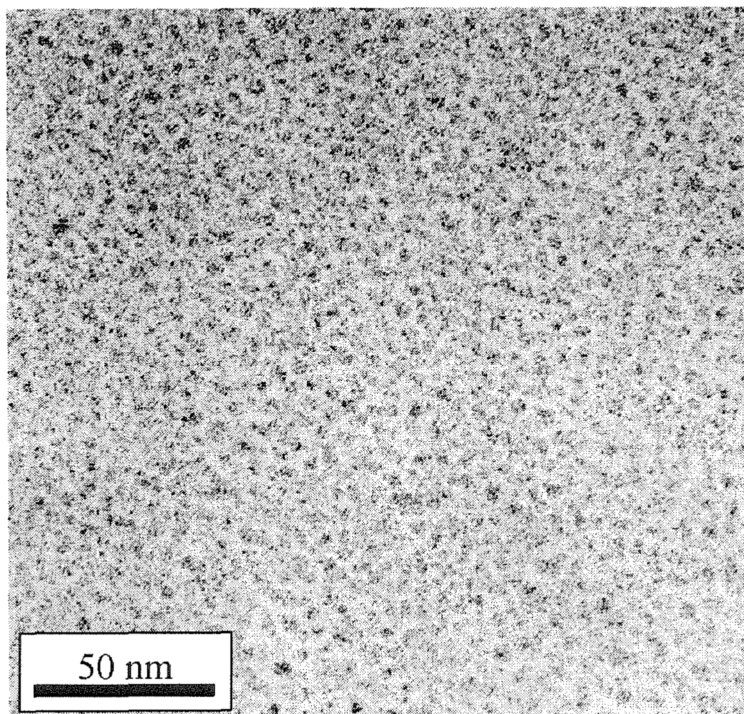

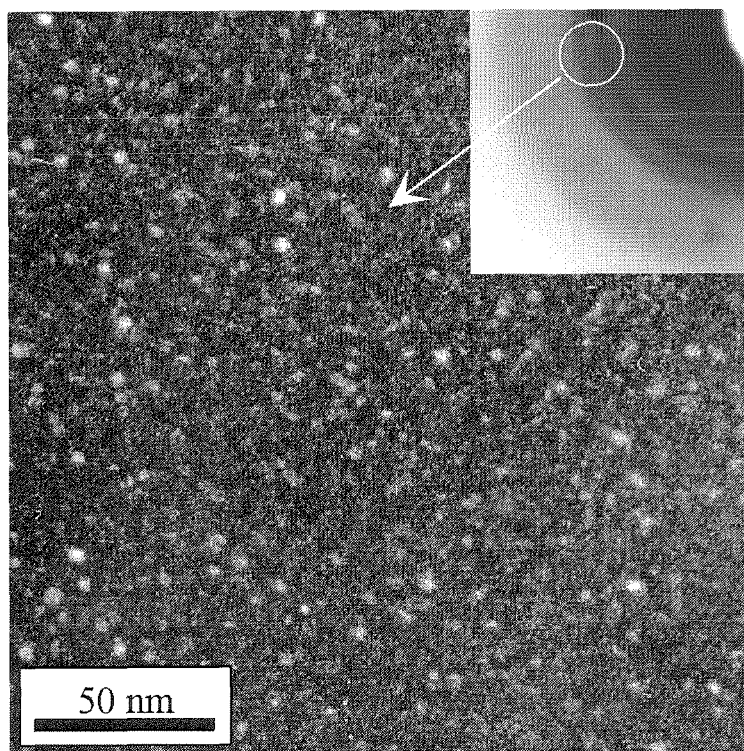

Figure 2.13 Bright and dark field TEM image pair of the 4×10^{16} /cm^2 Ge and 1×10^{16} /cm^2 Sn co-implanted sample annealed at 600 °C.

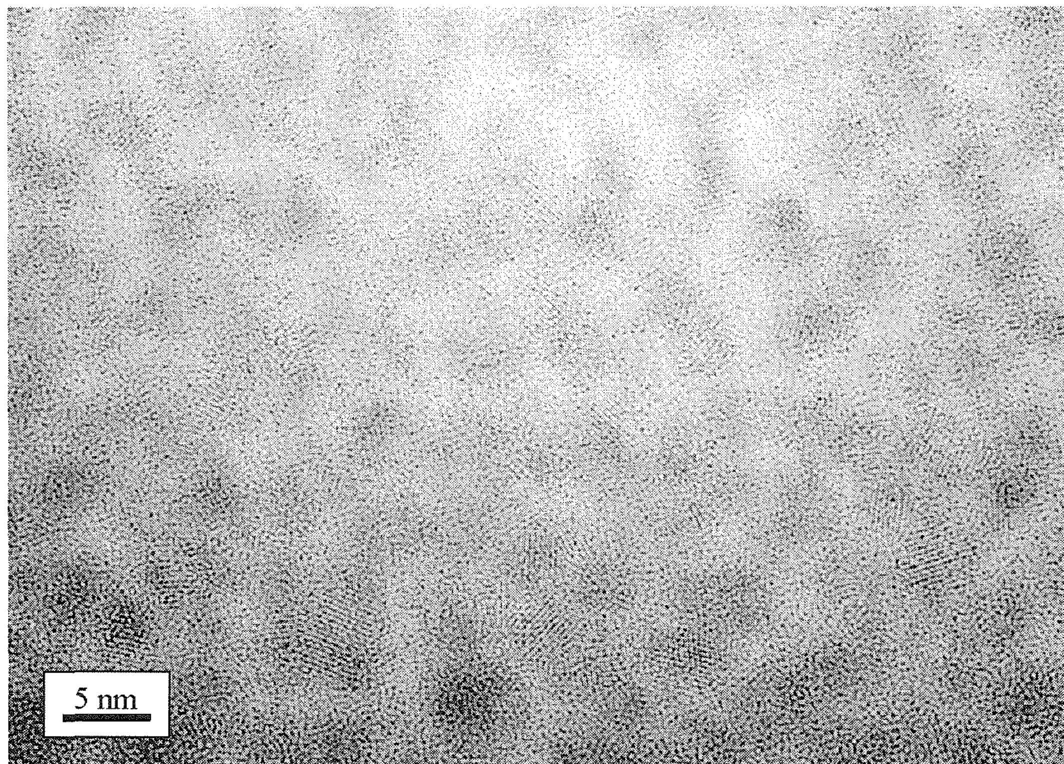

Figure 2.14 HREM image of the 4×10^{16} /cm^2 Ge and 1×10^{16} /cm^2 Sn co-implanted sample annealed at 600 °C.

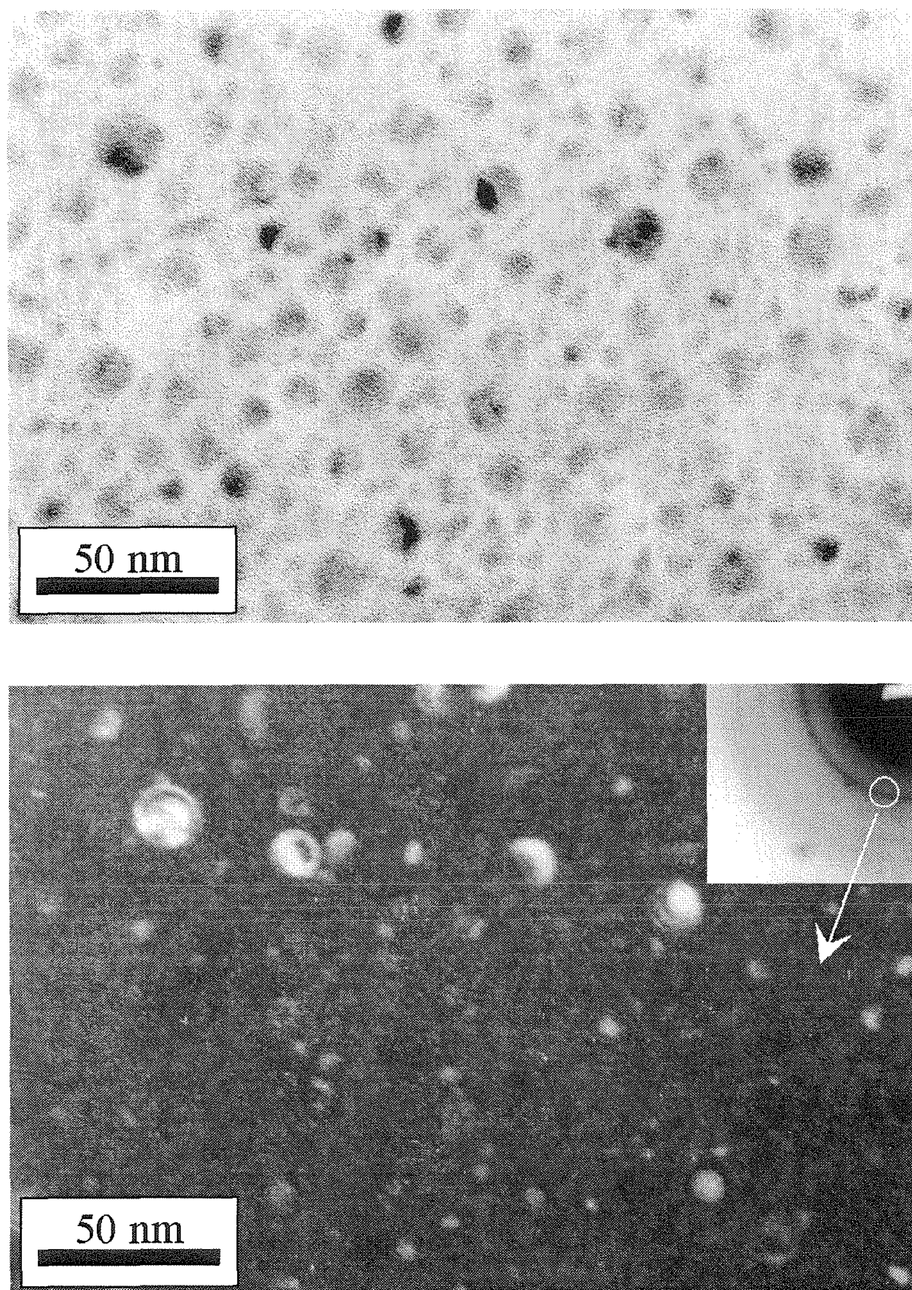

Figure 2.15 Bright and dark field TEM image pair of the 4×10^{16} /cm^2 Ge and 1×10^{16} /cm^2 Sn co-implanted sample annealed at 800 °C. A number of Sn and Ge coalesced nanocrystals is visible in both bright and dark field. There appear to be some "onion" structures as well.

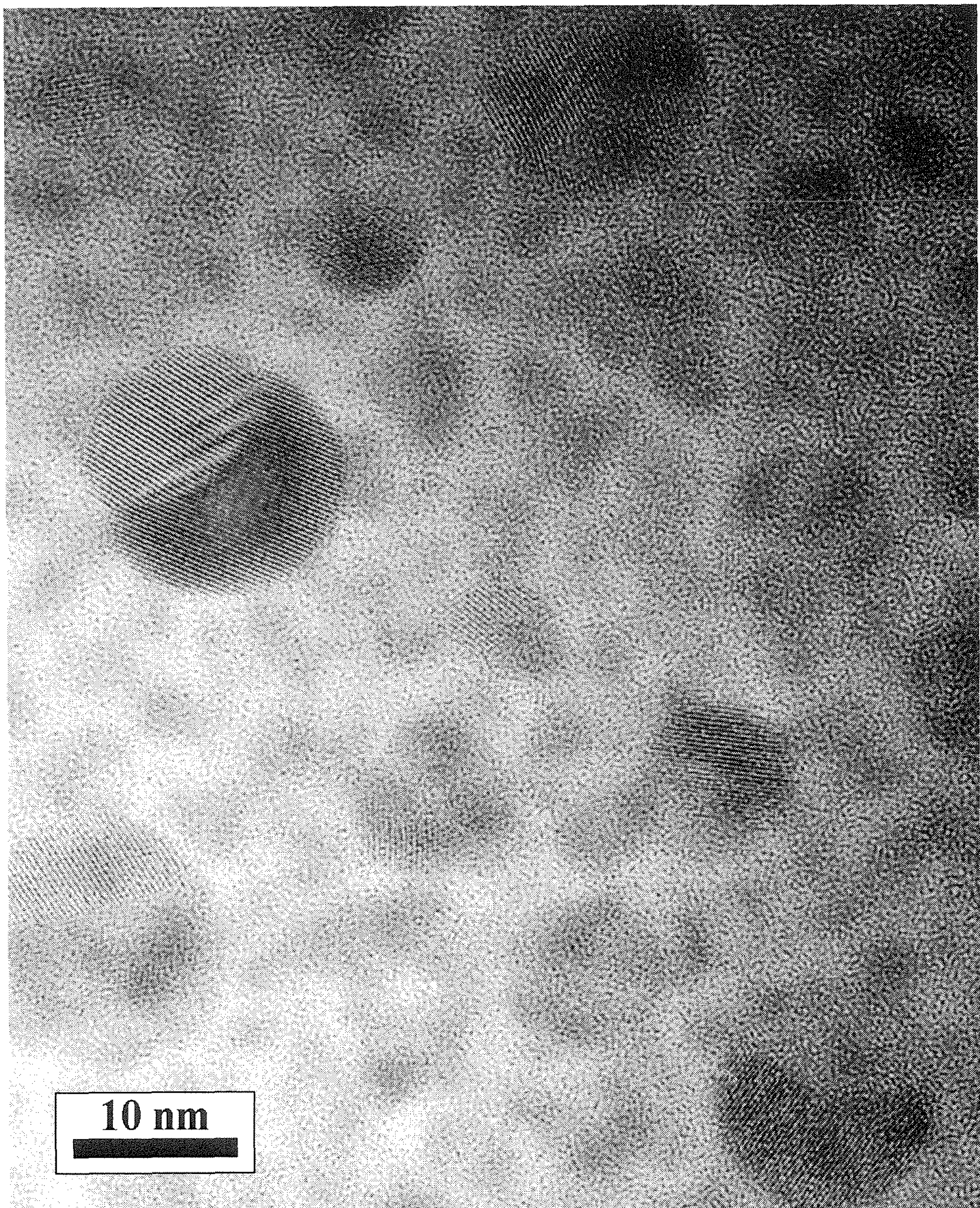

Figure 2.16 HREM image of the 4×10^{16} /cm^2 Ge and 1×10^{16} /cm^2 Sn co-implanted sample annealed at 800 °C. A number of Sn and Ge coalesced nanocrystals is visible. It appears that in the well-resolved nanocrystal on the middle-right there is lattice alignment between Sn and Ge portions. In a sense we have epitaxial growth.

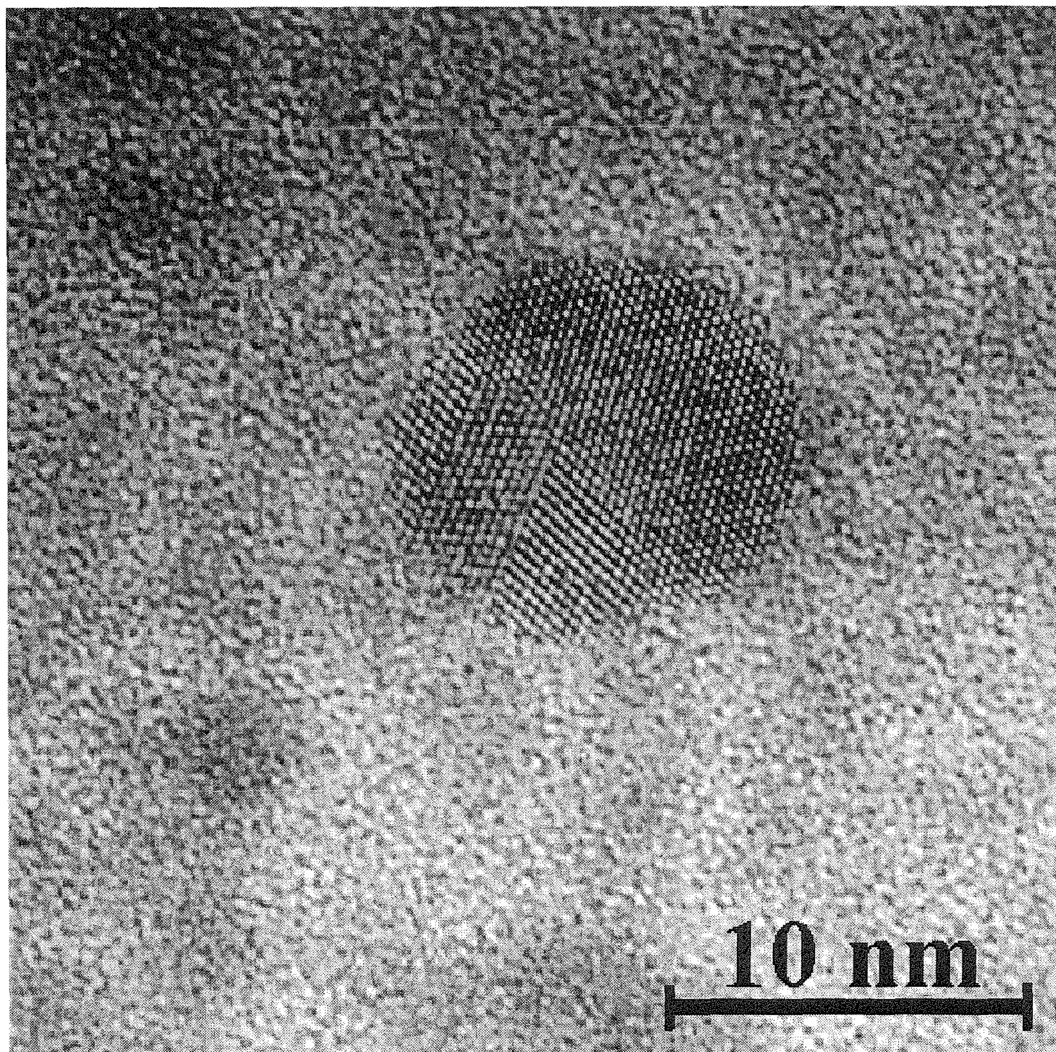

Figure 2.17 HREM image of the 2×10^{16} /cm^2 Ge and 2×10^{16} /cm^2 Sn co-implanted sample annealed at 600 °C. Here lattice fringes have resolved in both directions. We are seeing (111) lattice planes for Ge and either (111) planes for α-Sn or (101) planes for β-Sn. There is perfect registry across the interface, although two twins are visible in the Ge portion.

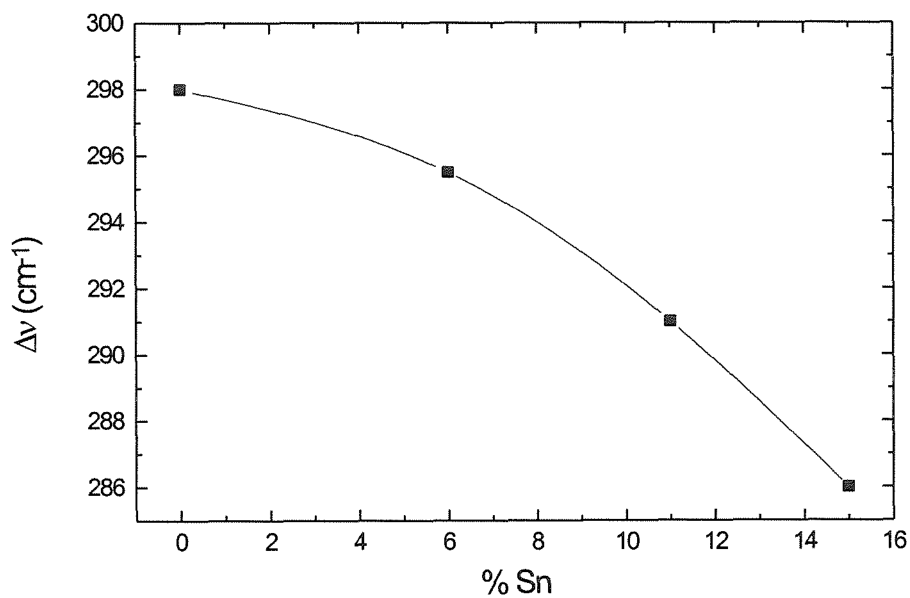

Figure 2.18 Raman scattering spectra of the Sn_xGe_{1-x} alloy films grown by MBE for different Sn concentrations.

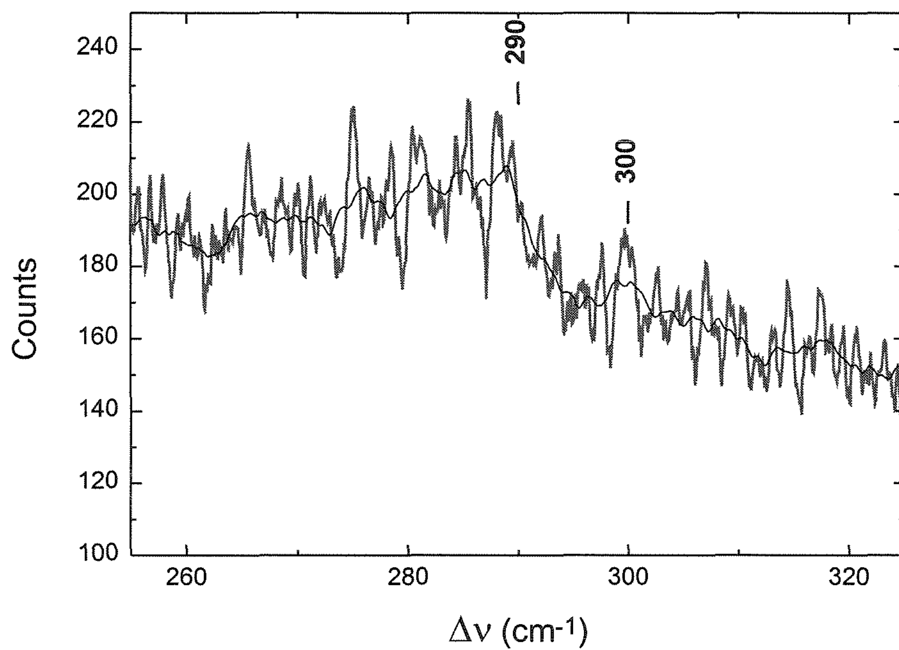

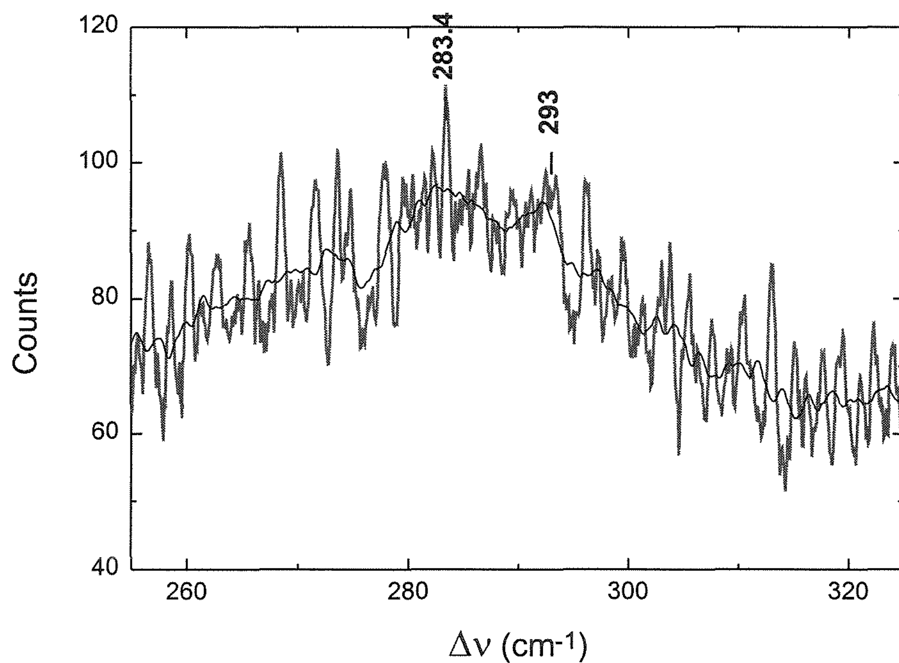

Figure 2.19 Raman scattering spectra of the 4×10^{16} /cm^2 Ge and 1×10^{16} /cm^2 Sn co-implanted sample annealed at 600 °C (a) and 800 °C (b).

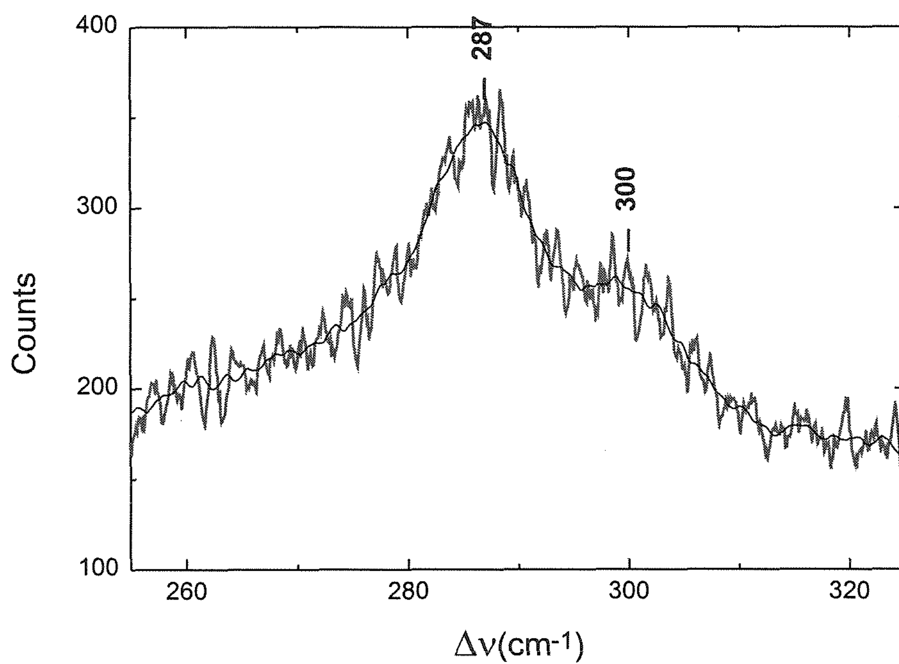

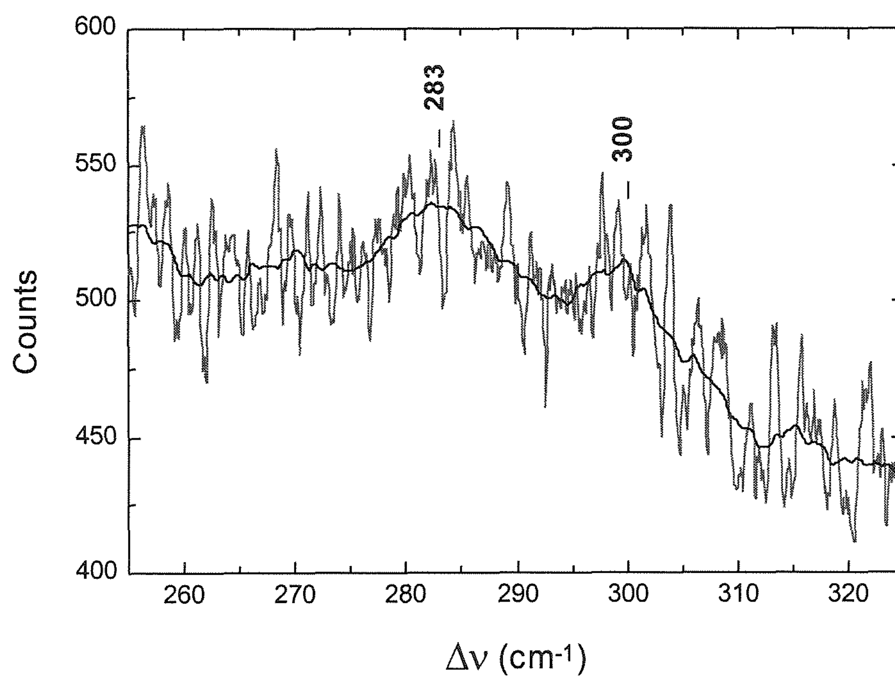

Figure 2.19 Raman scattering spectra of the 4×10^{16} /cm^2 Ge and 1×10^{16} /cm^2 Sn co-implanted sample annealed at 1000 °C (c) and 2×10^{16} /cm^2 Ge and 2×10^{16} /cm^2 Sn annealed at 600 °C (d).

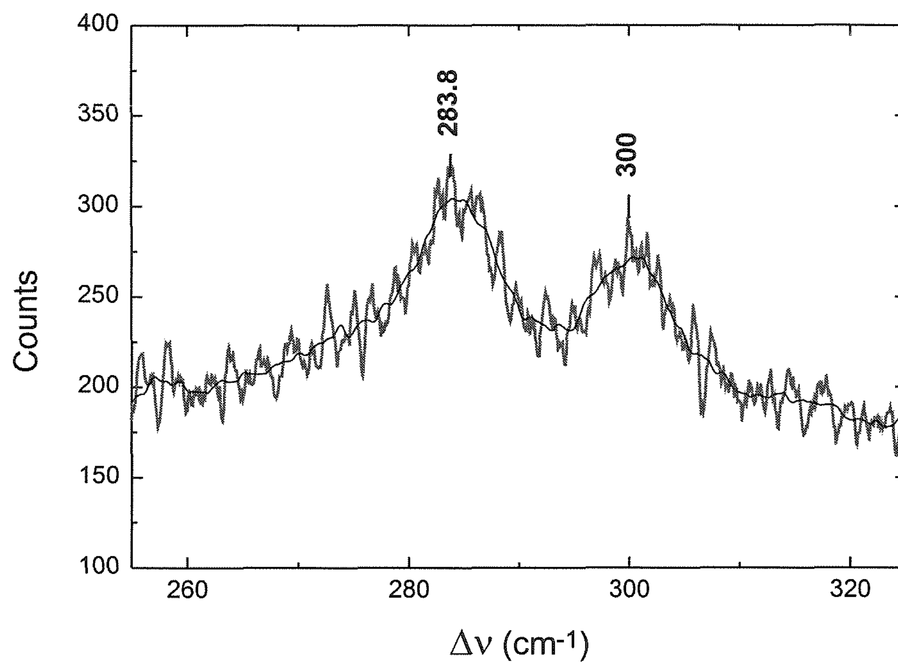

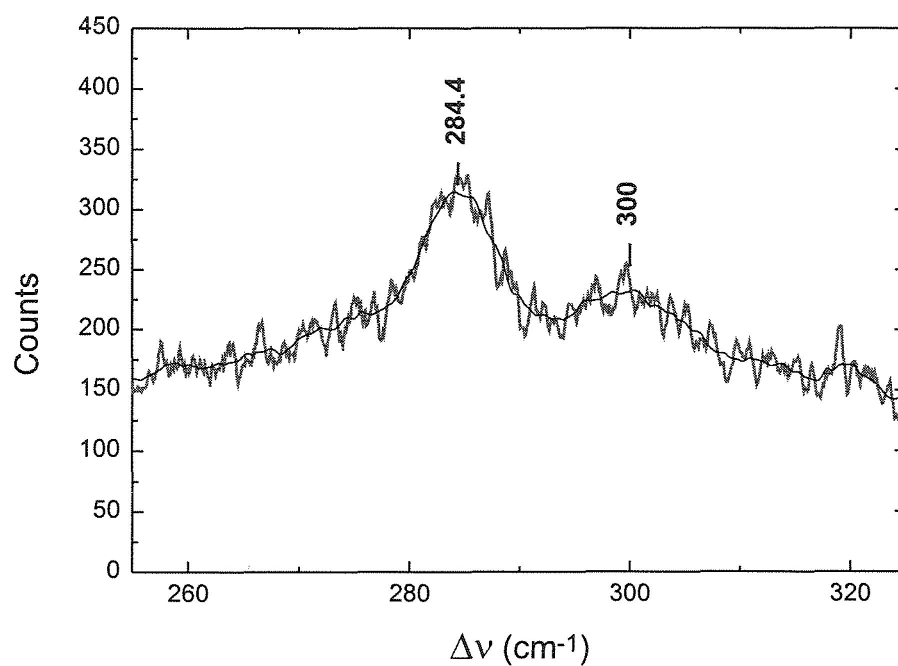

Figure 2.19 Raman scattering spectra of the 2×10^{16} /cm^2 Ge and 2×10^{16} /cm^2 Sn co-implanted sample annealed at 800 °C (e) and 1000 °C (f).

2.10 Conclusions.

We have fabricated and characterized structurally Si, Ge, and Sn nanocrystals in an SiO_2 matrix by ion implantation and precipitation through thermal annealing. It was discovered that the average Ge nanocrystal size can be effectively controlled by varying the annealing temperature. Nanocrystal size distributions were obtained for Ge nanocrystal samples annealed at different temperatures from bright field TEM micrographs.

Si nanocrystals, although they did not resolve as well in TEM due to poor contrast, could be observed in high resolution TEM for the highest dose implant annealed over 1000 °C.

Samples implanted with Sn alone and anealed at 800 °C shower large crystallite over 20 nm in diameter, while samples co-implanted with Sn and Ge contained interesting microstructures, such as Sn nanocrystals "epitaxial" on Ge nanocrystals, as well as "onion"-like structures. Raman measurements on the co-implanted samples revealed a significant deviation of the Ge-Ge stretch energy from that of bulk Ge which may be due to either formation of an alloy phase, or to significant strain induced by "epitaxy".

References.

[1] H.I. Hanafi, S. Tiwari, and I. Khan, IEEE Trans.Electr. Dev. **43**, p.1553 (1996).

[2] C.W. White, C.J. McHargue, P.S. Sklad, L.A. Boatner, and G.C. Farlow, Materials Science Reports **4**, p. 41 (1989).

[3] T. Takagahara and K. Takeda, Phys. Rev. B **46**, p. 15578 (1992).

[4] N. A. Hill, Private Communication (1994).

[5] M.S. Hybertsen, Phys. Rev. Lett. 72, p.1514 (1994).

[6] B. Delley and E. F. Steigmeier, Phys Rev. B. **47**, p. 1397 (1993).

[7] N. A. Hill and K.B. Whaley, Phys. Rev. Lett. **75**, p.1130 (1995).

[8] C.M. Yang, Doctoral Dissertation, California Inst. of Techn. (1997).

[9] S. Hayashi, E. Nishimae, and K. Yamamoto, Proc. ISSPIC-6, Chicago M-061 (1992).

[10] M. Fujii, S. Hayashi, and K. Yamamoto, Jap. J. Appl. Phys. **30**, p.687 (1991).

[11] S. Perkowitz, "*Optical Characterization of Semiconductors: Infrared, Raman and photoluminescence spectroscopy*" San Diego: Academic Press p. 115 (1993).

[12] A. Freundlich, G. Neu, A. Leycuras, R. Carles, and C. Verie, Mat. Research Symp. Proc. 116, pp.251-256 (1988).

[13] G. Abstreiter, K. Eberl, E. Friess, U. Menczigar, W. Wegscheider, and R. Zachai, *Spectroscopy of Semiconductor Microstructures, Series B: Physics* **206**, New York: Plenum Press, pp.165-174 (1989).

[14] G. He, Doctoral Dissertation, California Inst. of Techn., (1997).

Chapter 3
Luminescence properties of Ge and Si nanocrystals

3.1 Introduction.

Photoluminescence spectroscopy is a simple and powerful method for characterizing the bandgap of semiconductor materials. The sample is illuminated by a light source with photon energy larger than the bandgap of the material (typically in the blue or in the UV), and spectrally resolved luminescence is recorded. Direct bandgap semiconductors exhibit characteristic luminescence around the bandgap energy since the carrier relaxation to the band edge typically much faster than the carrier recombination time. This method should indicate whether the bandgap shifts as a function of nanocrystal size as predicted by theory and simulations. Many groups have used this technique to try to characterize Ge nanocrystals in SiO_2 fabricated by various methods described in Chapter 1 [1-14]. However, extensive structural characterization described in Chapter 2 was not available, and thus a thorough comparison could not be made.

3.2 Theoretical predictions.

There are a few theoretical predictions concerning the bandgap of Ge nanocrystals as a function of nanocrystal size [15,16]. A summary is shown in Fig. 3.1. While there is some variation in the exact numbers, the general trend is common to all, that the excitonic energy of Ge nanocrystals will increase with decreasing nanocrystal diameter due to quantum confinement effects (i.e., for nanocrystal sizes comparable or smaller than the

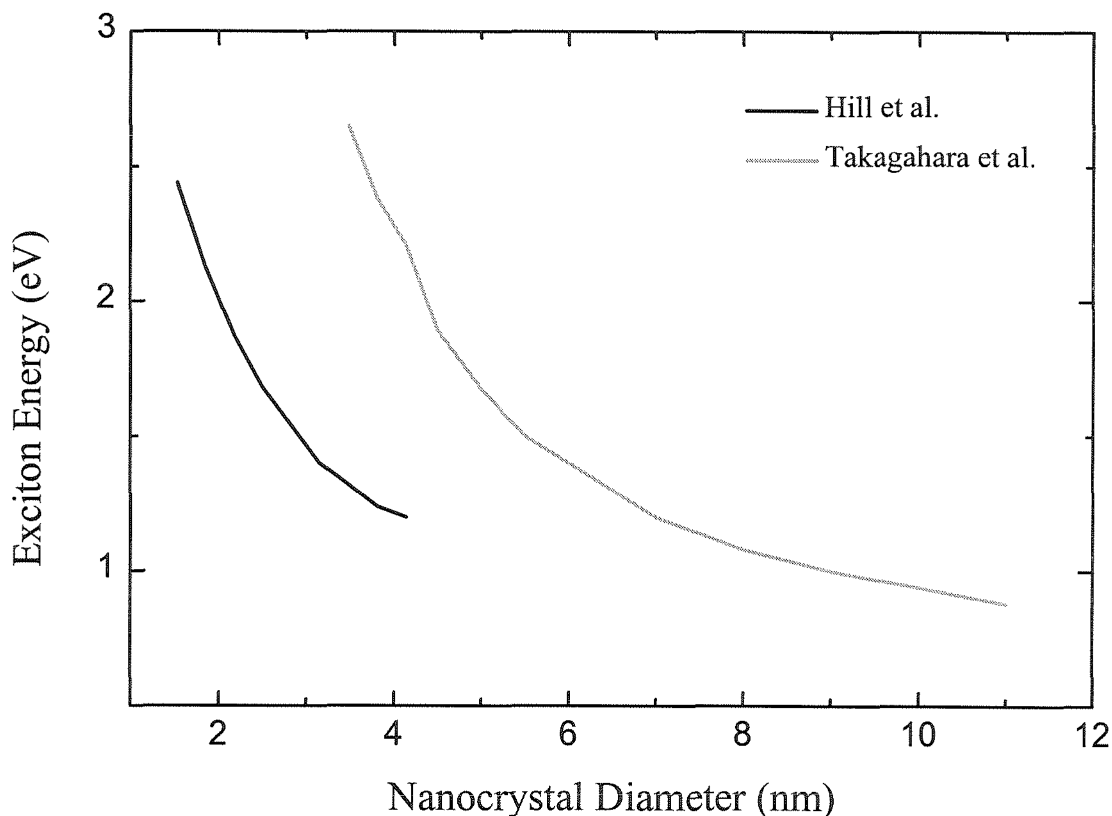

Figure 3.1 Summary of predicted bandgap data as a function of size for Ge nanocrystals from references [15,16].

excitonic radius in Ge). The excitonic confinement energy is expected to increase as well, leading to relatively stable excitons at room temperature for nanocrystals below 5-6 nm in diameter. We would thus expect the luminescence to blue-shift and increase in magnitude for samples with decreasing nanocrystal size. A few complications which will be discussed more thoroughly in later sections deserve to be mentioned here. First, an almost exponential increase of radiative excitonic lifetime with decreasing nanocrystal diameter will favor smaller nanocrystal sizes. On the other hand, absorption efficiency will generally be proportional to the nanocrystal volume, and will thus favor larger nanocrystal sizes. As a result of the interplay of these two factors, the peak of the

luminescence spectrum will not necessarily correspond to the average nanocrystal bandgap, and a slightly more involved treatment is necessary to compare experimental spectra with theoretical predictions for the bandgap and radiative lifetimes.

3.3 Experimental procedure.

Luminescence spectra were measured using a CCD Optical Multichannel Analyzer with a .25 m single grating spectrometer. The samples were pumped by 30-100 mW of the Argon Ion 457.9 nm laser line. A filter with a 505 nm cutoff wavelength was used to cut out stray laser light. The system had a 4 nm resolution and was calibrated for the grating and CCD spectral efficiency using a standard black body source. Photoluminescence lifetimes were measured using a GaAs PMT with a Multichannel Scaler (MCS). The time resolution of the lifetime measurement system was about 100 nsec.

3.4 Photoluminescence of Ge nanocrystals.

Figure 3.2 shows a set of Photoluminescence spectra for the four annealing temperatures of the middle dose Ge implanted samples for which TEM characterization was described in Chapter 2. Although the nanocrystal size increased monotonically with

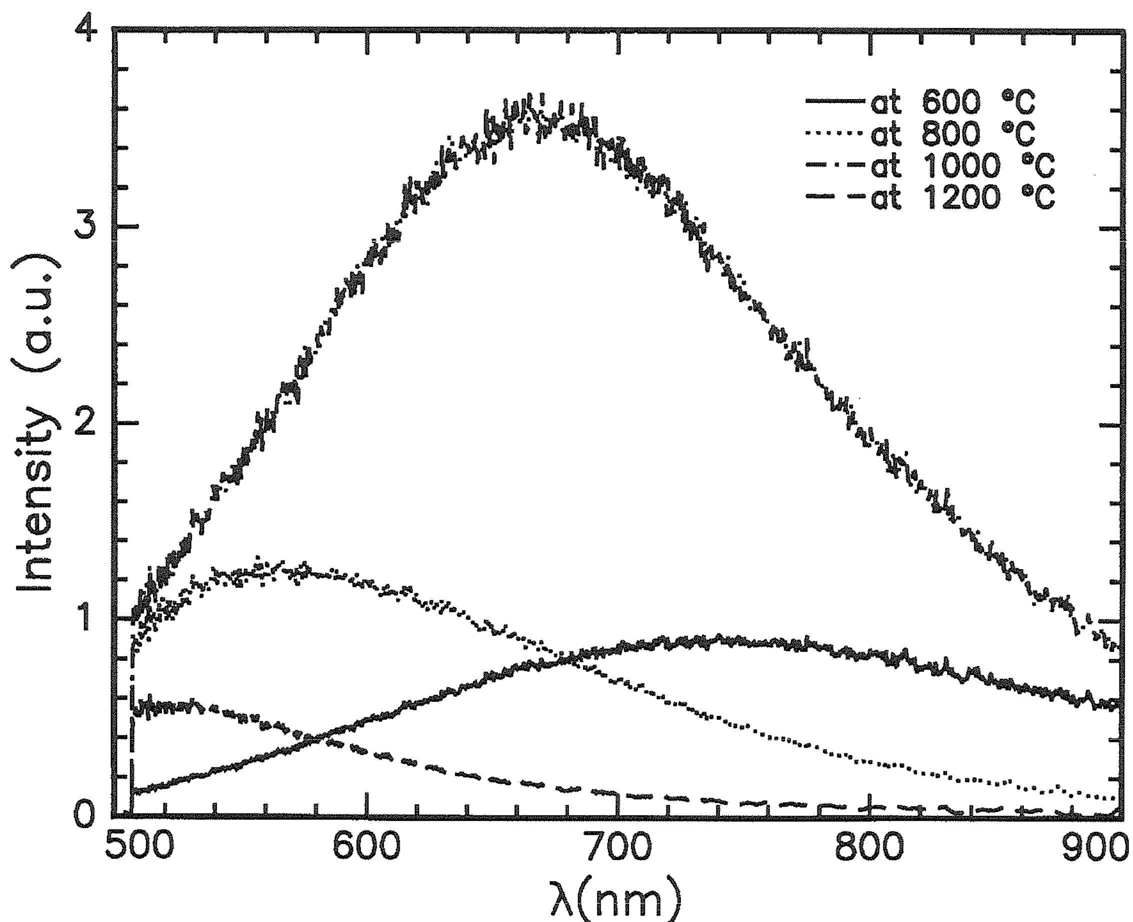

Figure 3.2 PL spectra of the middle dose Ge-implanted sample annealed at different temperatures.

increasing annealing temperature as was seen from bright-field TEM, there is no monotonic trend in the photoluminescence spectra. To compare these spectra to theoretical predictions of reference [16] we employ a simple "two-band" model.

3.5 Modeling of Ge PL spectra.

We consider an inhomogeneous ensemble of nanocrystal diameters given by the gaussian fits to the particle size distributions described in Chapter 2 and shown in figure 2.8. Under weak pump, we may assume that each nanocrystal has at most one excited

electron-hole pair. We thus treat the excited nanocrystals as being in the "upper" band and unexcited as being in the "lower" band. We solve the rate equation and for a steady-state condition. The radiative rates, the bandgap and the absorption efficiency are parametrized as functions of nanocrystal size. We take the complex part of the Ge bulk refractive index red-shifted by the predicted bandgap shift from reference [16] and scaled by the particle volume as the absorption efficiency. Nonradiative rates are not known and cannot be measured directly, so we will look at limiting cases. We can, however, assume a simple dependence for the nonradiative rate, that it is proportional to the nanocrystal surface area, since we expect dangling bonds and defects on the nanocrystal surface to act as nonradiative recombination centers. The model is briefly summarized below

R: Nanocrystal radius

I_p: Pump intensity

$Y_r(R), Y_n(R)$: Radiative and non-radiative decay rates, respectively.

$F(R)$: Fraction of nanocrystals excited.

$A(R)$: Absorption efficiency at pump wavelength

$N(R)$: Number of particles of radius R

Two-level system:

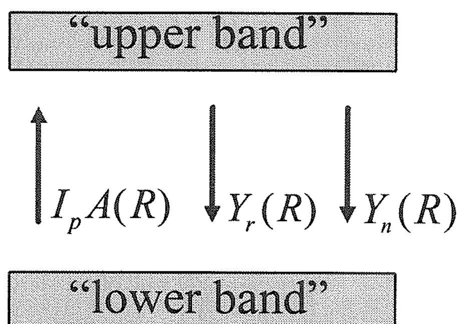

Steady state:

$$\left[Y_r(R) + Y_n(R)\right]F(R)N(R) = \left[1 - F(R)\right]N(R)I_pA(R)$$

$$I_{lum} = F(R)Y_r(R)N(R) = \frac{I_pA(R)N(R)Y_r(R)}{I_pA(R) + Y_r(R) + Y_n(R)}$$

$$\mathrm{A}(\mathrm{R}(\lambda)) = \mathrm{V_{nc}}(\mathrm{R}(\lambda))\mathrm{k}\left(2.71\mathrm{eV} + \mathrm{E_{gap}} - \frac{1239.842\,\mathrm{eV/nm}}{\lambda(\mathrm{nm})}\right)$$

We use this simple model to compare measured spectra to the effective mass model of reference [16]. Figure 3.3 shows again experimentally measure luminescence from the four samples for which particle size distributions were counted and three sets of predicted spectra corresponding to different assumptions on the relative magnitudes of rates. Figure 3.3 (b) is a predicted set of spectra assuming that $Y_r >> Y_n$, 3.3 (c) - a set of spectra assuming $Y_r >> Y_n$, and (d) - all rates roughly the same order of magnitude; This set of parameters comes closest to reproducing the experimental data. We conclude that no set of assumptions can give a satisfactory fit to the experimental data, and thus either the theoretical picture is at fault, or the origin of the luminescence is not exactly radiative recombination of excitons quantum confined at Ge nanocrystals. Subsequent work in our group shed more light on the origins of luminescence in our samples.

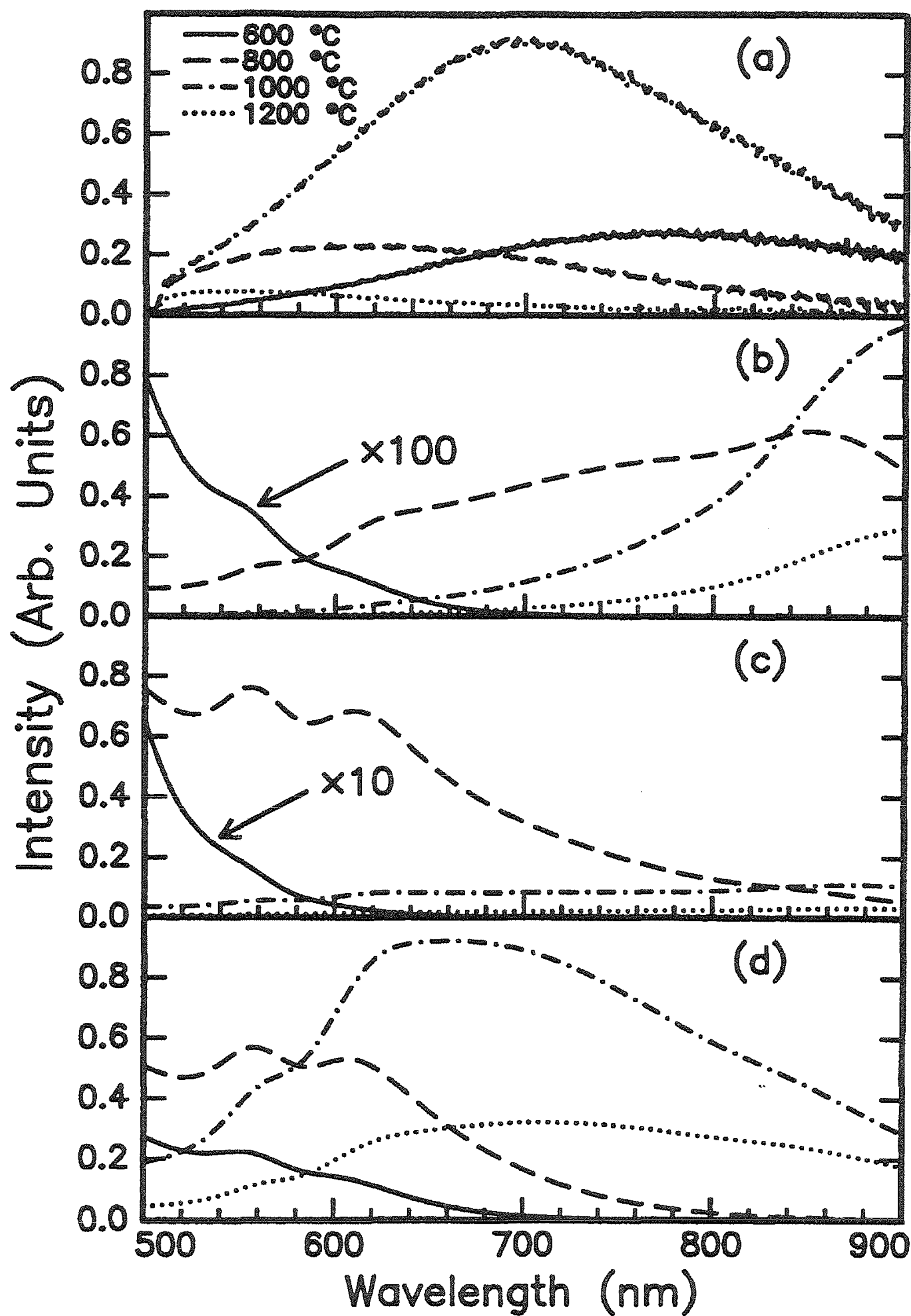

Figure 3.3 Comparison of measured and calculated PL spectra.

3.6 Deuteration experiments and Xe^+ implantation.

There is a number of possible sources of PL observed in our experiments. One is , as was mentioned above, excitonic recombination at Ge nanocrystals. Other mechanisms are possible: Surface-mediated recombination, recombination at defects inside the nanocrystals, and also luminescence of defects in the matrix created by ion implantation which survived after the thermal anneal. It is desirable to first examine the last possibility, as the least favorable to possible technological applications of the material. To do this a set of experiments was performed attempting to passivate defects in the matrix, and also nonradiative recombination centers at nanocrystals surfaces using deuterium since it is well known that hydrogen (and deuterium) passivates dangling bonds in bulk Si. We would thus expect luminescence from defects to decrease upon deuteration, and the luminescence from nanocrystals to be enhanced considerably due to blocking if nonradiative recombination channels.

In addition, thermal oxide films were implanted with Xe at doses that correspond to a similar defect density that would be produced as a result of Ge implants. These films were annealed under similar conditions and their luminescence was compared to that of the Ge-implanted films.

3.7 Experimental procedure.

Deuterium was implanted at 600 eV at various doses into the 2×10^{16} /cm^2 Ge implanted sample annealed at 1000 °C, which corresponded to the most intense luminescence. Deuterium concentrations in the film were measured by elastic recoil spectroscopy (ERS) using a 2 MeV $^4He^{++}$ beam.

Xe was implanted into 100 nm thick thermal oxide at 120 keV at three doses 6.6×10^{15} /cm^2, 1.3×10^{16} /cm^2, 3.3×10^{16} /cm^2. The energy and the doses were chosen to reproduce the defect density and spatial distribution created by Ge implants, as predicted by TRIM Monte Carlo code [23].

3.8 Experimental results.

Figure 3.4 shows the relative luminescence intensity of the sample upon deuteration to various deuterium doses. The luminescence decreases monotonically upon deuteration to almost zero. Subsequent annealing of the deuterated sample in vacuum at 500 °C leads to some recovery of the original PL due to out-diffusion of deuterium. After annealing about 70 % of deuterium has diffused out as seen from ERS data, leading to recovery of about 60% of the original PL intensity. Comparing PL spectra of Ge implanted samples with those of Xe implanted samples (Figure 3.5) where the luminescence is due solely to the damage in the matrix, we observe strikingly similar spectral features, and we are forced to conclude that Ge nanocrystals are optically "dead", and the observed PL is solely due to defects in SiO_2 created during implantation. PL lifetime measurements which put the lifetime at below 100 nanoseconds, the experimental resolution of our setup, also support this conclusion. Predicted radiative lifetimes range from milliseconds to microseconds, and reported values for porous silicon, for instance, are also in the msec- μsec range.

Later results indicate that there may be an extremely weak PL band around 850 nm which is left after extensive deuteration and which could be attributed to Ge nanocrystals, but since it is so inefficient, it would be of little practical value.

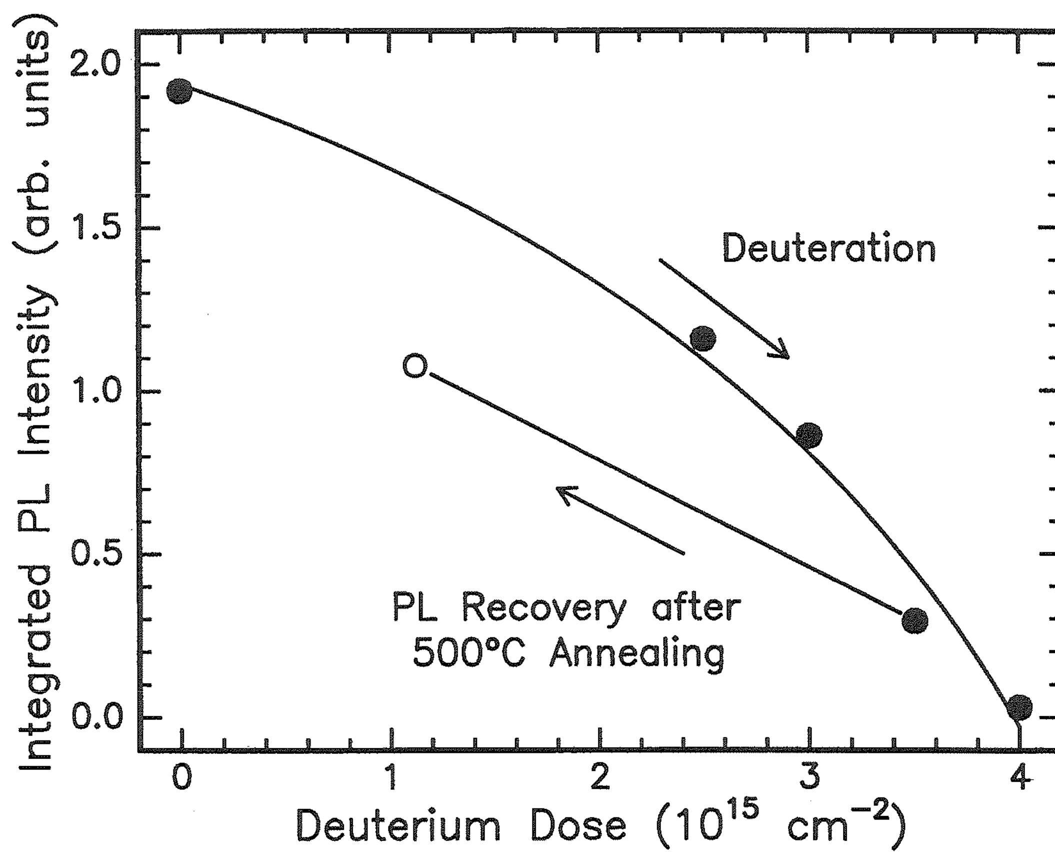

Figure 3.4 Effect of deuterium on the Ge nanocrystal sample PL intensity.

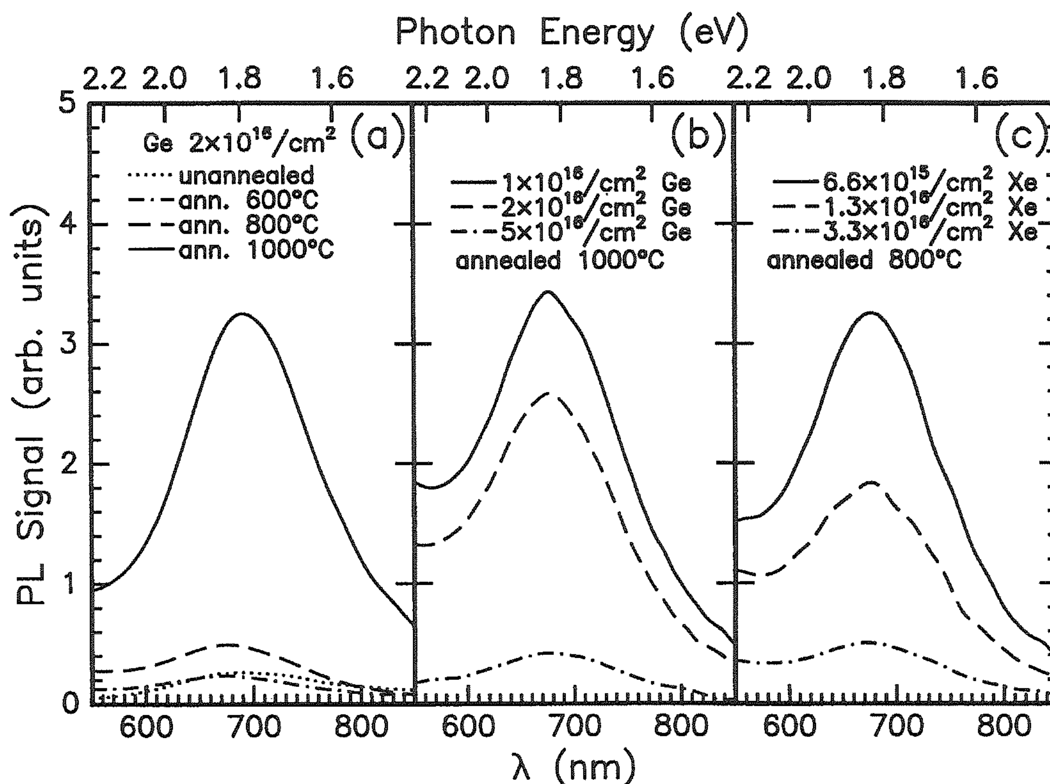

Figure 3.5 Comparison of Ge-implanted and Xe-implanted samples. (a) PL of Ge-implanted samples annealed at different temperatures, (b) PL of samples implanted with Ge at different doses and annealed at 1000 °C and (c) PL of samples implanted with Xe at different doses and annealed at 800 °C.

3.9 Predictions for Si nanocrystals.

Many more calculations have treated the bandgap of Si nanocrystals as a function of particle size [16-22]. A summary of selected predictions is given in Fig. 3.6. As for Ge nanocrystals, the qualitative trend is for the bandgap to increase significantly as the nanocrystal diameter decreases, albeit at smaller diameters than Ge nanocrystals. As for Ge nanocrystals, there is a large variation in the quantitative predictions, however most calculations agree that a noticeable change in the bandgap should happen for nanocrystal diameters below 4-5 nm.

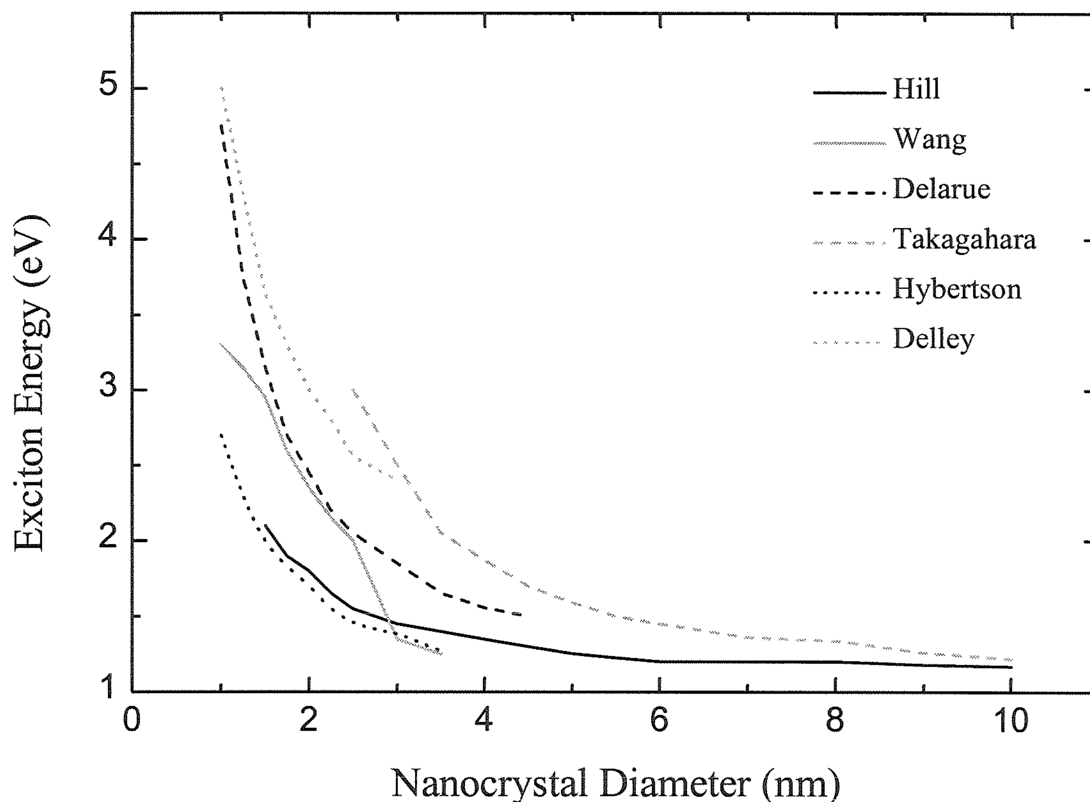

Figure 3.6 Summary of various calculations for Si nanocrystal bandgap as a function of nanocrystal diameter. Results are taken from references [16-22]

3.10 PL of Si nanocrystals.

Si-implanted samples treated in a similar fashion show a markedly different PL behavior. Figure 3.7 (a) shows the PL spectra of the Si nanocrystal sample. The yellow-red PL band around 500-600 nm, which we have found to be due to defects, is suppressed by deuteration, while a near IR band around 800 nm is unaffected. Subsequent low temperature annealing at 400 °C which promotes deuterium diffusion significantly

enhances the PL intensity of the 800 nm band. Selected spectrally resolved lifetimes shown for the 600 nm band and 800 nm band also indicate that the former is due to defect luminescence and the latter to Si nanocrystals. We thus conclude that the 800 nm band is due to Si nanocrystals, and deuterium enhances the intensity by passivating defects at the nanocrystal surface which may act as nonradiative recombination sites.

Figure 3.7 (b) shows a monotonic peak shift for the high dose Si-implanted sample annealed ad different temperatures. The peak red-shifts as the annealing temperature is increased which is consistent with the quantum confined exciton picture. Presumably higher annealing temperatures produce larger average particle diameters which corresponds, according to calculations, to lower emission photon energy. Although, as was indicated in the previous chapter, because of poor contrast in the TEM images, good size distributions could not be obtained and thus spectra for comparison could not be generated using bandgap data in literature, size distributions were generated from PL spectra for a 6×10^{16} /cm^2 Si-implanted sample annealed at 1100 °C during film etch-back using HF. Figure 3.8 shows a set of PL spectra after different durations of etching time. Figure 3.9 shows calculated nanocrystal size distributions for $Y_r >> Y_n$ and $Y_r << Y_n$. As expected, we need to look for nanocrystals in the 1-3 nm size range.

3.11 Conclusions.

Photoluminescence spectra of Ge nanocrystal containing samples were measured and compared to calculated spectra derived from bandgap and radiative rate predictions of reference [16]. No set of reasonable assumptions could be identified that produced quantitative agreement between calculated and measured spectra. Subsequent deuterium passivation experiments indicated that luminescence in these samples is due to defects in the matrix produced by ion implantation since deuterium quenched the sample luminescence. Photoluminescence lifetimes below 100 nsec. were also consistent with the defect origin of PL in these samples

On the other hand, the 800 nm photoluminescence band in Si nanocrystal containing samples was enhanced by deuteration, and so it appears to be due to Si

nanocrystallites. PL lifetimes in the μsec to msec range also suggest that PL was due to quantum-confined excitons. The model described earlier was used to generate a set of predicted particle size distributions. The resulting nanocrystal diameters were in the 1-3 nm range.

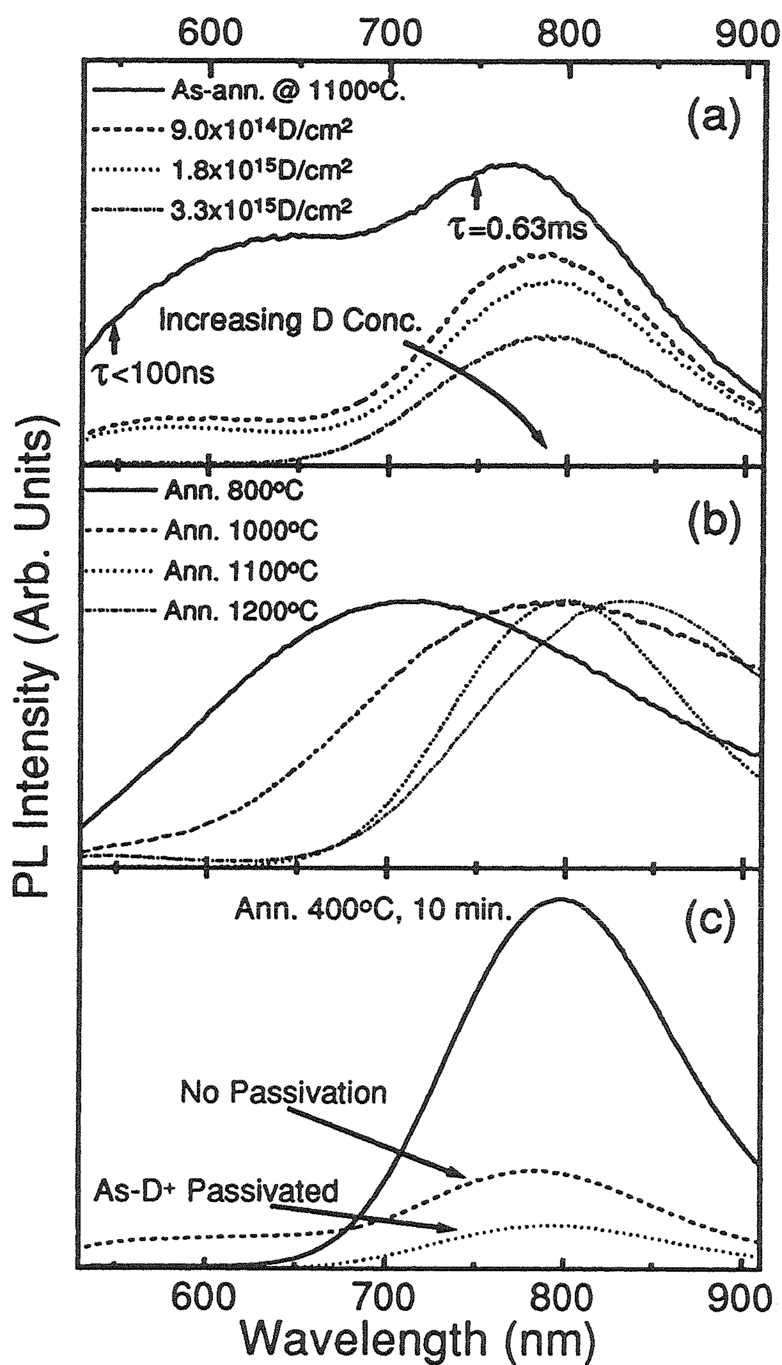

Figure 3.7 (a) Effect of deuteration on luminescence of Si nanocrystal sample. (b) PL peak shift as a function of annealing temperature. (c) Enhanced PL upon post-deuteration low temperature annealing.

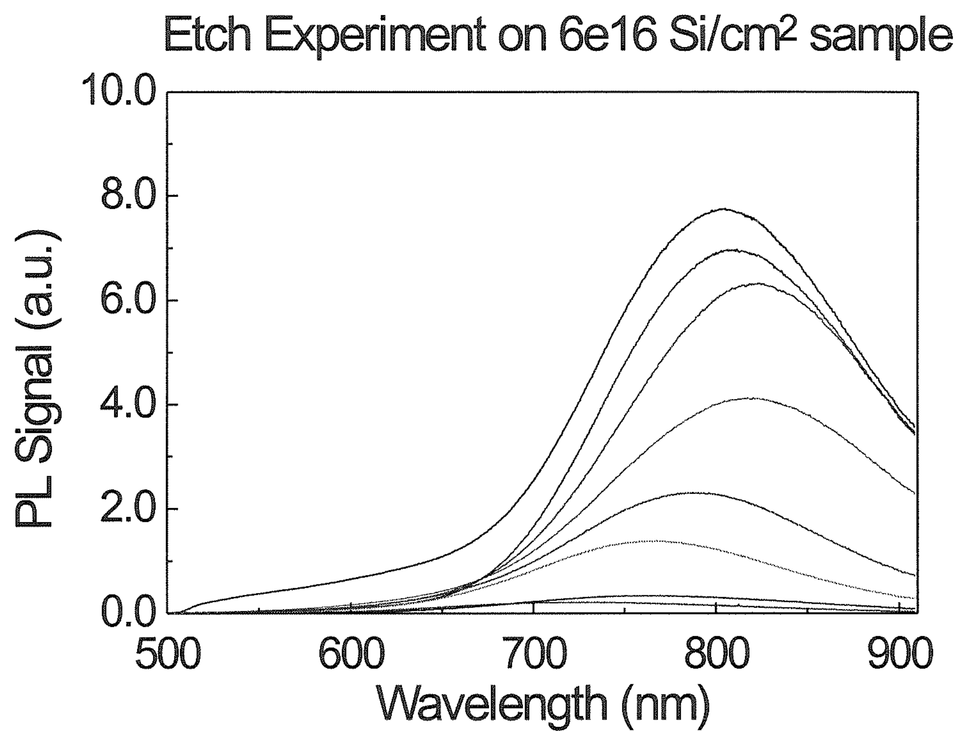

Figure 3.8 PL of etched-back Si-implanted sample. PL intensity decreases monotonically with increasing etching time.

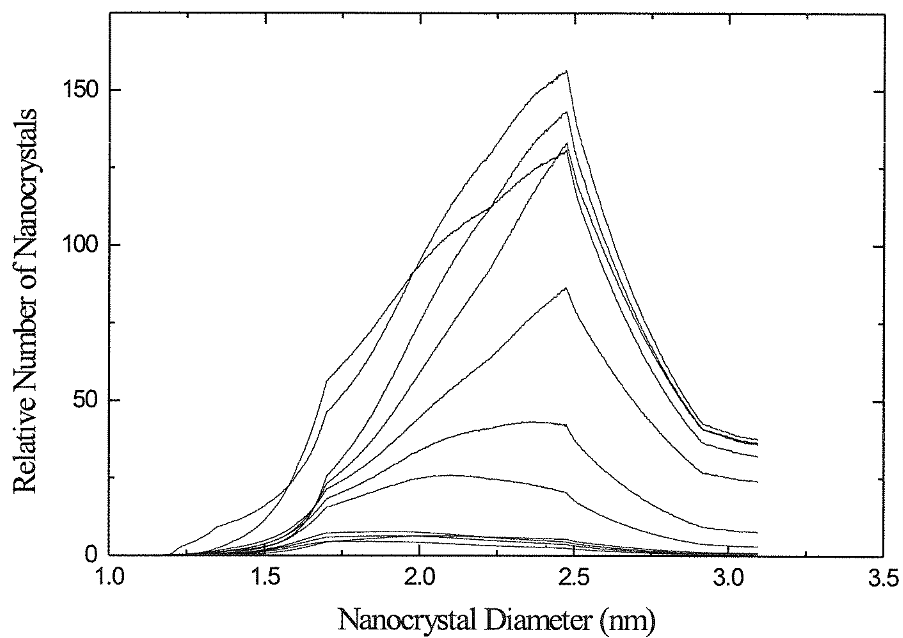

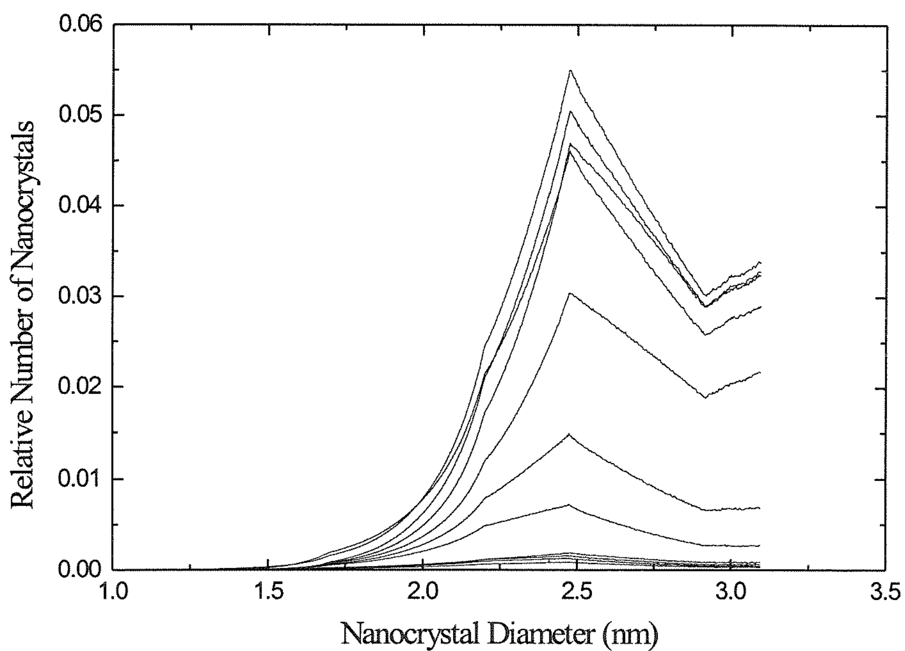

Figure 3.9 Nanocrystal size distributions calculated using the model and bandgap data from reference [21], assuming the radiative rate dominates (top) and non-radiative rate dominates (bottom).

References.

[1] S. Hayashi, M. Fujii, and K. Yamamoto, Jpn. J. Appl. Phys. **28**, p.1464 (1989).

[2] W. L. Wilson, P. F. Szajowski, and L. E. Brus, Science **262**, p.1242 (1993).

[3] Y. Maeda, N. Tsukamoto, Y. Yazawa, Y. Kanemitsu, and Y. Masumoto, Appl. Phys. Lett. **59**, p. 3168 (1991).

[4] S. Hayashi, Y. Kanzawa, M. Kataoka, T Nagareda, and K. Yamamoto, ISSPIC-6, (1992).

[5] Y. Kanemitsu, K. Suzuki, H. Uto, Y. Masumoto, T. Matsumoto, S. Kyushin, K. Higuchi, and H. Matsumoto, Appl. Phys. Lett. **61**, p. 2446 (1992).

[6] Z. H. Lu, D. J. Lockwood, and J.-M. Baribeau, Nature **378**, p.258 (1995).

[7] W. A. Saunders, K. J. Vahala, H. A. Atwater, and R. C. Flagan, J. Appl. Phys. **72**, p. 806 (1992).

[8] S. Hayashi, T. Nagareda, Y. Kanzawa, and K. Yamamoto, Jpn. J. Appl. Phys. **32**, p.3840 (1993).

[9] D. A. Grutzmacher, E. F. Steidmeier, H. Auderset, R. Morf, B. Delley, and R. Wessicken, Mat. Res. Soc. Symp. Proc. **358** (1994).

[10] T. Shimizu-Iwayama, M. Ohshima, T. Niimi, S. Nakao, K. Saitoh, T. Fujita, and N. Itoh, J. Phys. Cond. Matt 5, p.L377 (1993).

[11] A. K. Dutta, Appl. Phys. Lett. **68**, p.1189 (1996).

[12] Y. Kanemitsu, Phys. Rev. B **53**, p.13515 (1996).

[13] J. B. Khurgin, W. E. Forsythe, G. S. Tompa, and B. A. Khan, Appl. Phys. Lett. **69**, p. 1241 (1996).

[14] T. Shimizu-Iwayama, K. Fujita, M. Akai, S. Nakao, K. Saitoh, J. NonCrystalline Solids **187**, p. 112 (1995).

[15] N. A. Hill, Private Communication (1994).

[16] T. Takagahara and K. Takeda, Phys. Rev. B **46**, p. 15578 (1992).

[17] N. A. Hill and K.B. Whaley, Phys. Rev. Lett. **75**, p.1130 (1995).

[18] K. Takeda, J. Phys. Soc. Jpn **63** , Suppl. B. pp 1-29 (1994).

[19] B. Delley and E. F. Steigmeier, Phys Rev. B. **47**, p. 1397 (1993).

[20] F. Huaxiang, Y. Ling, and X. Xide, J. Phys. Cond. Matt. **5**, p.1222 (1993).

[21] M.S. Hybertsen, Phys. Rev. Lett. 72, p.1514 (1994).

[22] J. P. Proot, C. Delerue, and G. Allan, Appl. Phys. Lett. **61**, p.1948 (1992).

[23] J.F. Ziegler, J.P. Biersack, and U. Littmark, *The Stopping and Range of Ions in Solids*, Pergamon, New York, (1985).

Chapter 4
Nanocrystal-based devices

4.1 Introduction.

Strong photoluminescence of nanocrystal-containing oxide does not necessarily guarantee that it will be technologically useful, since almost all devices must be electrically pumped. To test the possibility of making electroluminescent devices based on nanocrystals PIN structures have been fabricated and characterized. The structure consists of a nanocrystal-containing SiO_2 sandwiched between two layers of Si, one p- and one n-doped. Electroluminescence spectra and current-voltage (I-V) characteristics were acquired for these devices.

4.2 Fabrication of Ge nanocrystal-containing LED structure.

Samples consisted of a 45 nm thick polycrystalline Si films deposited initially as amorphous films by ultrahigh vacuum electron beam evaporation onto 70 nm thick SiO_2 films thermally grown on n^+ Si substrates. These structures were implanted with Ge at doses of 4×10^{16} /cm^2 at 140 keV and 1×10^{16} /cm^2 at both 130 and 150 keV. These energies and doses were chosen to create a supersaturated solid solution of Ge in the SiO_2 film with approximately uniform Ge concentration profile at 5 atomic % throughout the layer. The samples were subsequently annealed at 600 °C in high vacuum (~1×10^{-6} Torr) to induce precipitation, then the top layer was doped with B in a furnace at 900 °C for 15 min. to generate a p^+ polycrystalline Si film at the top of the structure. Other experiments [1] suggest that Ge nanocrystals continued to grow during this 900 °C anneal. Finally, photolithography was used to define isolated mesas for separate devices, and to define Al contacts using liftoff. Individual devices were of various sizes, between 1 and 0.05 mm^2.

4.3 Experimental Procedure.

The fabricated devices were subsequently electrically characterized with a semiconductor parameter analyzer operating in current-voltage test mode. Electroluminescence was measured with a single grating spectrometer equipped with a charge-coupled-device-based optical multichannel analyzer detector. Photoluminescence spectra were measured with the same spectrometer and were pumped with 40 mW of 457.9 nm argon-ion laser line. System response of the spectrometer was calibrated using a black-body source and all luminescence spectra are divided by the system response curve.

TEM images were acquired using the Phillips 301 transmission electron microscope.

4.4 Structural characterization.

Figure 4.1(a) is a bright-field cross-sectional TEM micrograph of the completed device prior to metal contact deposition. Visible at the top is the polycrystalline silicon layer with grain size approximately equal to the film thickness. The top surface of the polycrystalline silicon is very smooth, which is characteristic of films deposited in the amorphous phase and crystallize during post-deposition anneal. The interface roughness of ~5 nm is observed at the polycrystalline Si/oxide interface, and the thickness of the oxide appears to vary by approximately 5 nm across the field of view of the cross-sectional specimen. Rutherford Backscattering spectroscopy measurements suggest that the oxide is of a stoicheometry SiO_x, where $1.5 \leq x \leq 1.8$. The speckles observable in bright-field

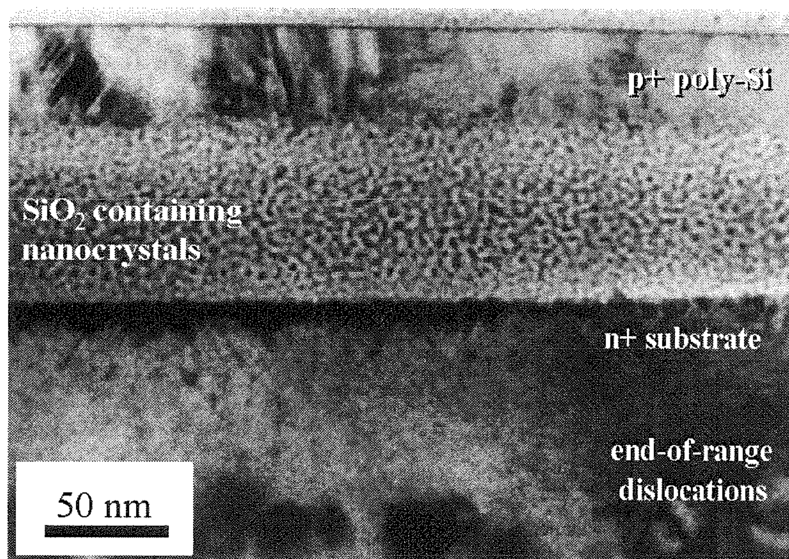

(a)

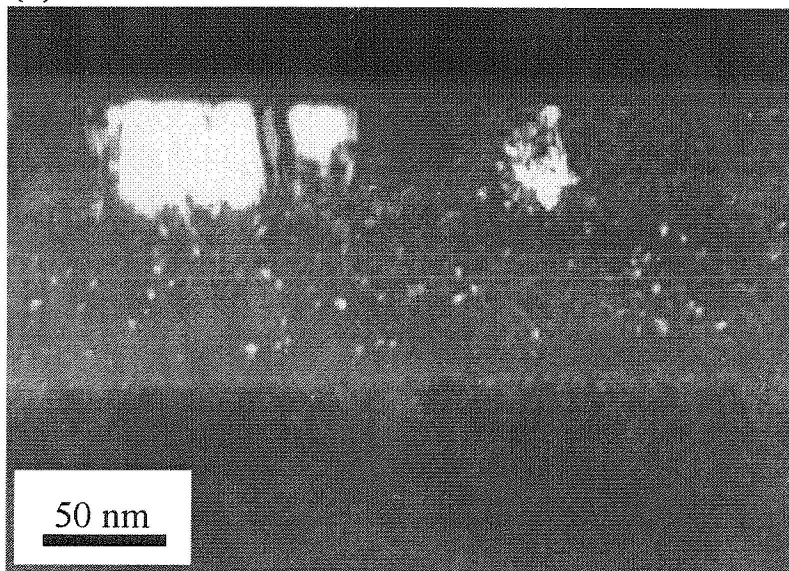

(b)

Figure 4.1 (a) Bright field cross-sectional electron micrograph og the completed device prior to metal contact deposition. (b) Dark field cross-sectional electron micrograph of the same region.

contrast correspond to Ge nanocrystals roughly 5 nm in diameter, which are visible in the accompanying dark-field image of the same region shown in Fig. 4.1 (b). The volume density of nanocrystals is approximately 1×10^{18} /cm^3. Also visible is a rough, dark layer at the lower oxide/Si interface, which is probably Ge_xSi_{1-x} alloy region which resulted from extension of the implanted Ge profile at 150 keV in the Si substrate and from diffusion of Ge out of the oxide and into the substrate during annealing. This later effect has been observed in other work at our group by RBS [2]. This effect is apparent in these micrographs as a roughly 10 nm wide bands of oxide near the two interfaces which are devoid of nanocrystals. A band of extended defects appears approximately 100 nm below the oxide/substrate interface, which is due to condensation of Si point defects generated from the stopping of the tail of Ge implant profile in the Si substrate.

4.5 Electrical and optical characterization.

The I-V characteristic of a typical device (0.8 mm^2) is shown in Fig. 4.2. Rectifying behavior is seen in forward bias, and a relatively broad breakdown feature is seen in reverse bias between -5 and -10 volts. In both forward and reverse bias, a relatively large series resistance is observed. Electroluminescence is characterized by an onset at reverse bias below approximately -10 V, which corresponds to an electric field greater than about 10^6 V/cm. There are indications that there exists a polarity dependence of the breakdown in ultra-thin SiO_2 films related to the energy of hot electrons relative to the Fermi level at the anode/oxide interface [3]. The dielectric breakdown electric field of thin films of high-quality, stoicheometric SiO_2 is on the order of 10^7 V/cm, but the observed field is reasonable in view of the stoicheometry and modified structure of the oxide layer.

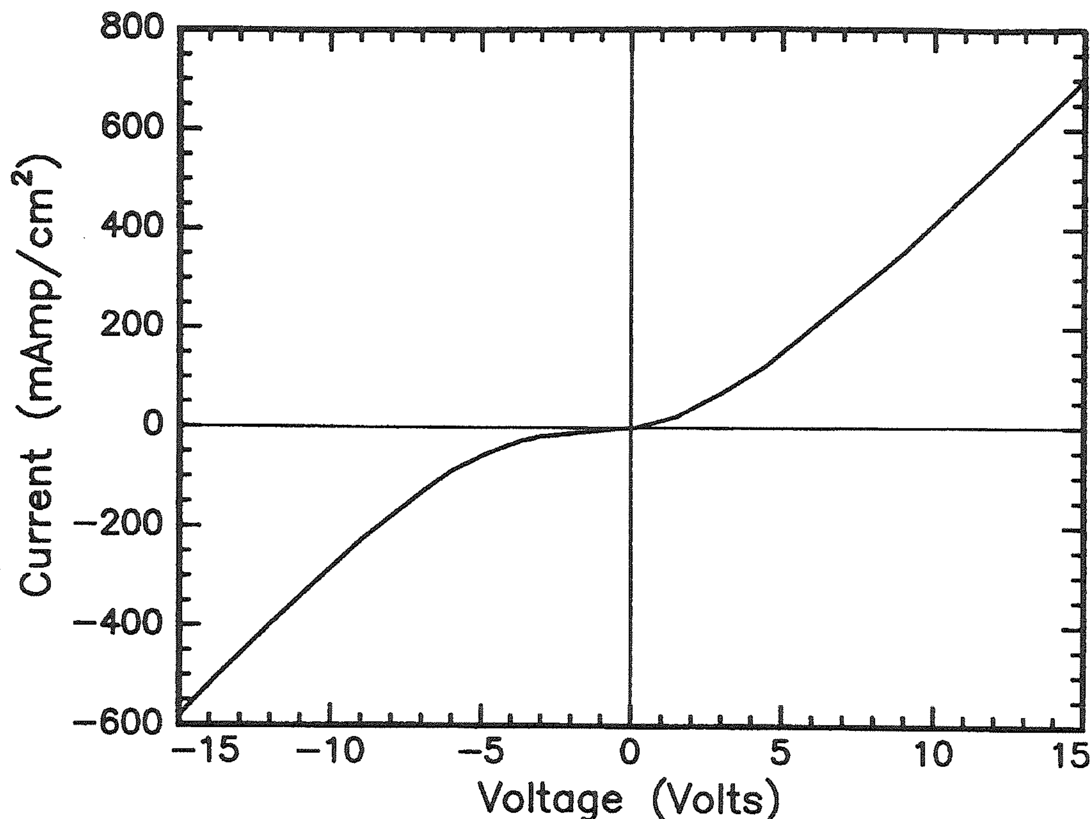

Figure 4.2 The current-voltage characteristic of a typical device.

Devices fabricated without Ge ion implantation did not exhibit any breakdown at ±50 V, which is the maximum voltage range of the parameter analyzer. The strongest luminescence usually appeared over approximately 10 % of the device surface. Spatial non-uniformity in emission may be related to nonuniformity in oxide layer thickness, which would lead to the development of electric fields exceeding the breakdown field in the thinnest oxide regions first. Some of the devices did not exhibit luminescence and their I-V characteristic appeared to be that of a diode in series with a large resistance (> 1000 Ω).

The spectra of the devices that did exhibit electroluminescence looked quite similar and were very broad with an onset at about 500 nm. Figure 4.3 is a comparison of photoluminescence and electroluminescence spectra. The sharp feature at approximately

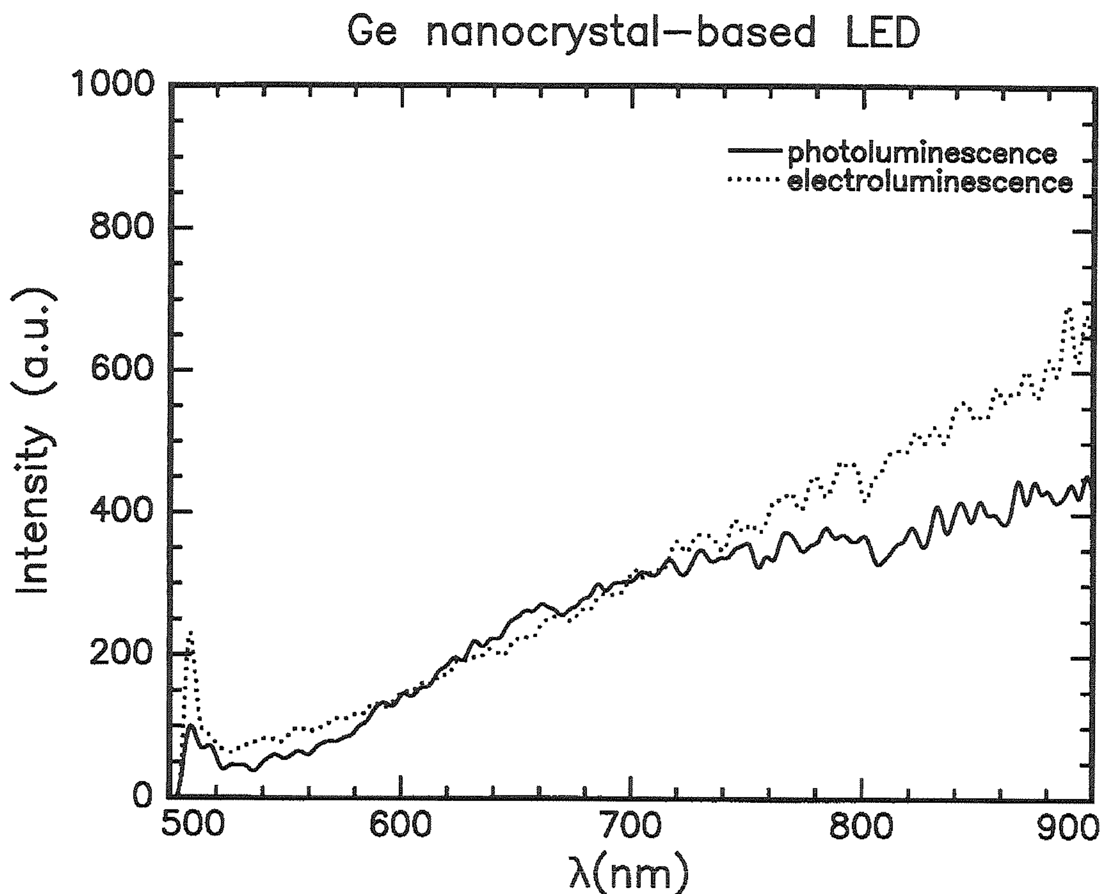

Figure 4.3 Photoluminescence and Electroluminescence spectra at room temperature for a typical device operating in reverse breakdown. Spectra are corrected for the response of the optical spectrometer. The sharp feature at approximately 510 nm is an artifact of normalization by the spectrometer response function.

510 nm is an artifact generated by division by the system response function, and was related to an abrupt change in transmission of a filter used to suppress the pump beam. We note that there are no artifacts in the spectra above 520 nm, where the filter transmission is constant and near unity. The external efficiency of the electroluminescence was difficult to measure directly with our setup due to difficulty of measuring total absolute optical power output, but can be estimated to be about 10^{-6}.

Differences between EL and PL spectra could have many causes. Possible factors include differences in capture cross sections for the pump hot electrons and photons in EL and PL respectively. Many details regarding the mechanism responsible for EL can not be deduced from the available data, however we note that previously investigated EL in Si containing SiO_2 materials with broadly similar morphology yielded similar results [4]. Those authors proposed a mechanism based on radiative electronic transitions between discrete energy levels associated with Si islands and/or their interfaces with the host matrix. It is possible that carrier injection into these discrete energy states occurs via either relaxation from extended states in the conduction band or by tunneling from other localized states. We speculate that the mechanism for excitation of EL is related to impact ionization by "hot" carriers in the oxide layer, because EL was observed when the device was in the reverse bias breakdown regime, and no EL was observed in forward bias. We note that carrier-related EL is known to occur in reverse breakdown in single-crystal silicon [5], but at much lower efficiencies than reported here.

It is also important to note that emission via black-body radiation is most likely insignificant, since visible emission would require local sample temperatures above 800 °C, temperatures employed in anneals used to precipitate and grow nanocrystals, which would result in significant microstructural and optical changes in devices during operation. However, no degradation of EL intensity was observed over 6 hours of device operation. Moreover, electrical and optical pump powers were similar (0.5 - 5.0 W/cm^2) and were unlikely to result in enough heating to produce visible blackbody emission from the devices, which were in intimate thermal contact with a 4 cm^2 area, 0.4 mm thick Si substrate.

4.6 Fabrication of Si nanocrystal-based LED.

A similar structure was fabricated containing Si nanocrystals instead of the Ge nanocrystals. Samples of 1 μm thermal SiO_2 on p-doped Si substrates were implanted with Si at four different energies and doses, 7.0e16 /cm^2 at 75 keV, 1.3e17 /cm^2 at 180 keV, 2.0e17 /cm^2 at 320 keV, and 2.3e17 /cm^2 at 500 keV to produce a uniform Si

concentration profile throughout the oxide film. A 2000 Å thick poly-Si top contact was deposited by MBE and the sample was annealed at 1100 °C for 30 min to precipitate the nanocrystals. Subsequently photolithography was used to define individual device mesas which were subsequently etched out using a weak $HF:HNO_3$ solution. The individual device sizes ranged from 0.07 to 1 mm^2.

4.7 Experimental procedure.

Fabricated devices were subsequently electrically characterized with Keithley 487 picoammeter and voltage source Electroluminescence was measured with a single grating spectrometer equipped with a charge-coupled device-based optical multichannel analyzer detector. Photoluminescence spectra were measured with the same spectrometer and were pumped with 15 mW of 457.9 nm argon-ion laser line. System response of the spectrometer was calibrated using a black-body source and all luminescence spectra are divided by the system response curve. TEM images were acquired using the Phillips 301 Transmission electron microscope.

4.8 Structural characterization.

Figure 4.4 is a bright-field and dark-field cross-sectional TEM micrograph of a portion of the annealed oxide film. A number of Si nanocrystals are visible in both bright and dark field.

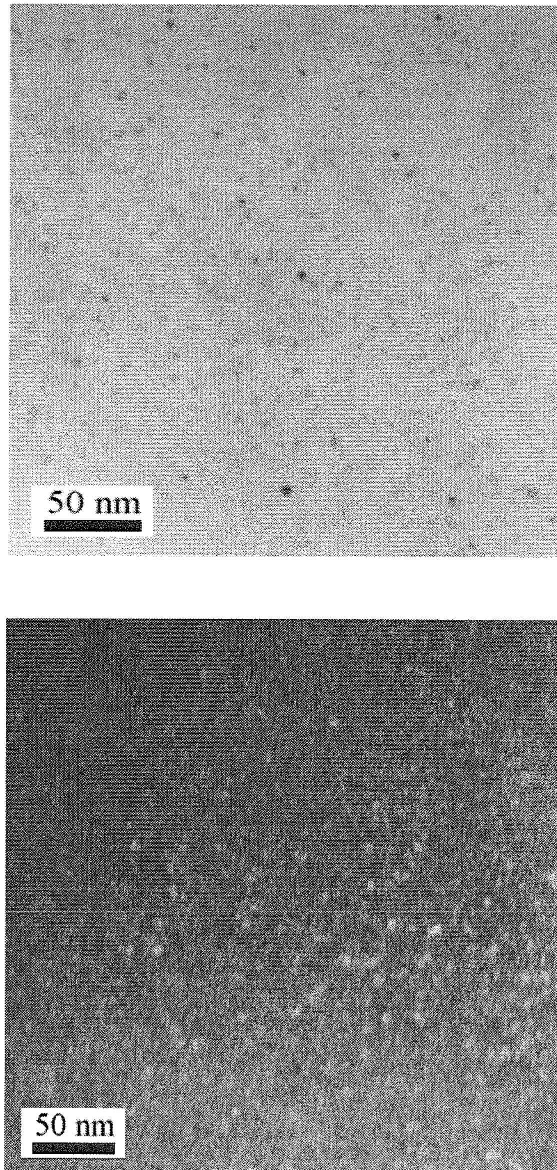

Figure 4.4 Bright and dark field images of Si nanocrystals in oxide in the device sample.

4.9 Electrical and optical characterization.

Figure 4.5 shows an I-V characteristic of a typical device. The curve shows a rectifying behavior with a rather large series resistance. The current shown in the plot represents the saturation current for a given applied voltage. It took a few seconds for the device to reach the saturation current for bias voltages over 10 V. Figure 4.6 shows a set of EL spectra taken at different applied voltages. Again, the spectra were taken at the saturation current of the device. A luminescence band with a peak at 800 nm characteristic of Si nanocrystal samples (chapter 3) appeared in reverse bias at voltages below -10 V. A similar EL band, although much broader, was observed in partially oxidized porous Si [13]. We note that the structure visible beyond 950 nm is an artifact of normalization since the system response at those wavelengths is very low. A PL spectrum of the device is shown for comparison in Fig. 4.7. The 800 nm band is clearly visible. At very high reverse bias voltages (below about -120 V) the intensity of the 800 nm band decreased and a strong band appeared centered around 900 nm. This effect often seemed to be accompanied by irreversible physical changes to the film. The EL efficiency of the device was 10^{-7} at -20 V bias and decreased by over an order of magnitude at -90 V bias. The highest efficiency observed for these devices was 5×10^{-7} at -8 V bias. While these numbers are two orders of magnitude below those reported for partially oxidized porous Si [13,16], we attribute the discrepancy to passivation issues. It is well known that only the (100) Si - oxide interface possesses a low density of interface states. Small nanocrystals are expected to possess significant effective contributions from other planes to the surface state density, and thus would not be well passivated. This is supported by deuterium passivation experiments, where PL was seen to increase by almost two orders of magnitude upon passivation with deuterium [10].

In forward bias there was a very weak luminescence with an unusual structure. The bias voltages at which EL was observed correspond to fields of 100 kV/cm for 10 V bias to 1.5 MV/cm for 150 V bias. Electronic transport in Si-rich SiO_2 films is fairly well understood thanks to a significant amount of investigation by DiMaria and others at IBM [4, 6-9]. They have found that for low fields (below 1 MV/cm), the transport proceeds

primarily by direct tunneling from nanocrystal to nanocrystal while at higher fields (a few MV/cm) the carriers are injected into the oxide conduction band by Fowler-Nordheim tunneling and are subsequently accelerated in the field loosing energy to phonon resonances and impact ionization. [4,11,12]. For fields below 1<V/cm the average electron energy is around 0 - i.e., there are no "hot" electrons [7,12]. Thus our EL spectra for 10-60 V bias probably correspond to transitions induced by tunneling of "cool" electrons into nanocrystals. We thus observe a characteristic emission at 800 nm which we have come to associate with the presence of Si nanocrystals in the SiO_2 matrix [10]. At fields above 1.2 MV/cm, we observe a irreversible degradation of the 800 nm band and a band around 900 nm begins to grow. At these fields we would expect some "hot" electrons to be present [12]. Thus the 900 nm band is most likely either excited by impact ionization of luminescent centers in the oxide, or by radiative trapping of "hot" electrons into nanocrystals. Figure 4.8 shows an EL spectrum taken in the forward breakdown regime at 300 V forward bias. The luminescence shifts significantly towards the Si bandedge.

It appears that the presence of hot electrons causes a degradation of the Si nanocrystal luminescence presumably by creating nonradiative defect states at or near Si nanocrystal interfaces. It is known that holes created by impact ionization recombining with injected electrons can lead to creation of interface states [14,15]. These, serving as nonradiative recombination sites, can lead to quenching of nanocrystal luminescence.

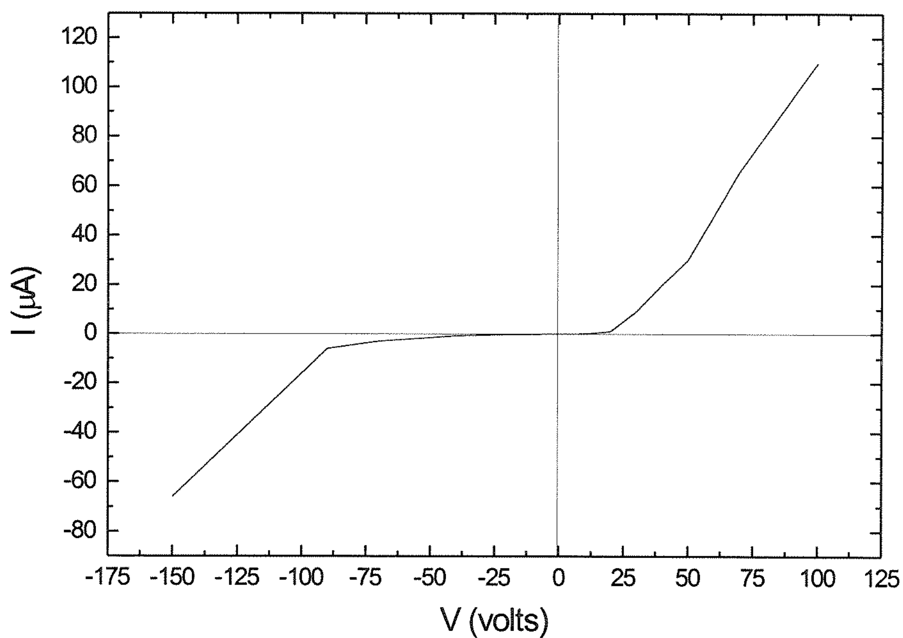

Figure 4.5 I-V characteristic of a typical device.

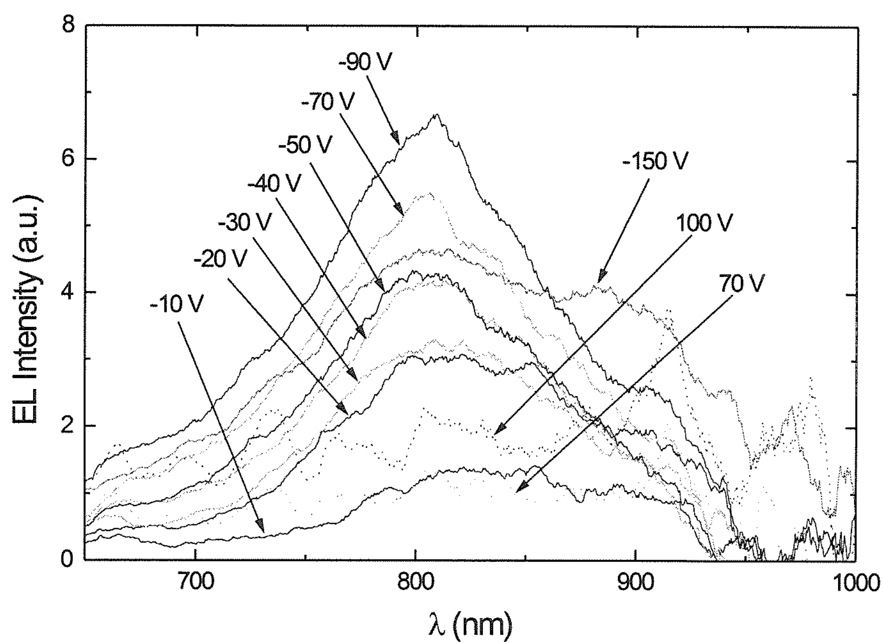

Figure 4.6 EL spectra of a typical device taken at different bias voltages.

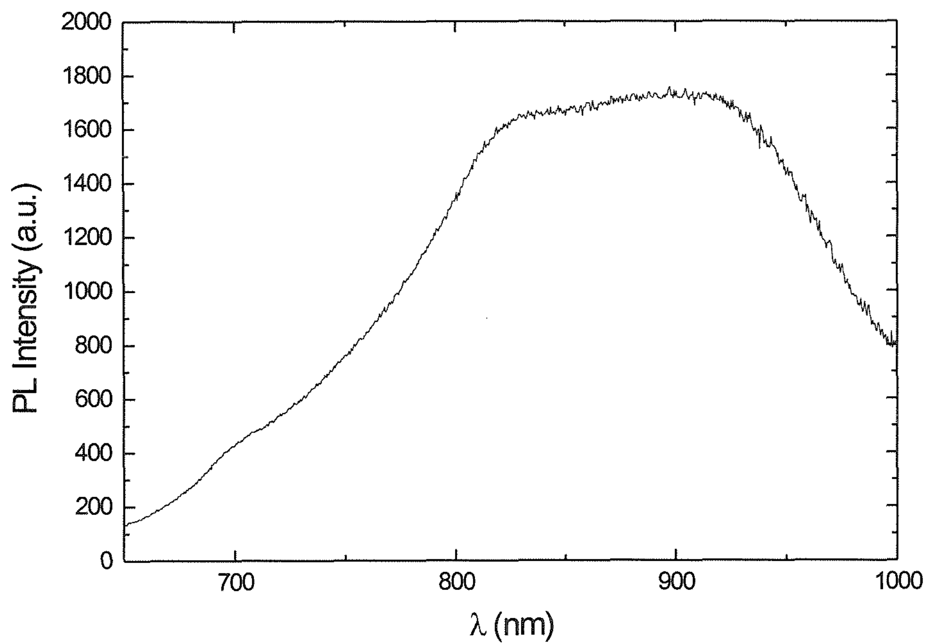

Figure 4.7 PL spectrum of the device. Differences in the excitation cross-sections for photons and electrons are most likely responsible for the discrepancy between PL and EL spectra.

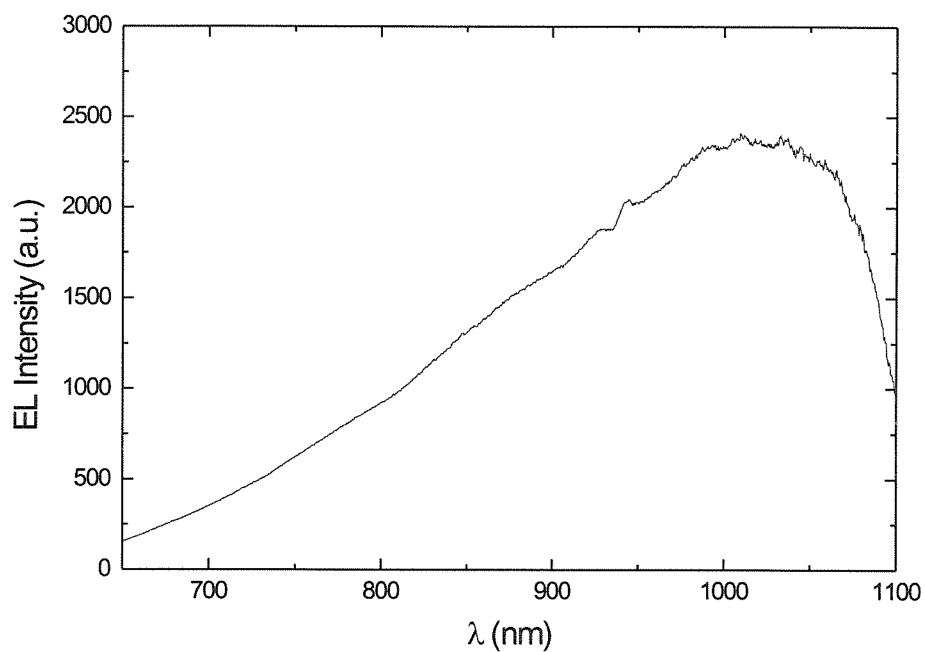

Figure 4.8 EL spectrum taken at 300 V forward bias.

4.10 Conclusions.

Electroluminescent PIN structures containing both Si and Ge nanocrystals were fabricated using ion implantation and precipitation by thermal annealing. These structures exhibited EL in reverse bias spectrally similar to observed PL. At moderate bias voltages Si containing structures electroluminesced with a characteristic 800 nm indicating that this luminescence is due to radiative recombination of electrically excited excitons quantum confined at Si nanocrystals. The origins of luminescence in Ge nanocrystal containing device are less clear since it was found that majority of the PL from Ge nanocrystal containing samples originates from defects in the matrix. Efficiencies of the devices were in the 10^{-6}-10^{-7} range, and are expected to improve substantially upon passivation of nanocrystals by hydrogen.

References.

[1] C. M. Yang, K. V. Shcheglov, K.J. Vahala, and H. A. Atwater, Nucl. Instr. Methods in Phys. Research B **106**, p. 433 (1995).

[2] C.M. Yang, Doctoral Dissertation, Caltech, (1996).

[3] D.J. DiMaria, Appl. Phys. Lett. **68**, p.3004 (1996).

[4] D.J. DiMaria, J.R. Kirtley, E. J. Pakulis, D.W. Dong, T.S. Kuan, F.L. Pesavento, T.N. Theis, J.A. Cutro, and S.D. Brorson, J. Appl. Phys. **56**, p.401 (1984).

[5] R. Newman, W.C. Dash, R.N. Hall, and W.E. Burch, Phys. Rev. A **98**, p.1536 (1955).

[6] D.J. DiMaria, T.N. Theis, J. R. Kirtley, F.L. Pesavento, D.W. Dong, and S.D. Brorson, J. Appl. Phys. **57**, p. 1214 (1985).

[7] D.J. DiMaria, M.V. Fischetti, M. Arienzo, and E. Tierney, J. Appl. Phys. **60**, p.1719 (1986).

[8] D.J. Robbins, D.J. DiMaria, C. Falcony, and D.W. Dong, J. Appl. Phys. **54**, p.4553 (1983).

[9] D.J. DiMaria, D. Arnold, and E. Cartier, Appl .Phys. Lett **60**, p. 2118 (1992).

[10] K.S. Min, K.V. Shcheglov, C.M. Yang, H.A. Atwater, M.L. Brongersma, and A. Polman, Appl. Phys. Lett. **69**, p.2033 (1996).

[11] D. Arnold, E. Cartier, and D.J. DiMaria, Phys. Rev. B **45**, p.1477 (1992).

[12] D. J. DiMaria, E. Cartier, and D. Arnold, J. Appl. Phys. **73**, p.3367 (1993).

[13] L Tsybeskov, S.P. Duttagupta, and P.M. Fauchet, Sol. St. Comm. **95**, p.429 (1995).

[14] J.H. Stathis and D.J. DiMaria, Appl. Phys. Lett. **61**, p.2887 (1992).

[15] S.K. Lai, J. Appl. Phys. **54**, p.2540 (1983).

[16] L. Tsybeskov, S.P. Duttagupta, K.D. Hirschman, and P.M. Fauchet, Appl. Phys. Lett. **68**, p. 2058 (1996).

Chapter 5

Nonlinear Optics of Nanocrystals

5.1 Introduction.

Semiconductor nanocrystals in a dielectric matrix have a potential to exhibit large optical nonlinearities. Since most of these materials are isotropic on the scale of the wavelength of light, symmetry demands that the second-order nonlinearity, $\chi^{(2)}$, be exactly zero. However, the third-order nonlinearity, $\chi^{(3)}$,can be substantially enhanced by the presence of nanocrystals. The large enhancement of the cubic nonlinearity is expected to take place because of local field corrections [1] and of the discreteness of the electronic density of states. The latter, provided that carrier lifetimes are sufficiently long, can lead to significant absorption saturation effects which through Kramers-Kronig relations will translate to intensity-dependent perturbations in the refractive index.

To date, the most thoroughly investigated $\chi^{(3)}$'s in a semiconductor nanocrystal material have been for II-VI nanocrystallites for which extremely precise control of nanocrystal size distributions is possible because of the synthesis technique, particularly for CdS [2] and CdSSe [3,4] nanocrystals in commercially available color glass filters. For these materials values up to 10^{-7} esu have been reported [2].

Fused silica containing metal nanoclusters such as Au, Cu and Pb, produced by ion implantation and thermal annealing, has received some attention as well [5,6]. For these materials, surface plasmon resonance enhancement has produced $\chi^{(3)}$'s as large as 10^{-10} esu.[6].

Nonlinear optical properties of some other nanoclusters in dielectric matrixes have been investigated as well. In particular a $\chi^{(3)}$ of 2.0×10^{-6} esu has been reported for CuCl nanoclusters [7] and of 1.2×10^{-6} esu for amorphous Phosphorus nanoclusters [8].

In light of theoretical predictions for Group IV semiconductor materials described in Chapter 3 [9-13], namely that the bandgap should become quasi-direct for small

enough crystallite sizes, Si and Ge nanocrystals in SiO_2 may be promising materials for nonlinear integrated optics applications. In the following sections measurements of the real part of the cubic optical nonlinearity $\chi^{(3)}$ are described.

5.2 Sample preparation.

Quartz and sapphire plates were implanted with Si an 2 MeV at 4×10^{17} /cm^2 and with Ge at 3 MeV and at 2×10^{17} /cm^2. Table 5.1 summarizes the average implant depths, implanted layer thickness, and peak atomic concentrations for the four samples. This data was obtained from TRIMM simulations [14].

Table 5.1 Summary of implantation characteristics.

Sample	Average implant depth (μm)	Implanted layer thickness (μm)	Peak atomic concentration (%)
Ge→Al_2O_3	1.25	0.2	3.4
Ge→SiO_2	2.2	0.3	4.5
Si→Al_2O_3	1.2	0.15	10
Si→SiO_2	2.1	0.2	12

Si -implanted samples were annealed in high vacuum at 1100 °C for 15 minutes and Ge-implanted samples - at 800 °C for 15 minutes to precipitate nanocrystals out of the supersaturated solid solution. The $\chi^{(3)}$ values of the resulting samples were characterized by z-scan measurement.

5.3 Experimental procedure.

Z-scan is a simple and effective way to characterize the cubic nonlinearity of thin films [15]. The principle of the method lies in the fact that a cubic nonlinearity can be though of as an intensity-dependent index perturbation. The schematic of a z-scan setup

is shown in Fig. 5.1. The sample being characterized is moved through the focus of the lens.

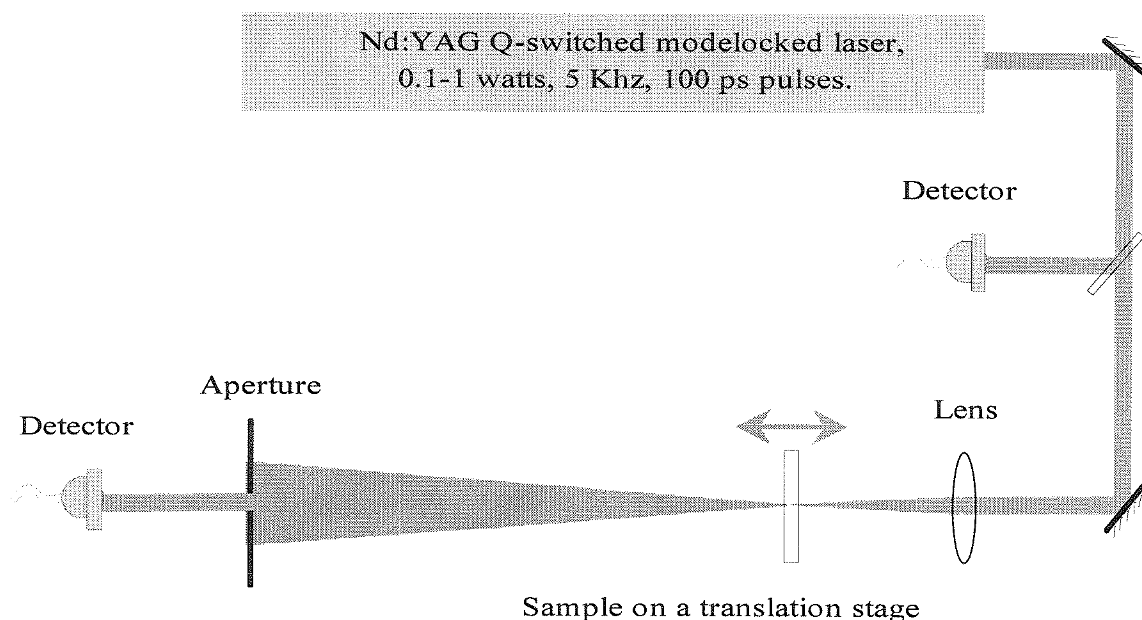

Figure 5.1 Schematic of the z-scan experimental setup.

The incident intensity changes depending on the sample position, and thus a weak variable lens proportional to the $\chi^{(3)}$ is induced in the sample. This lens causes a weak focusing or defocusing of the beam which can be detected as variations in intensity in the far field. This far-field intensity normalized by the incident laser power follows a characteristic curve as a sample is moved through focus (Fig. 5.2). The peak-to-valley difference $T_{p\text{-}v}$ is directly proportional to the intensity-dependent index perturbation, which in turn is proportional to the $\chi^{(3)}$.

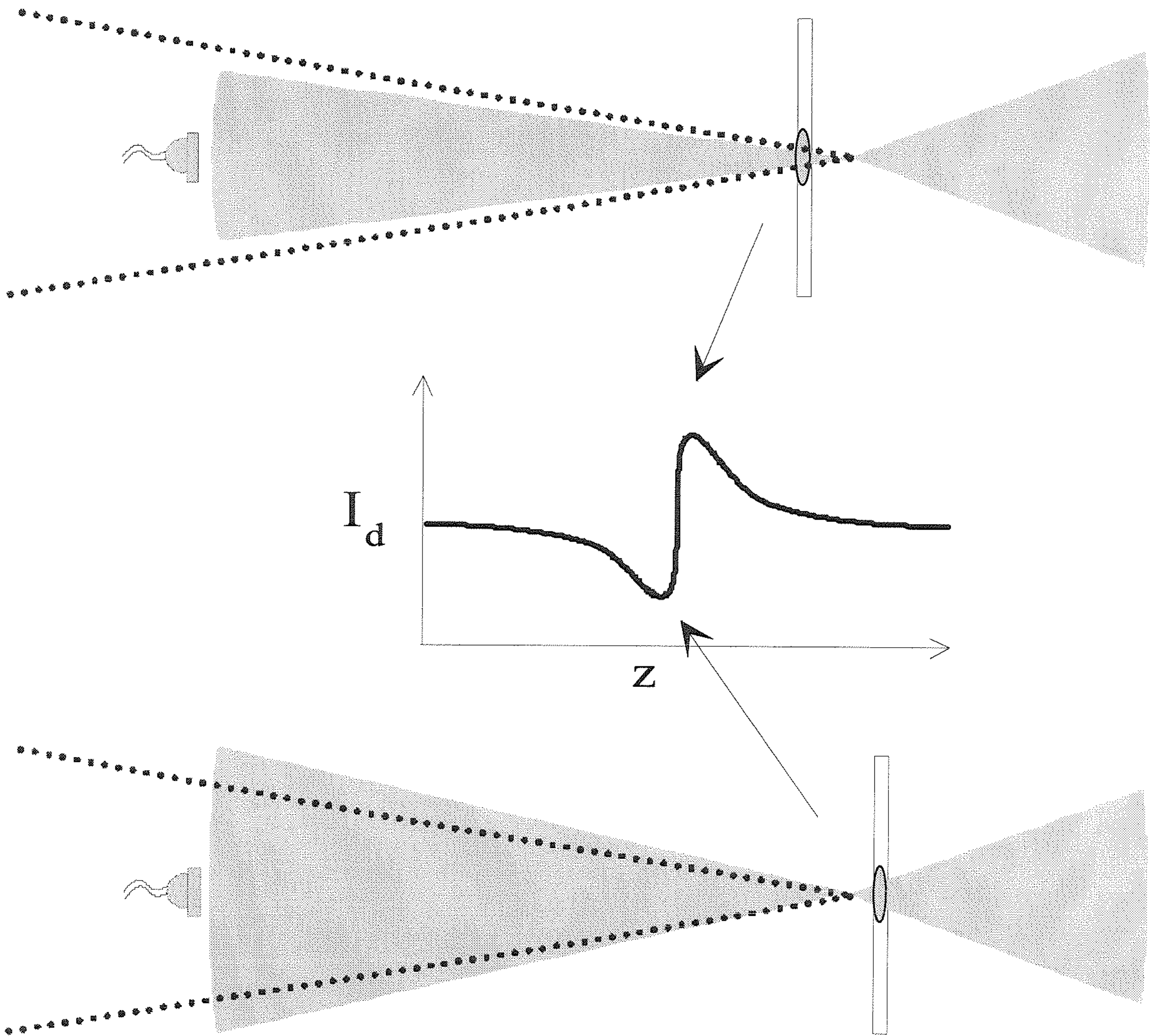

Figure 5.2 Measuring intensity-dependent index perturbation using z-scan.

5.4 Experimental setup.

The source of radiation used was a Q-switched mode-locked Nd:YAG laser. The laser was Q-switched at 5 kHz and there were 6 mode-locked pulses per Q-switch pulse train. The width of each pulse was about 100 Psec. The output of the laser passed through a half-wave plate and a polarizing beam-splitter, so that the output power could be varied without changing the lamp current which usually destabilizes the mode-locked

pulse train due to changes in the thermal lens inside the laser rod. The resulting radiation was focused by a lens onto a sample. A small aperture was placed in the far-field of the transmitted beam and the intensity through the aperture was measured by a Si photodiode. Another photodiode measured the intensity of the incident beam for normalization. Both intensities were acquired during the scan by an A/D card and stored in a laboratory computer. The sample was mechanically moved through the focus of the lens on a motorized micrometer stage having a resolution of 1 micron.

To distinguish between electronic and thermal cubic nonlinearities scans were performed with the laser operating in CW mode with the same average power. It was evident that the effect seen in mode-locked Q-switched mode was not the well-known thermal lens effect.

5.5 Experimental results.

Figures 5.4 and 5.5 show the measured normalized transmittances for Ge and Si nanocrystal samples, respectively. The measured transmittance changes were on the order of a few times the noise of the system due to the fact that the nanocrystal-containing region was extremely thin. Transmittance change on the order of a few percent were observed at highest possible incident intensities which were about 60-70 % of the damage threshold of the material. Figure 5.5 is an optical micrograph of a spot on the Ge-implanted sapphire sample where the damage threshold has been exceeded. The z-scan curve was characterized by a sharp drop of transmittance by a factor of 3-4. A strong scattering from the damaged spot was easily visible through the IR viewer.

Table 5.2 summarizes the experimental results for the four samples investigated.

Observed $\chi^{(3)}$ values were in the 10^{-9} - 10^{-10} esu range. The uncertainty on these values is on the order of 20% and stems mainly from the difficulty of determining exactly the peak laser power.

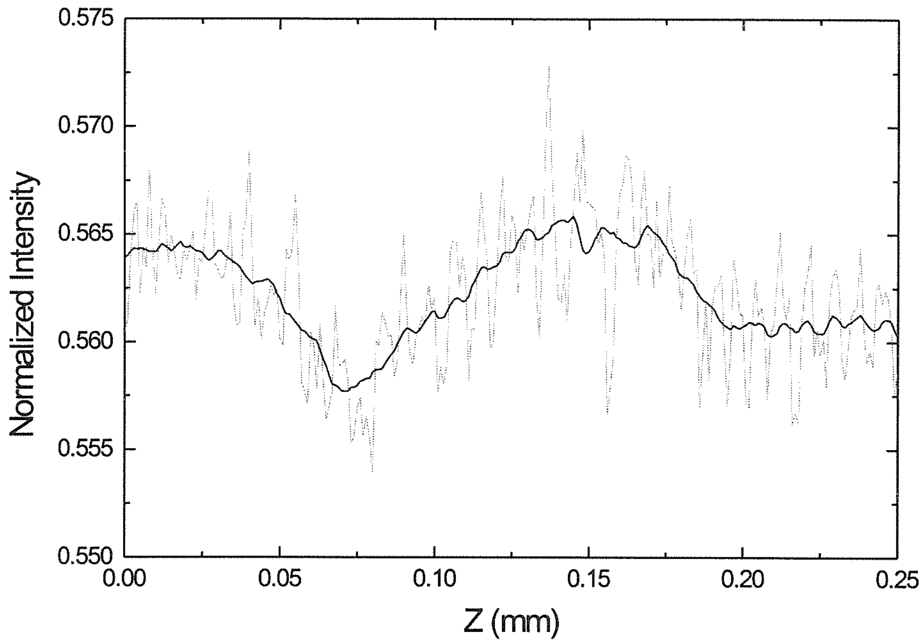

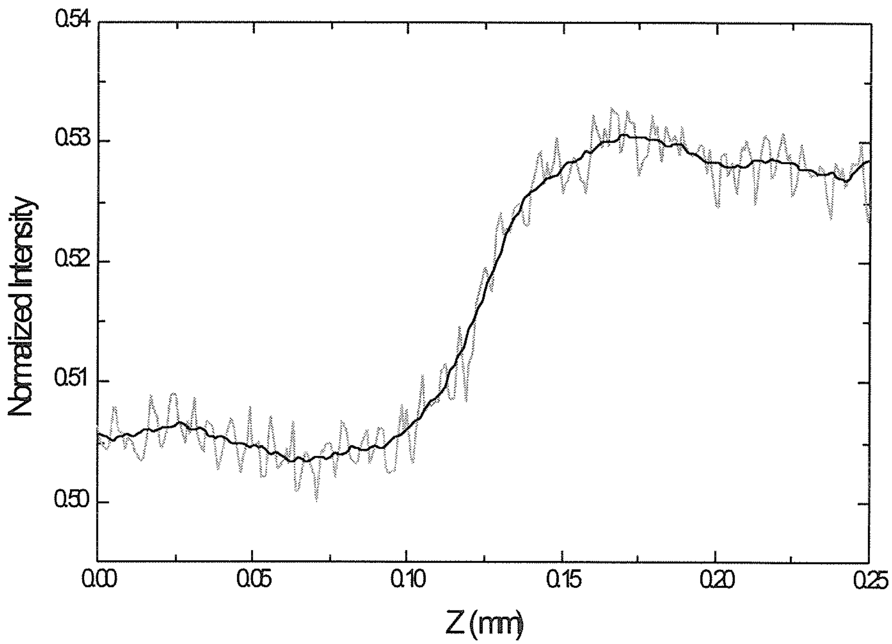

Figure 5.4 Normalized transmitted intensities for the Ge nanocrystals in Al_2O_3 (top) and SiO_2 (bottom) from z-scan measurements

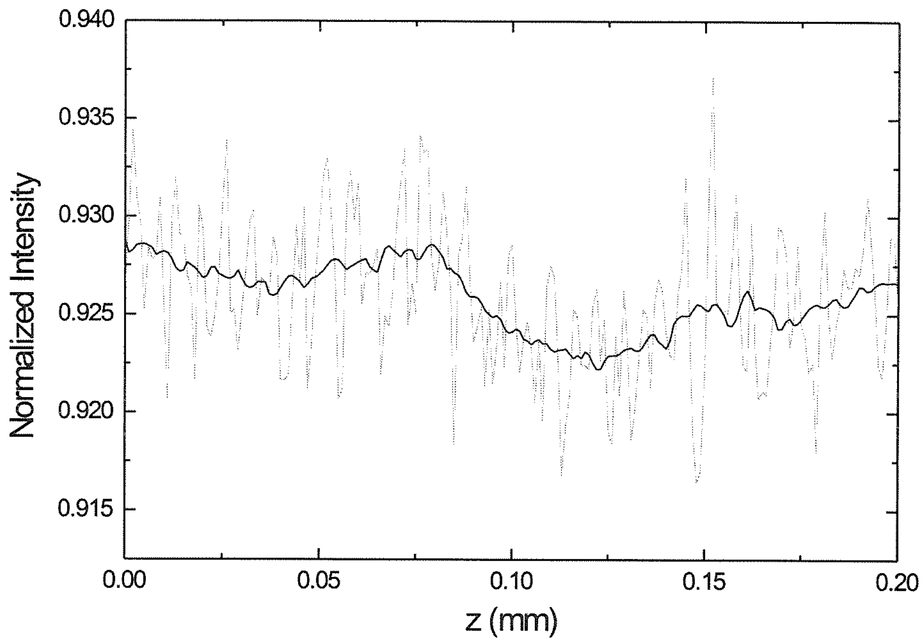

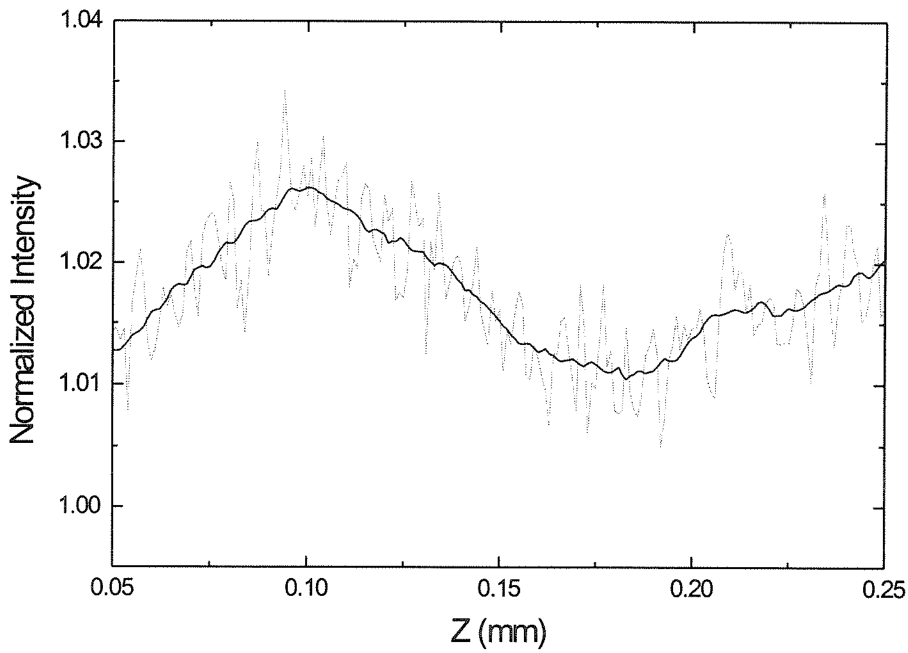

Figure 5.5 Normalized transmitted intensities for the Si nanocrystals in Al_2O_3 (top) and SiO_2 (bottom) from z-scan measurements.

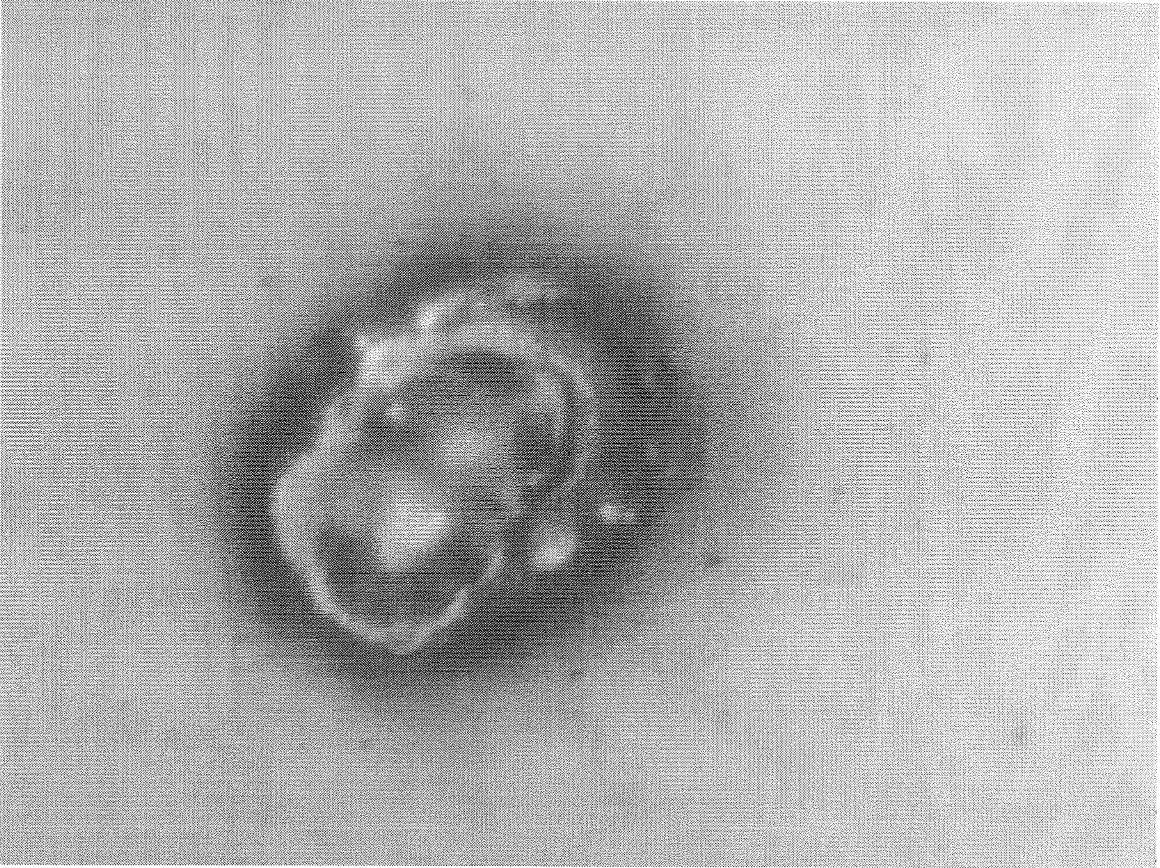

Figure 5.6 Damage to the sample from excessive incident laser power.

While these values are orders of magnitude less than the impressive numbers reported for phosphorus nanoparticles in SiO_2 [8], they are in the range seen for metal clusters in SiO_2 produced by ion implantation. These values may still be useful, if we consider a nanocrystal-doped waveguide where local fields can be reasonably high (on the order of 100 kW/cm^2 equivalent intensity) and the interaction length could make up for the low index perturbations.

Table 5.2 Summary of experimental results.

Sample	Average laser Power(mW)	Peak Intensity (GW/cm^2)	T_{p-v}	Δn	$\chi^{(3)}$ (esu)
$Ge \rightarrow Al_2O_3$	300	27.7	0.021	0.062	3.0×10^{-9}
$Ge \rightarrow SiO_2$	250	23.1	0.04	0.078	3.4×10^{-9}
$Si \rightarrow Al_2O_3$	500	46.2	0.005	0.020	5.7×10^{-10}
$Si \rightarrow SiO_2$	400	36.9	-0.016	0.047	-1.3×10^{-9}

5.6 Conclusions.

Si and Ge nanocrystals have been synthesized in SiO_2 and Al_2O_3 matrixes. Cubic optical nonlinearities of the nanocrystal-containing material were measured using the z-scan technique and found to be in the 10^{-10}-10^{-9} range. These materials may be useful as nonlinear optical elements in integrated optical waveguide devices.

References.

[1] R.W. Boyd, *"Nonlinear Optics"*, Academic Press, San Diego pp. 148-154 (1992)

[2] A. Othmani, J.C. Plenet, E. Bernstein, F. Paille, C. Bovier, J. Dumas, and P.Riblet, Radiation Effects and defects in Solids, **137**, pp. 1335-1339 (1995).

[3] H. Shinojima, J. Yumoto, and N. Ueugi, Appl. Phys. Lett. **60** p. 298 (1992).

[4] S.H. Park, R.A. Morgan, Y.Z. Hu, M. Lindberg, S.W. Koch, and N. Peyghambarian, J. Opt. Soc. Am. B **7**, p.2097 (1990).

[5] R.F. Haglund, R.H. Magruder, S.H. Morgan, D.O. Henderson, R.A. Weller, L. Yang, and R.A. Zuhr, Nucl. Instr. Methods in Phys. Research B65, pp. 405-411 (1992).

[6] R.H. Magruder, L. Yang, R.F. Haglund, C.W. White, Lina Yang, R. Dorsinville, and R.R. Alfano, Appl. Phys. Lett. **62**, p. 1730 (1993).

[7] T. Itoh, S. Iwai, K. Edamatsu, S. Yano, and T. Goto, Japn. J. Appl. Phys. Part 2 (letters) **34** suppl. 34-1, pp.1-4 (1994).

[8] H. Hosono, Y. Abe, Y.L. Lee, T. Tokizaki, and A. Nakamura, Appl. Phys. Lett. **61**, p. 2747 (1992).

[9] N. A. Hill, Private Communication (1994).

[10] T. Takagahara and K. Takeda, Phys. Rev. B **46**, p. 15578 (1992).

[11] B. Delley and E. F. Steigmeier, Phys Rev. B. **47**, p. 1397 (1993).

[12] M.S. Hybertsen, Phys. Rev. Lett. 72, p.1514 (1994).

[13] J.P. Proot, C. Delerue, and G. Allan, Appl. Phys. Lett. **61**, p.1948 (1992).

[14] J.F. Ziegler, J.P. Biersack, and U. Littmark, The Stopping of Ions in Solids, Pergamon, New York (1993).

[15] M. Sheik-Bahae, A.A. Said, T. Wei, D.J. Hagan, and E.W. van Stryland, IEEE J. Quantum Electr. **26**, p. 760 (1990).

Chapter 6
Modulated Source Interferometric Imaging

6.1 Introduction.

Interferometry is one of the most basic manifestations of the wave-like nature of light. It is a broad term for some process or system involving interference of two or more light beams. The first experimental observations date back to Young double-slit experiment in 1801. The realizations and applications of this process are innumerable, and have generally been known for over a hundred years. Most of important and common ones such as Michelson, Mach-Zender, Fizeau, etc. can be found in any book on classical optics [1]. However, most of the experiments have been done with CW sources, and thus the fringe pattern produced as the beams recombine is stationary. A disadvantage of all CW interferometry schemes is that the fringe pattern is periodic in the change of path-length difference which is an integer multiple of the center wavelength of the source (as long as the change is much smaller than the coherence length). Heterodyne interferometry is an exception, here the two beams are monochromatic beams offset by a difference frequency, and thus the fringes beat at the difference frequency of the two beams. The phase of this beating signal is directly related to the optical phase difference between the two beams. This method finds many uses since it is relatively simple to measure the phase of RF signals up to100's of MHz.

Until recently understanding of interferometry with a general spectrum was not developed apparently for the lack of need of understanding a real system.

6.2 Interferometry with a modulated source.

With the advent of semiconductor lasers, light sources became available with a spectrum ranging from a single frequency amplitude modulated source to a periodic source with hundreds of harmonics (such as a modulated semiconductor laser with large chirp, such as a DFB laser), and so the simple treatment available for understanding

heterodyne interferometry does not apply since now one must consider tens to thousands of spectral components. On the other hand, experimental evidence indicates an interesting dependence of the interferometric signal phase and amplitude on the path length difference. This effect was recognized for the first time relatively recently [2] as a result of an interplay of a large number of harmonics. Since treating the system as a conventional sum of a large number of harmonics was prohibitively bulky, an alternate, more general approach was developed by the authors to describe interferometry with an arbitrary spectrum. This approach will be presented in the following sections. It will also become apparent that for a special case of a periodically modulated laser diode, the result can be cast into a particularly elegant and simple form.

6.3 Two-beam interferometry of a source with an arbitrary spectrum.

Let us consider a source with an arbitrary spectrum, $S(\omega)$. Electric field a distance x away from the source will be given by

$$E = \int_{-\infty}^{\infty} S(\omega) e^{i\omega t} e^{-ikx} . \tag{6.3-1}$$

Now let us consider a system where the light from this source is split up into two beams that recombine at a photodetector having traveled a distance x and $x + \Delta x$ respectively. The fields due to the two beams are

$$E_1 = A \int_{-\infty}^{\infty} S(\omega) e^{i\omega t} e^{-ikx} \; ; \qquad E_2 = B \int_{-\infty}^{\infty} S(\omega) e^{i\omega t} e^{-ik(x+\Delta x)} \tag{6.3-2}$$

Here $S(\omega)$ is the signal spectrum, and A and B, the relative amplitudes of the two beams, are real constants. This is sufficiently general since any phase can be accommodated either as a shift of the origin, or as a change in the path length difference Δx. Also, assuming free space propagation we can replace k with ω / c.

The total field is then $E_{tot}=E_1+E_2$, and the detected intensity I_t will be $E_{tot}E^*_{tot}$. Substituting equations (6.3-2) into the expression for the total intensity we obtain after some simple algebra

$$I_t(t) = A^2 \iint S(\omega)S^*(\omega')e^{i(\omega-\omega')t}e^{-\frac{i}{c}(\omega-\omega')x}d\omega d\omega'+$$

$$B^2 \iint S(\omega)S^*(\omega')e^{i(\omega-\omega')t}e^{-\frac{i}{c}(\omega-\omega')(x+\Delta x)}d\omega d\omega'+ \qquad (6.3\text{-}3)$$

$$2AB \iint S(\omega)S^*(\omega')e^{i(\omega-\omega')t}e^{-\frac{i}{c}(\omega-\omega')x}\left(e^{\frac{i}{c}\omega'\Delta x}+e^{-\frac{i}{c}\omega\Delta x}\right)d\omega d\omega'$$

The first two terms represent the intensity due to the two beams separately, and the third term is the interference term which will give rise to the effects of interest. We are now interested in the complex amplitude (amplitude and the phase) of the detected RF signal. To obtain a complex amplitude we filter $I_t(t)$ at some frequency ω_f with some filtering envelope $f(t)$. The complex amplitude at ω_f is therefore given by

$$I_{\omega_f} = \int_{-\infty}^{\infty} I_t(t)f(t)e^{i\omega_f t}dt \qquad (6.3\text{-}4)$$

for the following development we will assume that the integration time is very large, and thus $f(t)$ can be taken approximately as 1. We note here that strictly speaking this assumption is only valid for finite and bounded spectra. For a purely periodic modulation (such as the case of a periodically modulated semiconductor laser) we may obtain infinities in the integration since we can have a finite power in one spectral component and an infinite integration time. There it will be necessary to include some arbitrary finite $f(t)$. We shall see, however that the result changes only by an overall multiplicative constant, and so our present treatment is sufficient for most applications.

Substituting I_t into equation (6.3-4) and carrying out the time integration we obtain the complex amplitude of the RF signal at the filtering frequency

$$I_{\omega_f} = A^2 \iint S(\omega)S^*(\omega')\delta(\omega - \omega' + \omega_f)e^{-\frac{i}{c}(\omega-\omega')x} d\omega d\omega' +$$

$$B^2 \iint S(\omega)S^*(\omega')\delta(\omega - \omega' + \omega_f)e^{-\frac{i}{c}(\omega-\omega')(x+\Delta x)} d\omega d\omega' + \qquad (6.3\text{-}5)$$

$$2AB \iint S(\omega)S^*(\omega')\delta(\omega - \omega' + \omega_f)e^{-\frac{i}{c}(\omega-\omega')x}\left(e^{\frac{i}{c}\omega'\Delta x} + e^{-\frac{i}{c}\omega\Delta x}\right) d\omega d\omega'$$

Carrying out the integration over ω' and combining terms we obtain our final general result

$$I_{\omega_f} = \left(A^2 + e^{\frac{i}{c}\omega_f\Delta x}B^2\right)e^{\frac{i}{c}\omega_f x} \int S(\omega)S^*(\omega + \omega_f)d\omega +$$

$$4ABe^{\frac{i}{c}\omega_f\left(x+\Delta x/2\right)} \int S\left(\omega - \frac{\omega_f}{2}\right)S^*\left(\omega + \frac{\omega_f}{2}\right)\cos\left(\frac{\omega\Delta x}{c}\right)d\omega \qquad (6.3\text{-}6)$$

We immediately notice that while the first term depends only on the relative phase shift at the filtering (RF) frequency, while the interference term is sensitive to relative phase shifts at optical frequency. In a simple system the filtering frequency will be the modulation frequency of the source, although in principle one may use arbitrary filtering frequencies if it is of interest. Also, for a real source with finite coherence length, the interference term will be multiplied by a fringe visibility function the exact form of which depends on the nature of the broadening. For a simple phase random walk (homogeneously broadened system) this function will be $e^{-\frac{\Delta x}{l_c}}$, where l_c is the coherence length of the source.

Of more practical interest is the form of the expression (6.3-6) for a periodically modulated source, such as a semiconductor laser. The spectrum consists of a sum of discrete frequency bands spaced by the modulation frequency ω_m:

$$S(\omega) = \sum_n a_n \delta(\omega - \omega_c - n\omega_m)$$

ω_c being the center frequency of the source, and a_n's- the complex band amplitudes. Substituting this spectrum into equation (6.3-3), setting $\omega_f = \omega_m$ and using an arbitrary filtering function $f(t)$, we obtain after integrating in time:

$$I_{\omega_m} = A^2 \iint \sum_{n,k} a_n a_k^* \delta(\omega - \omega_c - n\omega_m)\delta(\omega' - \omega_c - k\omega_m)\tilde{f}(\omega - \omega' + \omega_m) e^{-\frac{i}{c}(\omega - \omega')x} d\omega d\omega' +$$

$$B^2 \iint \sum_{n,k} a_n a_k^* \delta(\omega - \omega_c - n\omega_m)\delta(\omega' - \omega_c - k\omega_m)\tilde{f}(\omega - \omega' + \omega_m) e^{-\frac{i}{c}(\omega - \omega')(x+\Delta x)} d\omega d\omega' +$$

$$2AB \iint \sum_{n,k} a_n a_k^* \delta(\omega - \omega_c - n\omega_m)\delta(\omega' - \omega_c - k\omega_m)\tilde{f}(\omega - \omega' + \omega_m) e^{-\frac{i}{c}(\omega - \omega')x} \left(e^{\frac{i}{c}\omega'\Delta x} + e^{-\frac{i}{c}\omega\Delta x} \right) d\omega d\omega'$$

where $\tilde{f}(\omega)$ represents the Fourier transform of the filtering function $f(t)$.

Carrying out the double integration over ω's, we obtain

$$I_{\omega_m} = A^2 \sum_{n,k} a_n a_k^* \tilde{f}((n-k+1)\omega_m) e^{\frac{i}{c}(n-k)\omega_m x} +$$

$$B^2 \sum_{n,k} a_n a_k^* \tilde{f}((n-k+1)\omega_m) e^{\frac{i}{c}(n-k)\omega_m (x+\Delta x)} + \qquad (6.3\text{-}7)$$

$$2AB \sum_{n,k} a_n a_k^* \tilde{f}((n-k+1)\omega_m) e^{\frac{i}{c}(n-k)\omega_m x} \left(e^{\frac{i}{c}(\omega_c + k\omega_m)\Delta x} + e^{-\frac{i}{c}(\omega_c + n\omega_m)\Delta x} \right)$$

If the width of $\tilde{f}(\omega)$ is much smaller than ω_m (i.e. the integration time is much longer than the cycle of the modulation) only terms where $k=n+1$ survive and we obtain our final result:

$$I_{\omega_m} = \left(A^2 + B^2 e^{\frac{i}{c}\omega_m \Delta x} \right) \tilde{f}(0) e^{\frac{i}{c}\omega_m x} \sum_n a_n a_{n+1}^* +$$

$$4AB\tilde{f}(0) e^{\frac{i}{c}\omega_m (x + \Delta x/2)} \sum_n a_n a_{n+1}^* \cos\left(\left(\omega_c + (n + \tfrac{1}{2})\omega_m \right) \Delta x \right) \qquad (6.3\text{-}8)$$

As we expected, the filtering function enters only as an overall multiplicative constant, and is thus not of major importance.

6.4 Sinusoidally modulated semiconductor laser.

For a realistic sinusoidally current-modulated semiconductor laser, the field may be written as $E(x,t)=\sqrt{1-m\cos(\omega_m t)}\cdot e^{i\beta\sin(\omega_m t+\phi)}e^{i\omega t}e^{-ikx}$, where m is the current modulation depth, β is the phase modulation depth resulting from laser chirp, and ϕ is the phase between them [4]. For reasonably small m we expand the expression under the square root to second order in m, and the sinusoid in the exponential - as an infinite sum of Bessel functions.

$$E(x,t)=\left\{1-\frac{m^2}{16}-\frac{m}{2}\cos(\omega_m t)-\frac{m^2}{16}\cos(2\omega_m t)\right\}\sum_{n=-\infty}^{\infty}J_n(\beta)e^{in(\omega_m t+\phi)}e^{i\omega t}e^{-ikx}$$

We are interested in a_n's, the complex band amplitudes of the resulting spectrum. Substituting sums of complex exponentials for the two cosines and rearranging terms we can read off the complex coefficients:

$$a_n=\left(1-\frac{m^2}{16}\right)J_n(\beta)e^{in\phi}-\frac{m}{4}\left(J_{n-1}(\beta)e^{i(n-1)\phi}+J_{n+1}(\beta)e^{i(n+1)\phi}\right)-$$
$$\frac{m^2}{32}\left(J_{n-2}(\beta)e^{i(n-2)\phi}+J_{n+2}(\beta)e^{i(n+2)\phi}\right)$$

We can now substitute them into Eq. 6.3-8. We notice that the coefficients always enter as $a_n a^*_{n+1}$, so we calculate this expression explicitly. As before, we only keep terms up to the second power in m.

$$a_n a^*_{n+1}=-\frac{m}{4}\left(J_n^2+J_{n+1}^2\right)+e^{i\phi}\frac{m^2}{32}\left(2J_nJ_{n+1}-J_nJ_{n-1}-J_{n+1}J_{n+2}\right)+$$
$$e^{-i\phi}\left\{J_nJ_{n+1}+\frac{m^2}{16}\left(-2J_nJ_{n+1}+J_nJ_{n-1}+J_{n+1}J_{n+2}\right)\right\}-$$
$$e^{-2i\phi}\frac{m}{4}\left(J_nJ_{n+2}+J_{n+1}J_{n-1}\right)+e^{-3i\phi}\frac{m^2}{32}\left(2J_{n-1}J_{n+2}-J_nJ_{n+3}-J_{n-2}J_{n+1}\right)$$

We must now do the sums involving $a_n a^*_{n+1}$ in Eq. 6.3-8. $\sum_n a_n a^*_{n+1}$ is easily evaluated since Bessel functions form an orthogonal and complete set. Only $J_n J_n$ and $J_{n+1} J_{n+1}$ terms survive in the sum. After some manipulation we find that $\sum_n a_n a^*_{n+1} = -\frac{m}{2}$. The second sum involving the cosine is a little more difficult to evaluate. Fortunately there are summation formulas for just this form, a product of two Bessel functions with a sine or a cosine.

$$\sum_{n=-\infty}^{\infty} J_n(\beta) J_{n+N}(\beta) \begin{matrix}\cos \\ \sin\end{matrix}(n\alpha + \varphi) = J_N(\zeta) \begin{matrix}\cos \\ \sin\end{matrix}(N\chi + \varphi)$$

where $\zeta = 2\beta \sin\left(\frac{\alpha}{2}\right)$ and $\chi = \frac{\pi}{2} - \frac{\alpha}{2}$. Using this summation formula, and defining $\varphi = \frac{(\omega_c + \omega_m/2)\Delta x}{c}$ and $\alpha = \frac{\omega_m \Delta x}{c}$, we obtain after some algebra

$$\begin{aligned}\sum_n a_n a^*_{n+1} \cos\left(\left(\omega_c + (n+\tfrac{1}{2})\omega_m\right)\Delta x\right) &= -\frac{m}{4} J_0(\zeta)\{\cos\varphi + \cos(\varphi - \alpha)\} + \\ e^{i\phi} J_1(\zeta)\frac{m^2}{16}\cos(\chi+\varphi)(1-\cos\alpha) &+ e^{-i\phi} J_1(\zeta)\left\{\cos(\chi+\varphi) - \frac{m}{8}\cos(\chi+\varphi)(1-\cos\alpha)\right\} - \\ e^{-2i\phi} J_2(\zeta)\frac{m}{4}\{\cos(2\chi+\varphi) + \cos(2\chi+\varphi+\alpha)\} &+ e^{-3i\phi} J_3(\zeta)\frac{m^2}{16}\cos(3\chi+\varphi+\alpha)(1-\cos\alpha)\end{aligned} \qquad (6.3\text{-}9)$$

for $\alpha \ll 1$ the expression simplifies to

$$\sum_n a_n a^*_{n+1} \cos(n\alpha + \varphi) = -\frac{m}{2} J_0(\zeta)\cos\varphi + e^{-i\phi} J_1(\zeta)\cos(\chi+\varphi) - e^{-2i\phi} J_2(\zeta)\frac{m}{2}\cos(2\chi+\varphi)$$

although if we want to use this method for measuring substantial distances, we must use Eq. 6.3-9. Finally we substitute back into Eq. 6.3-8 to obtain the final result for a modulated semiconductor laser.

$$I_{\omega_m} = -\left(A^2 + B^2 e^{\frac{i}{c}\omega_m \Delta x}\right)\tilde{f}(0)\frac{m}{2} +$$

$$4AB\tilde{f}(0)e^{\frac{i}{c}\omega_m(x+\Delta x/2)}\begin{bmatrix} -\frac{m}{4}J_0(\zeta)\{\cos\varphi + \cos(\varphi-\alpha)\} + e^{i\phi}J_1(\zeta)\frac{m^2}{16}\cos(\chi+\varphi)(1-\cos\alpha) + \\ e^{-i\phi}J_1(\zeta)\left\{\cos(\chi+\varphi) - \frac{m}{8}\cos(\chi+\varphi)(1-\cos\alpha)\right\} - \\ e^{-2i\phi}J_2(\zeta)\frac{m}{4}\{\cos(2\chi+\varphi) + \cos(2\chi+\varphi+\alpha)\} + \\ e^{-3i\phi}J_3(\zeta)\frac{m^2}{16}\cos(3\chi+\varphi+\alpha)(1-\cos\alpha) \end{bmatrix}$$

It is immediately apparent that the phase and amplitude of the RF signal are sensitive to the optical phase difference between the two path-lengths (the presence of φ inside the cosine terms).

It is interesting to point out that a metrology system based on MSI is possible with no moving parts. A DFB laser wavelength can be shifted slightly by varying the bias current, and thus scanning the reference arm path length becomes unnecessary. All that is needed is a static path length difference.

6.5 Interferometric Imaging with a modulated source.

We can use a similar treatment to derive an expression for a far-field time-dependent intensity of a modulated beam passing through an amplitude/phase "mask", and interfering in the far-field with a reference plane wave. The schematic of the setup is shown in Figure 6.1.

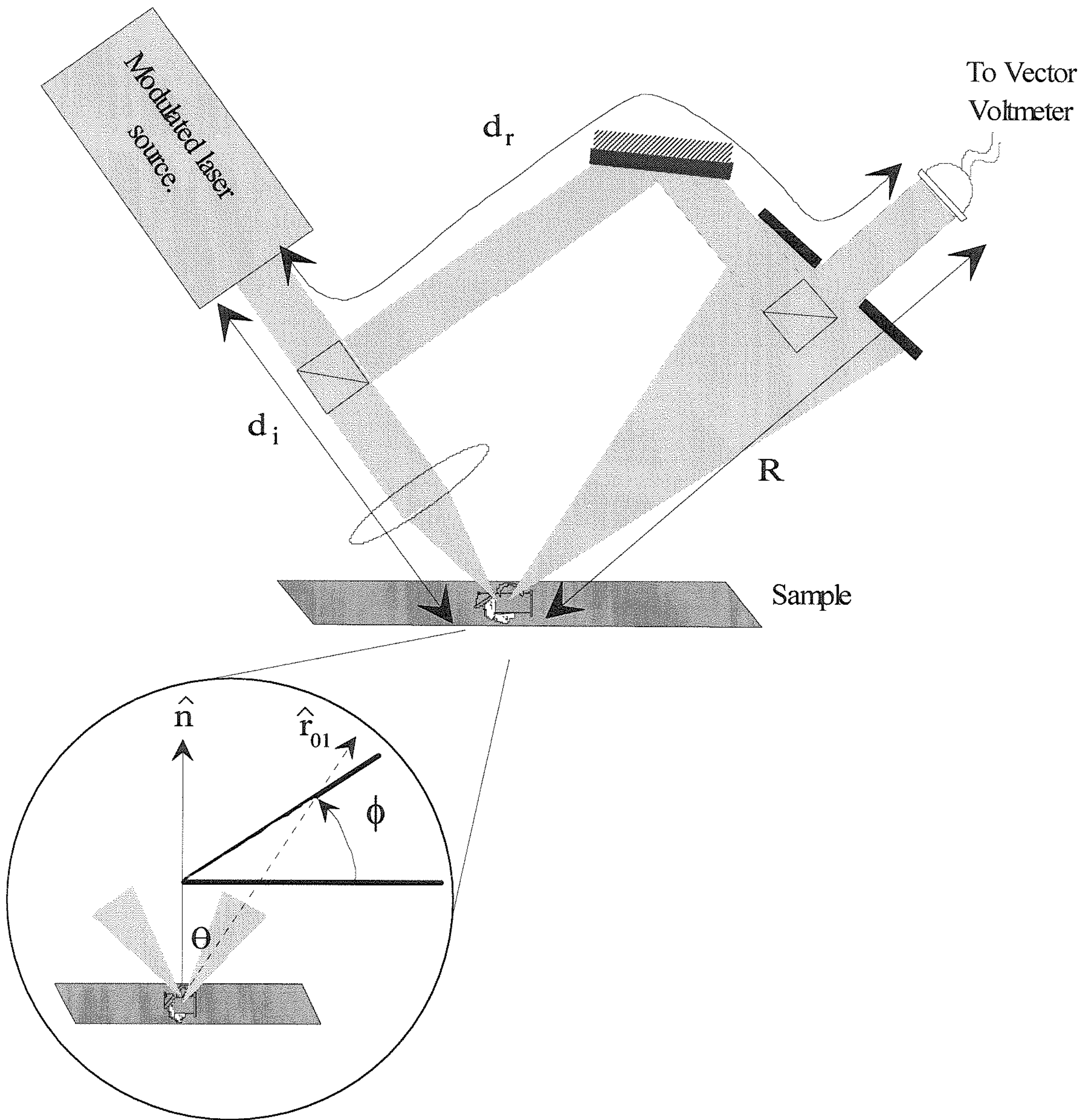

Figure 6.1 Schematic of the MSI imaging setup.

We use the Sommerfeld diffraction formula to describe the propagation of the image-bearing beam.

$$U(P_0) = -\frac{i}{\lambda} \iint U(P_1) \frac{e^{-ikr_{01}}}{r_{01}} \cos(\hat{n}, \hat{r}_{01}) ds$$

In our schematic $\cos(\hat{n}, \hat{r}_{01})$ becomes $\cos\theta$, and we approximate r_{01} in the denominator by R, since we are primarily interested in the complex phase contributions arising from the exponential in the numerator, and for our condition $R >> x_{max}, y_{max}$ correction terms in the denominator will enter in the second order. In the exponential of the numerator, however, we expand r_{01} to first order in x and y. Making these approximations we obtain after some algebra the formula for the image-bearing beam at the interference point:

$$E_{im} = \int \frac{-i\omega \cos\theta}{2\pi c R} e^{-\frac{i\omega}{c}(R+d_i)} S(\omega) e^{i\omega t} \iint A(x,y) e^{\frac{i\omega}{c}(x \sin\theta \cos\phi + y \sin\theta \sin\phi)} dx dy d\omega$$

Here $A(x, y)$ is the complex field intensity at the sample plane formed as a result of reflecting off the sample.

The reference beam is a plane wave that travels an arbitrary distance d_r before interfering with a portion of the far-field of the image-bearing beam, and is given as for the two beam case by

$$E_{ref} = B \int e^{i\omega t} e^{-\frac{i\omega}{c} d_r} S(\omega) d\omega$$

We combine the two beams as before, and our total detected intensity is

$$E_{tot} E_{tot}^* = |E_{ref}|^2 + |E_{im}|^2 + E_{ref} E_{im}^* + E_{ref}^* E_{im}$$

We will ignore the first two terms since they represent intensities of the two beams in absence of interference, and thus can be measured separately and subtracted out is necessary. The information we are interested in will be contain in the last two terms, the interference terms. We thus focus on them explicitly using a periodic spectrum for the source, $S(\omega) = \sum_n a_n \delta(\omega - \omega_c - n\omega_m)$. Repeating the treatment for the two-beam interferometry and filtering at an integer multiple of the modulation frequency, $k\omega_m$, we obtain

$$E_{ref}E^*_{im} \Rightarrow \tilde{f}(0)\frac{i\cos\theta}{2\pi cR}\sum_n a_n a^*_{n+k} e^{\frac{i\omega_c}{c}(R+d_i-d_r)} e^{\frac{i\omega_m}{c}((n+k)(R+d_i)-nd_r)} (\omega_c+(n+k)\omega_m) \bullet$$

$$\iint A^*(x,y) e^{-\frac{i}{c}(\omega_c+(n+k)\omega_m)(x\sin\theta\cos\phi+y\sin\theta\sin\phi)} dxdy$$

and

$$E^*_{ref}E_{im} \Rightarrow \tilde{f}(0)\frac{-i\cos\theta}{2\pi cR}\sum_n a_n a^*_{n+k} e^{-\frac{i\omega_c}{c}(R+d_i-d_r)} e^{\frac{i\omega_m}{c}((n+k)d_r-n(R+d_i))} (\omega_c+n\omega_m) \bullet$$

$$\iint A(x,y) e^{\frac{i}{c}(\omega_c+n\omega_m)(x\sin\theta\cos\phi+y\sin\theta\sin\phi)} dxdy$$

We can do the spatial integration since the terms in the integral represent a simple 2-D Fourier transform of the image intensity.

$$E_{ref}E^*_{im} \Rightarrow \tilde{f}(0)\frac{i\cos\theta}{2\pi cR}\sum_n a_n a^*_{n+k} e^{\frac{i\omega_c}{c}(R+d_i-d_r)} e^{\frac{i\omega_m}{c}((n+k)(R+d_i)-nd_r)} (\omega_c+(n+k)\omega_m) \bullet$$

$$\tilde{A}^*\left(\frac{(\omega_c+(n+k)\omega_m)\sin\theta\cos\phi}{c}, \frac{(\omega_c+(n+k)\omega_m)\sin\theta\sin\phi}{c}\right)$$

$$E^*_{ref}E_{im} \Rightarrow \tilde{f}(0)\frac{-i\cos\theta}{2\pi cR}\sum_n a_n a^*_{n+k} e^{-\frac{i\omega_c}{c}(R+d_i-d_r)} e^{\frac{i\omega_m}{c}((n+k)d_r-n(R+d_i))} (\omega_c+n\omega_m) \bullet$$

$$\tilde{A}\left(\frac{(\omega_c+n\omega_m)\sin\theta\cos\phi}{c}, \frac{(\omega_c+n\omega_m)\sin\theta\sin\phi}{c}\right)$$

These terms can be deconvoluted to obtain spatial amplitude and phase with precision exceeding regular imaging by orders of magnitude. The resulting information can be analytically extended to higher spatial frequencies and thus objects below diffraction limit can be imaged. This technique may be useful in investigating the properties of nanostructures, as well as for sub-micron non-contact alignment for deep UV and x-ray lithography in steppers.

References.

[1] M. Born and E.Wolf, "*Principles of Optics*" Pergamon, New York (1975).

[2] R.C. Gutierrez, Master's Thesis UCSB (1993).

[3] R.C. Gutierrez and K.V. Shcheglov, "*Modulated Source Interferometry*" to be published.

[4] H. Olesen and G. Jacobsen, IEEE J. Quantum Electr. **QE-18**, p. 2069 (1982).